THERMAL MANAGEMENT OF THE COPPER-CHLORINE CYCLE FOR HYDROGEN PRODUCTION: ANALYTICAL AND EXPERIMENTAL INVESTIGATION OF HEAT RECOVERY FROM MOLTEN SALT

by

Samane Ghandehariun

A Thesis Submitted in Partial Fulfillment

of the Requirements for the Degree of

DOCTOR OF PHILOSOPHY

in

The Faculty of Engineering and Applied Science

Mechanical Engineering Program

University of Ontario Institute of Technology

August 2012

In the Name of God

Most Gracious

Most Merciful

Abstract

Hydrogen is known as a clean energy carrier which has the potential to play a major role in addressing the climate change and global warming, and thermochemical water splitting via the copper-chlorine cycle is a promising method of hydrogen production. In this research, thermal management of the copper-chlorine cycle for hydrogen production is investigated by performing analytical and experimental analyses of selected heat recovery options. First, the heat requirement of the copper-chlorine cycle is estimated. The pinch analysis is used to determine the maximum recoverable heat within the cycle, and where in the cycle the recovered heat can be used efficiently. It is shown that a major part of the potential heat recovery can be achieved by cooling and solidifying molten copper(I) chloride exiting one step in the cycle: the oxygen reactor. Heat transfer from molten CuCl can be carried out through direct contact or indirect contact methods. Predictive analytical models are developed to analyze a direct contact heat recovery process (i.e. a spray column) and an indirect contact heat recovery process (i.e. a double-pipe heat exchanger).

Characteristics of a spray column, in which recovered heat from molten CuCl is used to produce superheated steam, are presented. Decreasing the droplet size may increase the heat transfer rate from the droplet, and hence decreases the required height of the heat exchanger. For a droplet of 1 mm, the height of the heat exchanger is predicted to be about 7 m. The effect of hydrogen production on the heat exchanger diameter was also shown. For a hydrogen production rate of 1000 kg/day, the diameter of the heat exchanger is about 3 m for a droplet size of 1 mm and 2.2 m for a droplet size of 2 mm.

The results for axial growth of the solid layer and variations of the coolant temperature and wall temperature of a double-pipe heat exchanger are also presented. It is shown that reducing the inner tube diameter will increase the heat exchanger length and increase the outlet temperature of air significantly. It is shown that the air temperature increases to 190^{o}C in a heat exchanger with a length of 15 cm and inner tube radius of 10 cm. The length of a heat exchanger with the inner tube radius of 12 cm is predicted to be about 53 cm. The outlet temperature of air is about 380^{o}C in this case. The length of a heat exchanger with an inner tube diameter of 24 cm is predicted to be about 53 cm and 91 cm for coolant flow rates of 3 g/s and 4 g/s, respectively. Increasing the mass flow rate of air will increase the total heat flux from the molten salt by increasing the length of the heat exchanger. Experimental studies are performed to validate the proposed methods and to further investigate their feasibility. The hazards involving copper(I) chloride are also investigated, as well as corresponding hazard reduction options. Using the reactant Cu_2OCl_2 in the oxygen production step to absorb CuCl vapor is the most preferable option compared to the alternatives, which include absorbing CuCl vapor with water or $CuCl_2$ and building additional structures inside the oxygen production reactor.

Acknowledgments

The author is most grateful for all the guidance and support received throughout this research from her co-supervisors: Prof. Greg F. Naterer and Prof. Marc A. Rosen. The author would also like to thank the thesis committee: Prof. Ibrahim Dincer, Dr. Zhaolin Wang, Dr. Liliana Trevani, and Prof. Zafer Dulger for their time and advice. The author would also like to thank her friends in the Clean Energy Research Laboratory and her family for their help and support.

Table of Contents

List of Tables

List of Figures

Nomenclature

A	Surface area [m^2]
A_c	Cross-sectional area [m^2]
B	Bias
Bi	Biot number
C_D	Drag coefficient
C_p	Specific heat at constant pressure [J/kg.K]
d	Droplet diameter, or the planes spacing in the atomic lattice [m]
D_{vg}	Vapor-gas mass diffusivity [m^2/s]
E_b	Blackbody emissivity power [W]
F	Force [N]
Fo	Fourier number
g	Gravitational acceleration [m/s^2]
h	Heat transfer coefficient [$W/m^{2\cdot}K$]
h_m	Mass transfer coefficient [m/s]
k	Thermal conductivity [W/m.K]
L	Latent heat of phase change [kJ/kg]
Le	Lewis number
M	Molar mass [kg/mol]
m	Mass [kg]
Nu	Nusselt number

P	Pressure [Pa]
Pe	Peclet number
Pr	Prandtl number
$\dot{q}$	Heat transfer rate [W]
R	Droplet radius [m]
r	Radial coordinate [m]
r^*	Non-dimensional radial coordinate
R_u	Universal gas constant [J/mol.K]
Re	Reynolds number
r	Radial coordinate [m]
S	Precision
Sc	Schmidt number
Sh	Sherwood number
Ste	Stefan number
T	Temperature [°C]
t	Time [s], or Student's multiplier
U	Uncertainty
V	Diffusion volume, used in calculating vapor-gas diffusivity
v	Velocity [m/s]
v_t	Terminal velocity [m/s]
W	Radiation power received by infrared camera [W]
y	Flight distance [m]
z	Axial coordinate [m]

z^*	Non-dimensional axial coordinate

Greek symbols

α	Thermal diffusivity [m^2/s]
β	Fixed (bias) error
δ_k	Measurement error
ϵ	Emissivity
ϵ_k	Random (precision) error
ζ_n	Positive roots of the transcendental equation
θ	Angle between the incident ray and the scattering planes [rad]
θ^*	Non-dimensional temperature
θ_i	Sensitivity factor
λ	Wavelength of the incident wave [m]
μ	Dynamic viscosity [Pa.s]
ρ	Density [kg/m^3]
σ	Stefan-Boltzmann constant [$W/m^2.K^4$]
τ	Non-dimensional time, or transmittance

Subscripts

atm	Atmosphere
B	Buoyancy, or bias
b	Bulk

c	Coolant, or convection
D	Drag
d	Droplet
f	Freezing
G	Gravity
g	Gas
i	Inner, or initial
in	Inlet
l	Liquid
m	Mass transfer
n	Nucleation
o	Outer
obj	Object
R	Result
r	Radiation
s	Solid, or surface
sur	Surroundings
v	Vapor
w	Wall
∞	Ambient

Chapter 1 Introduction

Worldwide energy demand is increasing rapidly due to the continuing increase in world population and the desires of developing countries to improve their living standards. A large portion of the world energy demand is met by fossil fuels, because of their availability and convenience. However, it is expected that fossil fuel production worldwide may peak in 15 years and thereafter begin to decrease [1]. Also, the environmental damage caused by fossil fuels and their combustion products is a major problem. Therefore, energy researchers are investigating alternative sources of energy to replace fossil fuels.

If fossil fuels continue to be used at high rates, the environmental impact (i.e. acid rains, ozone depletion, and climate change) will be significant [2,3]. Therefore, the use of clean energy is becoming an urgent matter as the energy demand keeps on increasing. Hydrogen may be derived from non-fossil sources, it burns cleanly to produce water with no pollutants emitted, it is suitable for use in a fuel cell to generate electricity directly, and its energy content per mass is 2.5 times higher than that of any other conventional fuel [3,4]. Therefore, hydrogen has been considered as the energy carrier of the future [3-6].

1.1 Motivation

Hydrogen has the potential to have a major role in addressing global warming and climate change. However, most of the world's hydrogen is currently derived from fossil fuels through some type of reforming process [7,8]. Thus, developing sustainable, large-scale, low-cost

methods of hydrogen production from energy sources other than fossil fuels is required to reduce greenhouse gas emissions and accelerate the transition to a low-carbon future.

Water electrolysis and thermochemical water splitting, using various heat sources such as nuclear energy, solar energy, and geothermal energy, are alternative processes for such hydrogen production. The overall efficiency of thermochemical cycles is potentially higher than electrolysis as heat is used directly to produce hydrogen. Overall electrolysis efficiency is typically about 24%, based on the ratio of the higher heating value of hydrogen to the thermal energy input to generate electricity for electrolysis, while thermochemical hydrogen using nuclear heat can achieve heat to hydrogen efficiency up to about 50% [9]. Several thermochemical cycles for hydrogen production have been developed over the past four decades. Among those, the copper-chlorine cycle is one of the most promising candidates, and requires heat input at a maximum temperature of less than 550℃ [10-13].

The overall efficiency of a thermochemical water splitting cycle can be improved by recovering heat within the cycle and minimizing the net heat supply of the cycle. The total potential for heat recovery within the copper-chlorine cycle is quantified in this research. It is shown that a major portion of the potential heat recovery can be achieved by recovering heat from molten copper(I) chloride, the product of a step of the cycle (the oxygen reactor). Recovering heat from molten CuCl is challenging, as the process involves phase change from liquid to solid and vapor. Conventional heat exchangers cannot be used for heat recovery from molten CuCl, because the system will clog due to solidification. Research is needed to investigate possible processes of heat recovery from molten CuCl which account for solidification and are applicable for the

copper-chlorine cycle. Heat recovery opportunities in the copper-chlorine cycle and the processes of heat recovery from molten CuCl are studied in this thesis. The methods for reduction the hazards in the processes are also investigated.

1.2 Objectives

The main overall objective of this research is to investigate options for recovering thermal energy within the copper-chlorine cycle of hydrogen production. For this purpose, the maximum recoverable heat within the cycle is evaluated using pinch analysis. The integration of the heat recovery with the overall thermochemical cycle is also investigated. Therefore the first objective of this thesis is to determine how much and where in the cycle heat can be recovered and where the recovered heat can be used.

As the major part of heat recovery is achieved by cooling and solidifying molten copper(I) chloride exiting the oxygen reactor, the focus of this thesis will be on heat recovery from molten CuCl

Several methods for recovering heat from molten CuCl, based on the existing industrial processes for molten materials, are investigated. Parameters such as heat transfer rate, the potential of introducing extra substances to the cycle, energy efficiency, material issues and design feasibility are considered to determine the most promising and efficient method for heat recovery from molten CuCl. Heat recovery methods based on casting/extrusion and atomization, using water or air as a coolant, are found to be the most advantageous for heat recovery from molten CuCl. Therefore, these two methods are chosen for further investigation.

Improving understanding of the chemical reactions that may occur during the heat recovery process is another objective of this research. Experiments are performed for a direct contact heat recovery process to study the possibility of chemical reactions in different conditions.

The other objective of this research is to analyze the proposed methods of heat recovery by developing predictive models for heat transfer from molten CuCl in a direct contact heat exchanger, as well as an indirect-contact heat exchanger. For an indirect contact heat exchanger, heat transfer from a solidifying flow of molten CuCl is modeled. The inlet and outlet temperature of the coolant and molten salt, and the dimensions of the heat exchanger are found. For a direct contact heat exchanger, solidification of molten droplets falling through the coolant is modeled. Heat transfer due to convection, radiation and mass transfer is studied. The dimensions of the heat exchanger are determined for different values of hydrogen production rate. The models are used in improving heat recovery system design for the Cu-Cl cycle.

The hazards caused by copper(I) chloride, during the heat recovery process, are investigated and different options for reducing the hazards in the copper-chlorine cycle are explored. Besides hazards reduction, the copper(I) chloride should be recovered and returned to the Cu-Cl cycle. This is also investigated in this research.

1.3 Scope of thesis

Background topics relevant to this research are discussed and a literature survey is presented in Chapter 2. The approaches used in the research as well as methods employed are explained in Chapter 3. In Chapter 4, pinch analysis is used to compute the maximum

recoverable heat within the copper-chlorine cycle. Different options for using the recovered heat in the cycle are studied in this chapter. Chapter 5 presents a comparative review of different methods for recovering heat from molten CuCl. Several parameters are considered in the evaluation of the methods. The casting/extrusion method appears to be the most promising method of heat recovery from molten CuCl in the Cu-Cl cycle. In Chapter 6, mathematical models for direct contact and indirect contact heat transfer from molten copper(I) chloride are presented. Chapter 7 includes the experimental studies for direct-contact heat transfer from molten copper(I) chloride. The results of the modeling and experiments are demonstrated and validated in Chapter 8. Chapter 9 includes CuCl hazards reduction methods for providing a safe working environment while producing clean hydrogen. In Chapter 10, the main conclusions and recommendations are presented.

Chapter 2 Background

2.1 Clean energy

Energy development is increasingly dominated by major global concerns of over population, air pollution, coastal pollution, fresh water pollution, deforestation, biodiversity loss, and global climate deterioration.

A sustainable energy vision of the future centers on the need to reduce global green house gas emissions, ensure security of energy supply, and create a new industrial and technological energy base [14].

Renewable energy has grown rapidly in recent years [15]. Renewable resources produced 16.5% of the world primary energy in 2005 [15]. The share of world electricity was 18% mostly from hydro resources [16]. Renewable sources may be the only candidates for satisfying most of the criteria of the sustainable backstop supply technology, except perhaps for the aspect of financial affordability when compared to the present low prices of fossil and nuclear power. For example, photovoltaic power from the sunlight is unlimited, but expensive to collect and convert, and additional steps are required to bridge intermittent supplies. Several other renewable power resources experience similar challenges [17].

Most unlimited energy sources are provided as flows from the sun which are known to be diffuse, fluctuating, intermittent, and sometimes badly predictable. Collection and conversion of the flows require significant investments and, because they

are not available on command, they need feed-forward control, storage facilities, and make-up and back-up power supplies delivered by other capacities [18].

Hydrogen may play an important role as an energy carrier of the future [19-23]. It may be used as a fuel in almost every application where fossil fuels are being used today, but without harmful emissions, with an exception of NO_x emissions when hydrogen is combusted (however these can be controlled). In addition, hydrogen may be converted into useful forms of energy more efficiently than fossil fuels. And despite public perception, hydrogen is as safe as other common fuels [24]. However, hydrogen is not an energy source. It does not occur in nature in its elemental or molecular form. Therefore, hydrogen must be produced.

2.2 Hydrogen production methods

The annual world consumption of hydrogen is about 50 billion kilograms, which is used primarily for ammonia production and conversion of heavier crude oils to lighter liquid fuels [25]. The hydrogen demand has grown rapidly because of a decrease in availability of light crude oils which do not require extra hydrogen for conversion to gasoline, with a corresponding increase in use of heavy crude oils which require large amounts of hydrogen for conversion to gasoline. If the cost goals for automotive fuel cells are reached, the transportation sector may ultimately be fueled by hydrogen. This implies a growth in hydrogen consumption of one to two orders of magnitude over a period of several decades [26].

Nuclear energy provides a source of heat that can be used to produce hydrogen. Multiple processes are being investigated to produce hydrogen from water and heat. If

nuclear energy is to be used for hydrogen production, the nuclear reactor must deliver the heat at conditions that match the requirements imposed by the H_2 production process [25].

The electrolysis of water to produce hydrogen is a mature technology that is used today to produce hydrogen. Electrolysis is not currently competitive for the large-scale production of hydrogen, except where low-cost electricity is available [25]. Using electrolysis for large-scale H_2 production over the long term depends upon the evolution of the electric grid, the capital costs of electrolysis, and other factors [25]. Current capital costs are estimated to be near $600/kW, while some predict future capital costs may approach $300/kW [25]. Conventional alkaline electrolyzers have efficiencies of 70–85%, and proton-exchange-membrane electrolyzers are projected to have efficiencies of 80–90%. There is a significant trade-off between capital costs and efficiency [26]. In many industrialized countries, the peak electrical demand is twice the minimum demand. Consequently, low-cost off-peak electricity is often available in such jurisdictions. Electrolysis may be viable provided there is successful development of efficient, low-cost electrolysis systems and associated local H_2 storage and distribution systems.

Today, hydrogen is produced primarily from the steam-reforming of natural gas. Steam reforming is an energy-intensive endothermic low-pressure process requiring high-temperature heat input. The input natural gas is used as the reduced chemical source of H_2 and burned to produce heat to drive the process at temperatures of up to 900^{o}C [27]. The amount of natural gas required for steam reforming can be significantly reduced when heat is provided by a nuclear reactor. The Japan Atomic Energy Research Institute is currently preparing to demonstrate the production of hydrogen by steam reforming of natural gas with the heat input provided by its High-Temperature Engineering Test

Reactor (HTTR) [27]. For Japan and other countries with high-cost natural gas, economic analyses indicate that hydrogen from nuclear-assisted steam reforming of natural gas will have lower costs than that from natural gas alone [27].

Thermochemical cycles are alternative and potentially more efficient methods to produce hydrogen from water [28,29]. A thermochemical water splitting process includes decomposition of water into hydrogen and oxygen using heat or a combination of heat and electricity, in a hybrid thermochemical cycle. The net reaction is as follows:

$$H_2O(l) \rightarrow H_2(g) + 1/2\ O_2(g) \quad (1.1)$$

Several thermochemical water splitting cycles, using various sources of energy, have been studied in the past. Abanades et al. [30] studied solar hydrogen production from a two-step thermochemical cycle based on a SnO_2/SnO redox reaction. A thermochemical cycle based on a Zn/ZnO redox reaction was presented by Steinfeld [31]. Galvez et al. [32] studied a two-step solar thermochemical cycle based on MgO/Mg redox reaction. The feasibility of a solar thermochemical cycle, based on a CeO_2/Ce_2O_3 cycle, was demonstrated at a lab scale by Abanades and Flamant [33].

The sulfur-iodine thermochemical cycle, in which solar energy is used for the decomposition of sulphuric acid, was investigated by Huang and Raissi [34]. Xinxin and Kaoru [35] studied the sulfur-iodine (S-I) cycle for hydrogen production using nuclear energy. Energy and economic assessment of an industrial plant for hydrogen production by sulfur-iodine thermochemical cycle was presented by Liberatore et. al [36]. The efficiency of the thermochemical cycle by itself was about 34%, based on higher heat value. If this value is associated with the electrical energy production, including the

efficiency of the solar plants, the total heat-to-hydrogen efficiency was obtained to be 21%.

The potential of sustainable hydrogen production through solar energy and thermochemical cycles was examined by Graf et al. [37]. A metal oxide based cycle and a hybrid sulfur cycle were compared with the commercial electrolysis, and a sensitivity analysis was carried out for different cost scenarios.

Granovskii et al. [38] presented a comparative performance assessment through thermal and hydrogen production efficiencies of the combined system including a supercritical water-cooled nuclear reactor and a chemical heat pump. The combined system can provide high temperature heat to a thermochemical water splitting cycle of hydrogen production.

Alternative thermochemical cycles of hydrogen production were evaluated by Lewis et al. [11-13]. Their results showed that the copper-chlorine cycle is chemically viable and feasible with respect to engineering energy-efficient.

Dincer and Balta [28] have discussed several potential and hybrid cycles for nuclear-based hydrogen production. The copper-chlorine cycle was shown to be a highly promising cycle for nuclear-based hydrogen production.

Recent advances in thermochemical cycles of hydrogen production, using non-fossil energy sources such as nuclear or solar, were reported by Rosen [9]. Numerous advances have been made on sulfur-iodine cycle and the copper-chlorine cycle was shown to have significant potential because of the lower temperature requirement for heat supplies compared to most other thermochemical processes.

2.3 Copper-chlorine thermochemical cycle

The copper-chlorine (Cu-Cl) cycle was identified as a promising low-temperature cycle for hydrogen production [11-13]. The Cu-Cl cycle decomposes water into hydrogen and oxygen, through intermediate copper chloride compounds, in a closed loop that recycles all chemicals continuously. There are three variations of the Cu-Cl cycle, based on the number of main chemical reactions: three step, four step, and five step. The schematic of the four step cycle is shown in Figure 2-1.

The first step in the four step cycle Cu-Cl thermochemical cycle for hydrogen production is CuCl/HCl electrolysis:

$$2CuCl(aq)+2HCl(aq)\rightarrow H_2(g)+2CuCl_2(aq) \quad (2.1)$$

in which oxidation of copper(I) chloride , CuCl occurs during an electrochemical reaction, in the presence of hydrochloric acid, HCl, to produce hydrogen, H_2 and copper(II) chloride, $CuCl_2$. The Cu(I) ion is oxidized to Cu(II) at the anode, and the hydrogen ion is reduced at the cathode.

Step 2 of the cycle is the drying step:

$$CuCl_2(aq)\rightarrow CuCl_2(s) \quad (2.2)$$

Aqueous $CuCl_2$ exiting from the electrolysis cell is dried to produce $CuCl_2$ particles, which are then moved to the hydrolysis unit (step 3) and reacted with superheated steam to produce copper oxychloride solid, Cu_2OCl_2 and hydrochloric gas:

$$2CuCl_2(s)+H_2O(g)\rightarrow Cu_2OCl_2(s)+2HCl(g) \quad (2.3)$$

In step 4 (oxygen production step), copper oxychloride particles decompose into molten CuCl and O_2 gas:

$$Cu_2OCl_2(s) \rightarrow 2CuCl(l) + 1/2\, O_2(g) \quad (2.4)$$

Several variations of copper-chlorine cycles with different numbers of steps and methods of grouping were compared, and major features of the cycles with different numbers of steps were discussed by Wang et al. [39]. A detailed kinetic study of the hydrogen and oxygen production reactions in the Cu-Cl cycle was presented by Serban et al. [40]. Balta et al. [41] presented energy and exergy analyses of a four step Cu-Cl cycle, coupled with a geothermal source for hydrogen production. Wang et. al [42] compared sulfur-iodine and copper-chlorine thermochemical cycles from the perspectives of heat quantity, thermal efficiency, and related engineering challenges.

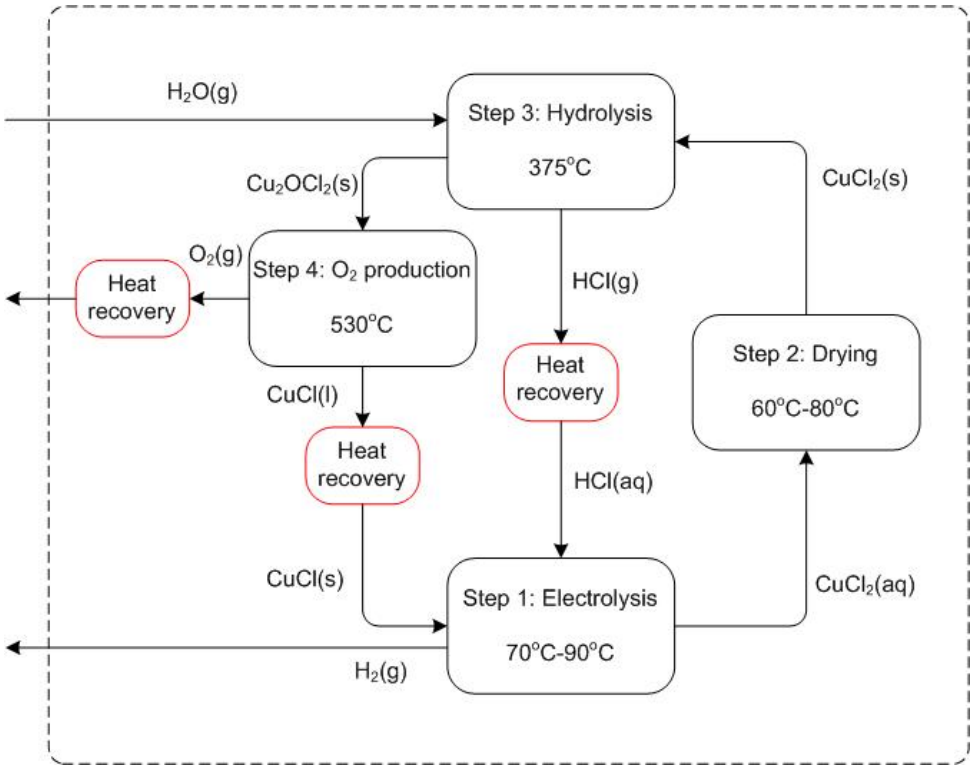

Figure 2-1 Schematic of the four step copper-chlorine cycle for thermochemical water splitting

A solar plant coupled with a Cu-Cl plant to produce hydrogen at three locations in Canada was analyzed by Ghandehariun et al. [43]. The results showed the feasibility of solar thermochemical Cu-Cl cycle as a promising and efficient pathway for large-scale hydrogen production.

Canadian advances in nuclear-based production of hydrogen by the Cu-Cl cycle were presented by Naterer et al. [44-47]. Orhan et al. [48] studied nuclear-based hydrogen production by a Cu-Cl hybrid cycle using sea or brackish water. Coupling of the Cu-Cl cycle with a desalination plant was analyzed in this study. Different desalination processes were reviewed to determine the most appropriate option for the Cu-Cl cycle. Their results assist the design and improvement of coupled systems. Cost analysis of a Cu-Cl thermochemical plant was presented by Orhan et al. [49]. The authors investigated the sensitivity of costs as a function of plant capacity, capacity factor, and percentages of each cost component.

Thermophysical properties of copper compounds in the Cu-Cl cycle were studied by zamfirescu et al. [50]. The environmental impacts of the Cu-Cl were presented by Ozbilen et al [51] using life cycle assessment.

Hydrolysis of $CuCl_2$ into Cu_2OCl_2 and HCl using a spray reactor was investigated by Ferrandon et al. [52]. It was shown that a counter-current flow reactor results in a significantly higher yield of Cu_2OCl_2 compared to a co-current flow, due to enhanced mass transfer.

Naterer et al [53] examined the evaporative drying of aqueous copper(II) chloride ($CuCl_2$) droplets in the copper-chlorine cycle. An aqueous $CuCl_2$ stream exiting

from an electrochemical cell was preheated to 150^{o}C, before entering a flash evaporator to produce solid $CuCl_2$. The results showed that benefits of flashing the solution to enhance drying were relatively minor, compared to evaporative drying in the spray drying process.

The thermal design of the oxygen production reactor for decomposition of copper oxychloride (Cu_2OCl_2) into oxygen gas and molten cuprous chloride was presented by Naterer et al. [54]. Wang et al [55] examined the scale-up design issues for the hydrogen, oxygen and hydrolysis reactors in the copper-chlorine cycle. Various design schemes for the overall copper-chlorine cycle and its components were investigated by Orhan et al [56], in order to identify potential performance improvements of the cycle.

2.4 Heat recovery in the copper-chlorine cycle

Heat recovery within the copper-chlorine cycle is crucial to the efficient performance and the overall viability of the cycle [45-47]. The heat requirements of different steps of the five step copper-chlorine cycle were evaluated by Naterer et al [54]. The authors examined the heat matching between the steps of the Cu-Cl cycle so as to recover as much heat as possible and minimize the net heat supply of the cycle. It was shown that if all released heat is recovered within the cycle, the efficiency of the cycle increases significantly [54].

Heat recovery from molten CuCl was studied by Jaber et al. [57]. A direct contact heat exchanger was proposed and the convective heat transfer between molten CuCl droplets in a counter-current spray flow was evaluated. The results showed that full

heat recovery can be achieved with a heat exchanger diameter of 0.13 m and heights of 0.6 and 0.8 m for a 1 and 0.5 mm droplet diameter, respectively.

The feasibility of using copper(I) chloride as a working fluid in a new high temperature heat pump with vapor compression was investigated by Zamfirescu et al. [58]. It was shown that CuCl can be used as a working fluid in a vapor compression heat pump, and the oxygen reactor of the copper-chlorine cycle can be linked with the CuCl heat pump system.

A heat exchanger design recovering heat from oxygen gas exiting the oxygen reactor of the copper-chlorine cycle was presented by Rabbani et al. [59]. Based on energy and exergy analysis, the best possible path for the recovered heat from oxygen was also examined.

A majority of heat recovery within the copper-chlorine cycle can be achieved by cooling molten CuCl exiting the oxygen reactor step of the cycle at about 530^{o}C. Since the melting point of CuCl is about 430^{o}C, solidification occurs as molten CuCl cools.

Two types of heat exchangers can be considered for heat recovery from molten CuCl: direct and indirect contact. In a direct contact heat exchanger (e.g. an atomization process) molten droplets are released from the top of the heat exchanger whereas air or steam flows upwards. The droplets are cooled and solidified during the descent. In an indirect contact heat exchanger (e.g. a casting/extrusion process), molten CuCl flows through an inner pipe while the coolant flows through the outer pipe.

2.5 Heat transfer and solidification in an atomization process

One of the possible processes of heat recovery from molten CuCl is atomization and solidification. The temperature transition of a solidifying droplet is of major importance the heat recovery process.

The forced convection heat transfer rate for a variety of process configurations have been studied in the past. For a flow past a single sphere, a steady-state conduction solution exits which yields [60]

$$Nu = 2 \tag{2.5}$$

provided that the sphere is immersed in an infinite media. To obtain a correlation for the Nusselt number, a functional dependence on Reynolds and Prandtl numbers is chosen as follows.

$$Nu - 2 = f(Re, Pr, \frac{\mu_\infty}{\mu_s}) \tag{2.6}$$

subject to the restriction that $f(Re) \rightarrow 0$ as $Re \rightarrow 0$. Richardson [61] recommended that the heat transfer from the sphere be considered as two parallel processes. In the laminar boundary layer region, the contribution to the Nusselt number should be of the form $Re^{1/2}Pr^{1/3}$, while in the wake region the contribution should be of the form $Re^{2/3}Pr^{1/3}$, so that Equation (2-6) could be expressed as

$$Nu - 2 = (aRe^{\frac{1}{2}} + bRe^{\frac{2}{3}})Pr^{\frac{1}{3}}\left(\frac{\mu_\infty}{\mu_s}\right)^c \tag{2.7}$$

On the basis of the work of Vliet and Leppert 62] and the supporting data of Kramers [63], the exponent on the Prandtl number is chosen to be 0.4 and the exponent

on the viscosity ratio is taken to be 1/4. The constants a and b are chosen to obtain a good fit with the experimental data. The final form of Equation (2-7) is [64]:

$$Nu - 2 = (0.4Re^{\frac{1}{2}} + 0.06Re^{\frac{2}{3}})Pr^{0.4}\left(\frac{\mu_\infty}{\mu_s}\right)^{1/4} \tag{2.8}$$

This expression has been compared with experimental data and the agreement was quite good, the scatter of the data around the correlation being ±30% at the worst. The ranges of values of the parameters are:

$$\begin{aligned} &3.5 < Re < 7.6 \times 10^4 \\ &0.71 < Pr < 380 \\ &1 < \frac{\mu_\infty}{\mu_s} < 3.2 \end{aligned} \tag{2.9}$$

A special case of convection heat and mass transfer from spheres relates to transport from freely falling liquid drops where the correlations of Ranz and Marshall [65] have been widely used.

When a droplet breaks away from the feeding system, it may oscillate in shape and have some internal motion caused by the formation process. As the droplet accelerates, internal circulation is created by the shear stress on the surface and aerodynamic forces tend to distort the shape of the droplet. Yao and Schrock [66] suggested a transient correction factor for the Ranz-Marshall correlation which accounts for the effects of vibration and distortion of the drop shape as it falls. The authors presented two methods to model the internal heat transfer of a droplet: one by solving the internal heat conduction equation and the other by assuming a uniform temperature within the droplet. The uniform temperature within the droplet is due to internal mixing of liquid

within the droplet. It is difficult to account precisely for contributions of drop distortion and internal resistance; however, the approximate empirical procedure developed by Yao and Schrock [66] gives accurate predictions for water droplets with diameters ranging from 3 mm to 6 mm.

Melissari and Argyropoulos [67] developed a numerical model to describe the transport phenomena involved when a melting sphere is immersed in a moving fluid. The model was used to predict the melting times of various spheres immersed in fluids with different Prandtl numbers. A dimensionless heat transfer correlation for forced convection over a sphere was proposed and the results were compared with experimental data for liquid metals and water.

Solidification is a particularly complicated process and very different from melting, because it requires three different steps [68]:

- Supercooling: The liquid has to be cooled to a certain temperature, called the nucleation temperature, which is generally lower than the melting temperature. The degree of supercooling ΔT is defined as the difference between the melting or equilibrium temperature and the nucleation temperature.

- Nucleation: This process is characterized by the formation of critical nuclei in the supercooled liquid. - Growth of the nuclei. This process can be limited by the viscosity of the liquid.

In industrial processes including the manufacture of solid spheres, such as atomization or prilling, an understanding of the temperature transition of the spheres is of prime importance. The heat flow conditions prevailing during solidification determine the

resulting microstructures of the solids, mostly in the case of atomization of metals. In the case of non-metallic substances, which are solidified in prilling towers (such as manures or washing powders), the time for complete solidification is a particularly important parameter

The analysis of the solidification of a droplet is of great importance in the study of spray crystallisation processes. Spray crystallisation can be simply described as the solidification of a liquid by atomization into a relatively cold atmosphere [69]. It is a process developed for the powder production of a range of materials such as foodstuffs [70], metals [71], pharmaceuticals [72], and the artificial production of snow [73].

There are two types of experimental techniques for the study of single droplets: free flight and levitation. Free flight studies involve allowing a droplet to free fall and measuring the variables by observation or catching the droplet at different heights [66]. In the levitation method, the droplet remains stationary while air flows past it. Levitation techniques may be non-intrusive or intrusive.

Non-intrusive levitation employs electromagnetic [75], electrostatic [76], or aerodynamic [77] forces to levitate the droplet freely. The non-intrusive methods have the advantage of better approximating actual conditions, but the experimental apparatus required is generally expensive. Intrusive methods involve suspending a droplet on a thin mesh or plate, or the junction a thermocouple. The suspension of droplets on thermocouples has been extensively used in past studies [78-80].

Several works have been performed in the field of solidification in atomization processes [81,82]. Liu et al. [83] investigated the droplet-gas interactions in spray

atomization of a Ta-2.5W alloy using nitrogen gas. A two-dimensional flow model and a lumped parameter formulation, based on the modified Newton's law of cooling, were developed to simulate the flow and heat transfer phenomena, including rapid solidification of droplets in the spray cone. It was assumed that the concentration of droplets in the atomization gas was sufficiently dilute, so that interactions between droplets were neglected. The gas flow was not solved, but an exponential correlation for the gas velocity distribution was assumed. Zeoli et al. [84,85] developed a numerical model, which combines both a cooling process and break-up, in an atomization process for powder production, in a single computation. The gas flow was computed using the commercial software FLUENT. The predictions demonstrated that droplets have very similar profiles during gas atomization. A major factor influencing the atomization and solidification processes of droplets is in-flight distance. In another study, a simulation method to predict the solidification of gas-atomized Sn-5% Pb (on a mass basis) droplets was developed by Li et al. [86]. The model predicts the mode of nucleation, the undercooling, the recalescence time and duration, the post-recalescence plateau duration, and the fraction of solid at the end of recalescence. They assumed a uniform droplet temperature during solidification and adopted the model proposed by DiVenuti [87] for the droplet temperature variation. However, unlike the present research, the objective of all these works was solidification, rather than heat recovery.

A number of studies on spray tower heat exchangers have been reported, concerning heat and mass transfer characteristics between dispersed and continuous phases. The dispersion of a PCM (phase change material) liquid and the solidification of PCM droplets in a heat exchange fluid with a low temperature was experimentally

investigated [88]. The solidification fraction of the solidified oil droplets was expressed in terms of the Stefan number, droplet Reynolds number, and non-dimensional temperature ratio. Song et al. [89] obtained an analytical solution for direct contact heat transfer between two immiscible liquids in a counter-current spray column. The explicit formulae for the column height required for complete evaporation, and the temperature of the continuous phase at the end of evaporation, were given. Recently, Jaber et al. [57,90] presented a predictive model of droplet flow and heat transfer from molten CuCl droplets in a counter-current spray flow heat exchanger. For a case with a CuCl flow rate of 3.4 g/s and air flow rate of 3 g/s, the required height of the heat exchanger is 0.6m (for droplets with a diameter of 1mm) and 0.8 m (for droplets with a diameter of 0.5mm). For both cases, the inlet and exit CuCl temperatures were 530^{o}C and 70^{o}C, respectively. The air stream had inlet and exit temperatures of 25^{o}C and 493^{o}C, respectively. The authors assumed that the temperature distribution within the droplet was spatially uniform. The presented results do not seem reliable. Therefore, futher analytical studies are required. Also, experiments need to be performed to investigate the feasibility of the process for heat recovery from molten CuCl.

2.6 Heat transfer and solidification in a pipe

As mentioned earlier, the casting/extrusion method is identified as a potentially advantageous method for recovering heat from molten CuCl. Modeling of the solidification during the casting process has been investigated by many authors [91-95]. Most assumed that conduction heat transfer was the main heat transport mechanism of significant importance, and convection heat transfer from the molten metal to the solid shell was not considered.

In past literature, a number of works have been reported to predict solidification of liquids flowing through pipes [96-98]. Sampson and Gibson [99] developed a mathematical model for solidification of a liquid metal with a low Prandtl number, flowing through a pipe maintained at a subfreezing temperature. In another study, Conde et al. [100] presented a two-dimensional model, using commercial software FLUENT, to analyse the freezing of water, olive oil, and aluminum in tubes under laminar conditions. The authors validated their model with experimental results of blocking lengths, provided earlier by Cheung and Baker [101]. Most of the previous researchers assumed a constant wall temperature. Recently, Seeniraj and Hari [102] studied the transient freezing of warm liquids flowing through convectively cooled pipes under laminar and turbulent flow conditions. In the limiting case, the results agreed with those reported earlier for steady state and constant temperature boundary conditions.

Chapter 3 Approach and Methodology

3.1 Approach

A thermal analysis of the four step copper-chlorine cycle is required to determine the heat recovery opportunities within the copper-chlorine cycle. It is shown that a majority of the heat recovery can be achieved by cooling molten copper(I) chloride. Heat recovery from molten CuCl is challenging due to the phase change of the material from liquid to solid as it cools. Solidification of molten CuCl during the cooling process will clog the equipment, hence conventional heat exchangers cannot be used.

Different devices for heat recovery from molten copper(I) chloride in the Cu-Cl cycle are presented. These options include atomization and steam generation with a quench bath, atomization and steam generation with a separate vessel, atomization and droplet descent in counter-current flow, atomization by air or other inert gases in concurrent flow, rotary/spinning atomization, casting/extrusion method, and drum flaker. Heat transfer rate, the potential of introducing extra substances into the cycle, energy efficiency and temperature retention, economics, material issues, design feasibility, and safety issues are considered in the evaluation of the methods. This comparative approach is by necessity approximate due to lack of practical data for the Cu-Cl cycle. Sufficient data is not available for performing an economic investigation. Nonetheless, casting/extrusion method seems to be the most cost-effective method. Based on present comparative assessment, casting/extrusion configuration, atomization with separate vessel using water as a coolant, and rotary/spinning atomization using air as a coolant are

recognized as the most advantageous. processes of heat recovery from molten CuCl in the copper-chlorine cycle.

Casting/extrusion method represents an indirect-contact heat transfer from the molten CuCl. A mathematical model is developed to analyze an indirect-contact heat exchanger. This is a counter-current double-pipe heat exchanger in which the molten CuCl flows through the inner pipe while the coolant flows through the outer pipe. Solidification during heat transfer from the molten material is investigated in modeling of the system. Both laminar and turbulent flow conditions are studied.

Afterwards atomization method is investigated. This method includes a direct contact heat transfer process from the droplets of molten CuCl to the coolant. A predictive model is presented to model solidification of molten CuCl droplets during the falling. The model can be used in developing a heat recovery system design for a thermochemical hydrogen production plant.

3.2 Methodology

Pinch analysis is used to determine the heat distribution and the maximum recoverable heat within the Cu-Cl cycle, and how heat recovery can be integrated effectively into the overall cycle.

For a casting/extrusion method (i.e., indirect contact heat recovery), the governing equations are normalized by defining dimensionless variables. For the laminar flow condition, the energy equation is solved analytically to obtain the spatial bulk mean temperature. For the turbulent flow condition, the normalized equations are solved numerically using finite difference method.

For an atomization method (i.e., direct contact heat recovery process), a four-stage solidification model is developed analytically. Each stage is investigated separately. The prediction of the temperature transition of each stage is undertaken by balancing the internal energy of the droplet against the heat loss to the environment. Established methods of modeling heat and mass transfer are employed in this study. Two models are used to predict the temperature of the droplet during the flight. The first model solves the internal heat conduction equation while the second model assumes a uniform temperature distribution within the droplet. Experimental studies are also performed to examine the behavior of molten CuCl in a direct-contact heat recovery system, and investigate the feasibility of the process for heat recovery from molten CuCl.

3.3 Assumptions and simplifications

Major assumptions and simplifications employed in the modeling of are presented in this section. Other assumptions and simplifications, that are limited to specific stages of the research, are identified at the appropriate points in the thesis. For an indirect contact heat recovery process, the following assumptions and heat exchangers are used [99-102].

- It is assumed that the heat exchanger is well insulated. Therefore heat loss from the heat exchanger to the surroundings is negligible.

- It is assumed that the liquid bulk mean temperature reaches a steady-state distribution instantaneously as the freeze-front radius changes. This assumption is believed to be reasonable for turbulent flows and Prandtl numbers higher than 0.5.

- The axial growth of the solidified layer is much slower than the rate of change of the temperature of the liquid with time. This allows us to neglect the time derivative of the temperature in the heat conduction equation for the solid layer.

- The axial conduction in the solid layer is negligible with respect to the bulk transport in the axial direction. This is valid for fluids with Pr>0.5.

- Fully developed flows are assumed throughout the tubes.

- CuCl properties are assumed to be constant at the melting point.

For a direct contact heat transfer modeling, the following assumptions are applied [66,78]:

- CuCl vapor is assumed to behave as an ideal gas.

- It is assumed that the droplet shape is constant and spherical during the falling.

- The solid fraction is assumed to increase uniformly within the droplet.

Chapter 4 Pinch Analysis for Recovering Thermal Energy in the Copper-chlorine Cycle

4.1 Introduction

Pinch analysis is a methodology for minimizing the energy consumptions of processes, by calculating thermodynamically feasible energy targets, and achieving them by optimizing heat recovery systems, energy supply methods, and process operating conditions. This method is also known as a process integration or pinch technology [103-111].

The pinch analysis has been first developed for studying energy savings in the chemical process industry [107]. Since then, the pinch analysis has been applied in many industrial sectors where thermal operations occur [111-114]. This analysis offers a systematic approach to optimum energy integration in a process. One of the key advantages of pinch analysis is the ability to set an energy target which is the minimum theoretical energy demand for the overall process. The principle objective of this analysis is to match cold and heat process streams with a network of heat exchangers so that demands for externally supplied utilities are minimized. The best design for an energy-efficient heat exchanger network will result in a trade-off between the energy recovered and the capital costs involved in the energy recovery [103].

In this chapter, the pinch analysis is used to compute the maximum recoverable heat within the copper-chlorine cycle, and areas where heat recovery is beneficial.

Different options for using the recovered heat in the copper-chlorine cycle are also explored [115].

4.2 Pinch analysis concepts

In this section, the key concepts of pinch analysis are presented. The starting point for a pinch analysis is to identify all the process streams that need to be heated and all those that need to be cooled. This means identifying the streams, their flow rates and thermal properties, phase changes, and the temperature ranges through which they must be heated or cooled. A differential heat flow (dQ), when added to a process stream, increases its enthalpy (H) by CdT, where C is the heat capacity rate and dT is differential temperature change. With C assumed constant, the total heat added to bring a cold stream from a supply temperature (T_S) to a target temperature (T_T) is equal to the stream enthalpy change [98]:

$$Q = \int_{T_S}^{T_T} C\,dT = C(T_T - T_S) = \Delta H \tag{4.1}$$

This allows plotting of the temperature versus enthalpy to provide a composite curve of all streams that require a heat source. The same procedure is followed to prepare a composite curve of the streams to be cooled. The slope of the line representing the stream is:

$$\frac{dT}{dH} = \frac{1}{C} \tag{4.2}$$

In reality, the heat capacity generally tends to increase with temperature, resulting in some curvature in the curves. However, the use of temperature-dependent

properties does not change the heat integration method; only the details of the computations are changed [103].

Since we are mainly concerned with enthalpy changes of streams in the present analysis, a given stream can be plotted anywhere on the enthalpy axis, provided it has the same slope and runs between the same supply and target temperatures. For feasible heat exchange between the two streams, the hot stream must be at all points hotter than the cold stream, so it should be plotted above the cold stream. The cold stream should be shifted on the H-axis relative to the hot stream so that the minimum temperature difference (ΔT_{min}) is positive and finite. The overlap between the composite curves represents the heat recovery target, while the needs for external heating and cooling are represented by the non-overlapping segments of the cold and hot composite curves, respectively.

To handle multiple streams, the heat loads or heat capacity rates of all streams existing over any given temperature range are added together. So a single composite of all hot streams and a single composite of all cold streams are produced on the T-H diagram. For a given value of ΔT_{min}, the quantities predicted are the minima required to solve the heat recovery problem. ΔT_{min} occurs at the point of closest approach, which is called the pinch. The optimum value for ΔT_{min} is generally in the range of 10-40 K. For a given ΔT_{min}, the composite curves define the utility cooling and heating duties. The composite curves can be used to evaluate the overall tradeoff between energy and capital costs. An increase in ΔT_{min} causes an increase in the energy costs, but also provides a larger driving force for heat transfer which yields a reduction in capital costs [103].

4.3 Thermal analysis of the copper-chlorine cycle

The heat requirements for the four steps of the copper-chlorine cycle are evaluated in this section. Table 4-1 summarizes the four steps of the Cu-Cl cycle along with the temperature range of each step [45].

Table 4-1 Reaction steps in the Cu-Cl cycle

Step	Reaction	Temperature Range (K)
1	$2CuCl(aq)+2HCl(aq)\rightarrow H_2(g)+2CuCl_2(aq)$	343-363
2	$CuCl_2(aq)\rightarrow CuCl_2(s)$	333-353
3	$2CuCl_2(s)+H_2O(g)\rightarrow Cu_2OCl_2(s)+2HCl(g)$	648
4	$Cu_2OCl_2(s)\rightarrow 2CuCl(l)+1/2\,O_2(g)$	803

The heat required for drying aqueous $CuCl_2$ is 122 kJ/mol H_2, including the heat required for vaporizing water and the enthalpy of dissolution [54]. The sensible heat requirement for increasing the temperature of $CuCl_2(s)$ from 298 K to 648 K is calculated as follows:

$$2\int_{298}^{648} C_p^{CuCl_2} dT = 53.47 \frac{kJ}{mol\ H_2} \tag{4.3}$$

where C_p is found from the following correlation [116]:

$$C_p^{CuCl_2} = 70.21882 + 23.36132t - 14.86876t^2 + 4.053899t^3 - 0.366203/t^2 \tag{4.4}$$

Here, t is equal to $T/1000$.

The heat required for steam production in the hydrolysis step is 57.8 kJ/mol H_2, which consists of the heat required for increasing the temperature of water from 298 K to 373 K, vaporizing water at 373 K, and increasing the temperature of steam from 373 K to 648 K. The specific heat for liquid and water vapor is calculated by using Equations (4.5) and (4.6) respectively [116]:

$$C_p^{H_2O(l)} = -203.6060 + 1523.290t - 3196.413t^2 + 2474.455t^3 + 3.855326/t^2 \tag{4.5}$$

$$C_p^{H_2O(g)}=30.09200+6.832514t-6.793435t^2-2.534480t^3+0.082139/t^2 \quad (4.6)$$

The heat of reaction for hydrolysis is:

$$\Delta H_f(Cu_2OCl_2)+2\Delta H_f(HCl)-2\Delta H_f(CuCl_2)-\Delta H_f(H_2O)=80.68\ \frac{kJ}{mol\ H_2} \quad (4.7)$$

The heat released during cooling of HCl from 648 K to 298 K is 2.47 kJ/mol H_2.

Copper oxychloride exiting the hydrolysis step at 648 K should be heated to 803 K to be used as a reactant in the oxygen production step. The heat required is 17.81 kJ/mol H_2. C_p is calculated based on the following correlation [117]:

$$C_p^{Cu_2OCl_2}=99.23243+21.62162t \quad (4.8)$$

Similar to Equation (4-7), the heat of reaction for step 4 is found to be 138.39 kJ/mol H_2. The heat released during cooling and solidification of molten CuCl is 74.74 kJ/mol H_2. This includes the heat required for cooling molten CuCl from 803 K to 703 K, the heat of solidification at 703 K, and the heat required for cooling solidified CuCl to 298 K. C_p for molten and solidified CuCl is calculated using the following correlations [116]:

$$C_p^{CuCl(l)}=66.94400-3.699628\times10^{-10}t+2.166748\times10^{-10}t^2 -3.900460\times10^{-11}t^3-9.813196\times10^{-12}/t^2 \quad (4.9)$$

$$C_p^{CuCl(s)}=75.27100-26.83212t+25.69156t^2-7.357982t^3-1.847747/t^2 \quad (4.10)$$

The heat released during cooling of oxygen gas from 803 K to 298 K is 7.97 kJ/mol H_2. C_p of the oxygen is calculated from the following equations [116]:

$$C_p^{O_2}=31.32234-20.23531t+57.86644t^2-36.50624t^3-0.007374/t^2 \quad (4.11)$$

$$C_p^{O_2}=30.03235+8.772972t-3.988133t^2+0.788313t^3-0.741599/t^2 \quad (4.12)$$

Equation (4.11) is valid for the temperature range 100 - 700 K, and Equation (4.12) is valid for the temperature range 700 – 2,000 K.

4.4 Pinch analysis for internal heat flows

Table 4-2 shows the distribution of heat requirements in the Cu-Cl cycle, based on a hydrogen production rate of 3 kg/day. About 18% of the total heat requirement for the cycle can be recovered within the cycle. About 88% of the heat recovery can be achieved by cooling and solidifying molten CuCl. Heat recovery from HCl is less than 3% of the total recovered heat in the cycle, hence it is not considered. The theoretical temperature-enthalpy diagram with $\Delta T_{min} = 0$ is shown in Figure 4-1. The cold stream represents the heat required for vaporizing water from $CuCl_2$(aq), heating $CuCl_2$(s), producing steam, providing the hydrolysis heat of reaction, heating Cu_2OCl_2 and providing the heat of reaction for Cu_2OCl_2 decomposition. Vertical dashed lines separate different steps of the cycle in the cold stream. The hot stream represents the heat released during cooling and solidification of molten CuCl and cooling of O_2 gas. Heat losses to the environment are not considered here.

In practice, a positive minimum temperature difference between the hot and cold stream is required for heat transfer. There are two approaches to provide the required minimum temperature difference. In the first approach (see Figure 4-2), the cold stream is shown to be shifted on the H-axis so that $\Delta T_{min} = 40$ K. The heat recovery region is shown on the graph by vertical dashed lines. The hot stream is plotted above the cold stream since it has a higher temperature. As also shown in table 4-2, the total heat released in the cycle is not sufficient to provide the total heat requirement of the cycle.

From Figure 4-2, 1.24 kW of the heat recovery rate from molten CuCl and oxygen gas can be used in the drying step. About 0.2 kW of the heat recovery rate cannot be used due to an insufficient temperature difference between the hot and cold streams. Hence 6.92 kW of external heating is required for the remainder of the cycle.

The second approach is to divide the hot stream into two separate parts (see Figure 4-3). The high temperature part is shifted on the H-axis relative to the cold stream to reach the minimum temperature difference of 40 K. Two separate heat recovery regions are shown by vertical dashed lines in Figure 4-3. In this case, 0.38 kW of the heat recovery rate is used in the drying step and 0.86 kW for heating the reactants of the hydrolysis reaction. As noted above, 0.2 kW of the heat recovery rate is not usable within the cycle.

Table 4-2 Heat distribution in the Cu-Cl cycle (without considering internal heat recovery)

Step	Sum of heat input rates (kW)	Portion of total heat input rate (%)	Endothermic processes in step	Heat input rate breakdown for processes in step			Sum of heat output rates (kW)	Exothermic processes in step	Heat output rate breakdown for processes in step	
				kW	%				kW	%
1	0	0	-	0	0		0	-	0	0
2	2.12	26.0	Drying	2.12	100		0	-	0	0
3	3.33	40.8	Reaction	1.4	42		0.04	Cooling HCl	0.04	100
			Heating $CuCl_2$	0.93	28					
			Superheated steam generation	1	30					
4	2.71	33.2	Reaction	2.4	89		1.44	Cooling O_2	0.14	10
			Heating Cu_2OCl_2	0.31	11			Cooling CuCl	1.3	90
Total	8.16	100					1.48			

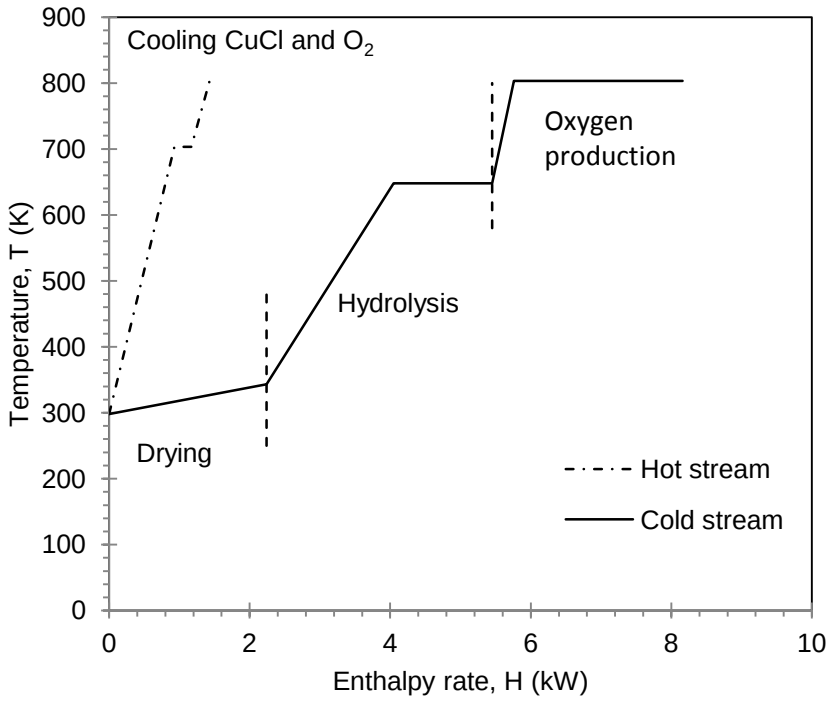

Figure 4-1 Temperature-enthalpy diagram with $\Delta T_{min} = 0$

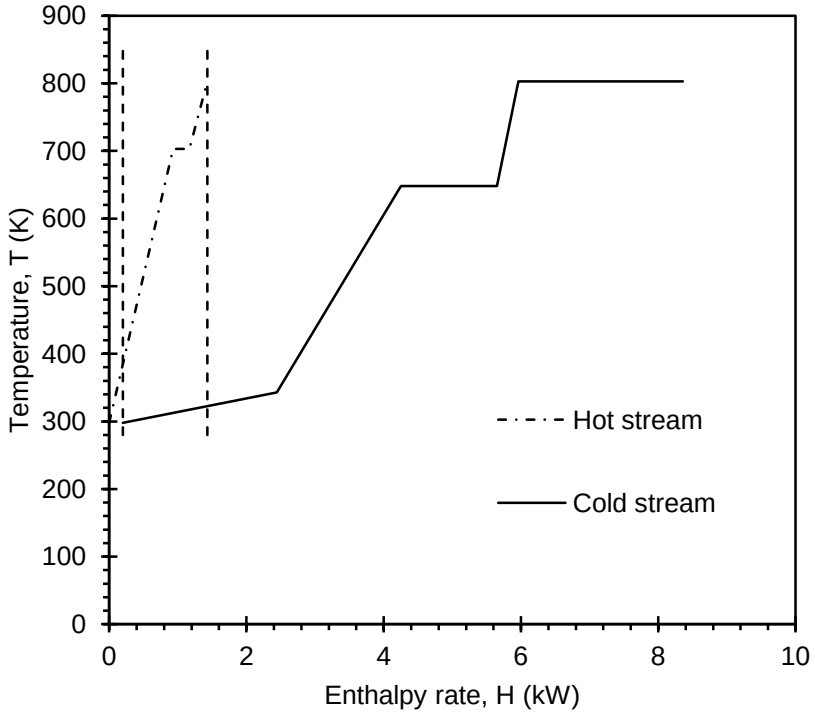

Figure 4-2 Temperature-enthalpy diagram with $\Delta T_{min} = 40$ K

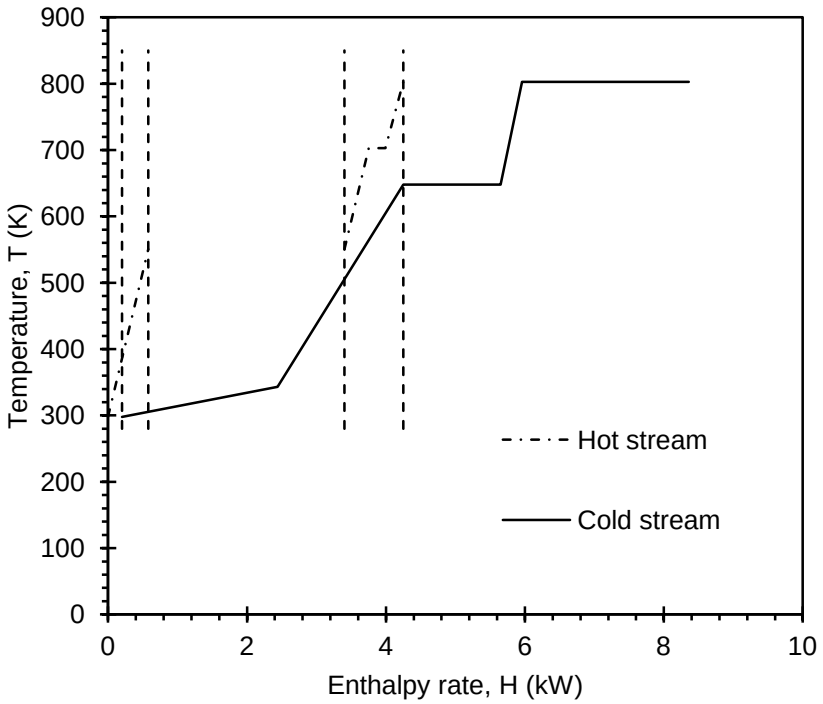

Figure 4-3 Temperature-enthalpy diagram with two heat recovery regions

4.5 Layout options for the integration of internal and external heat flows

The pinch analysis and heat flow profiles presented in the previous section provide a solid basis for the study of heat recovery. However, the pinch analysis is applicable to internal heat flows and based on ideal assumptions that no heat losses exist. As for the external hot stream that transports heat by a heat transfer fluid from a nuclear reactor or a solar thermal plant to the Cu-Cl cycle, as shown in Table 4-1, the temperature requirement for step 4 (oxygen production step) is 803 K, which means that the heat transfer fluid (external hot stream) entering the cycle must be significantly higher than 803 K, and the heat transfer fluid still has a temperature of over 803 K when it exits step 4. Considering the driving temperature difference for efficient heat transfer, the minimum temperature exiting step 4 could be reasonably assumed as 823 K. If it is higher than 823 K, the inlet temperature of

the Cu-Cl cycle may be raised. The same situation exists for step 3 (hydrolysis) and the minimum outlet temperature, T_{32}, can be assumed as 668 K, which is 20 K higher than the reaction temperature 648 K, so as to provide the heat transfer driving temperature. However, the outlet temperature of step 3 could also be adjusted to be higher than 648 K to meet the heat requirement of the downstream step. As for step 2, the temperature requirement is 333-353 K, which is about 300 K lower than the exiting temperature of the heat transfer fluid for step 3. Therefore, the exiting temperature for step 2 is flexible in the engineering design. Figure 4-4 shows a flowchart for the external hot stream. The inlet temperature (T_i) of the cycle depends on the heat sources and pipeline heat losses, and the outlet temperatures T_{32} of step 3 and T_o of the cycle can be adjusted so as to meet the heat distribution requirement of Table 4-2.

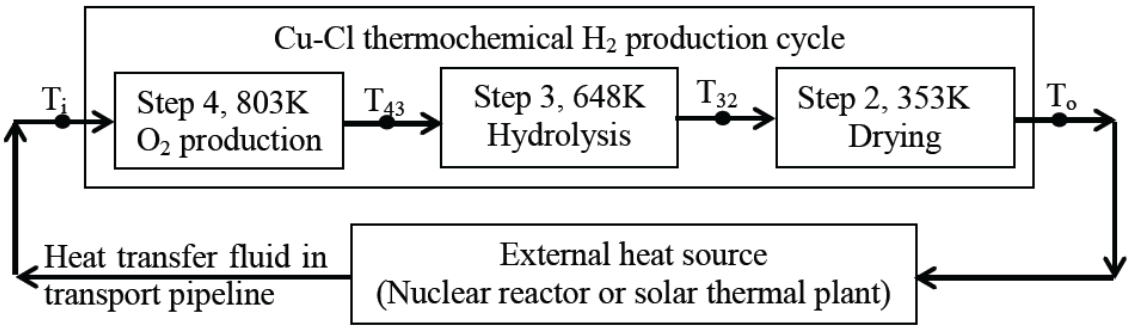

Figure 4-4 External heat flows from heat source to the thermal steps of Cu-Cl cycle

Assuming the external heat transfer fluid does not undergo phase change when passing through the Cu-Cl cycle and the heat capacity of the heat transfer fluid does not change significantly in the temperature range of interest, the percentage of heat transferred to each step of the cycle, presented in Table 8-1, depends mainly on the temperature

difference. Therefore, the following equations can be written for heat percentages of steps 4 and 3:

$$\frac{T_i - T_{43}}{T_i - T_o} \times 100 = 33.2\% \qquad T_{43} > 823 \text{ K} \tag{4.13}$$

$$\frac{T_{43} - T_{32}}{T_i - T_o} \times 100 = 40.8\% \quad T_{32} > 668 \text{ K} \tag{4.14}$$

The values of $T_{32}$and T_{43} are set to 668 K and 823 K, respectively. From Equations (4.13) and (4.14), the values of T_i and T_o are found to be 949 K and 569 K, respectively. If the heat source cannot provide the temperature of 949 K, the flow rate of the heat transfer fluid must be increased to meet the required heat quantity of step 4. Considering the available temperature of various heat sources, the temperature of 949K is not practical in industry. For example, the maximum outlet temperature of supercritical water-cooled reactors (SCWRs) planned for the future is 898-923 K, and the maximum temperature of current solar thermal plants is 823 K [118,119]. Considering heat losses in the pipeline, the temperature will be reduced further. Therefore, the inlet temperature for step 4 must be lowered. If the internally released heat is transported to steps 2 and 3 of the cycle, assuming that the heat recovery efficiency is about 60%, the heat requirement of the Cu-Cl cycle will change, as shown in Table 4-3.

Table 4-3 Heat distribution in the Cu-Cl cycle (considering internal heat recovery)

Step	Heat input rate (kW)	Portion of total heat input rate (%)
1	0	0
2	1.9	25.6
3	2.81	37.9
4	2.71	36.5
Total	7.42	100

The values of T_i and T_{43} are set to 903 K and 823 K, respectively. Applying the heat input percentages of Table 4-3 to Equations (4.13) and (4.14), the values of T_{32} and T_o are found to be 740 K and 684 K, respectively. Figure 4-5 shows the layout of internal and external heat flows. Table 4-4 summarizes the temperature distribution with and without internal heat recovery. The inlet temperature of 903K can then likely be satisfied by future SCWRs. In addition, the heat "quality" leaving of Cu-Cl cycle is enhanced by 100 K, which can allow it to be used for other purposes, e.g., to drive a gas turbine or generate steam for a steam turbine.

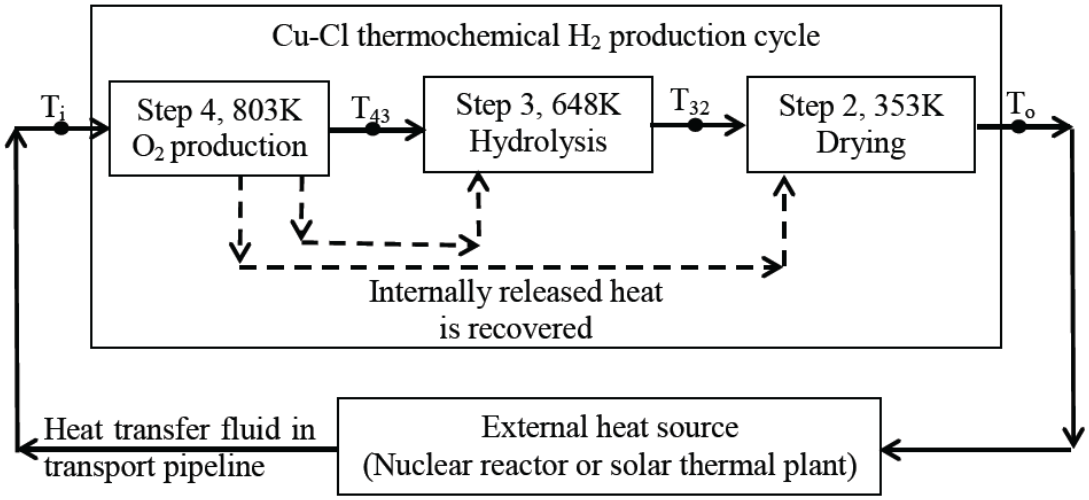

Figure 4-5 Layout for external and internal heat flows for the Cu-Cl cycle

Table 4-4 Temperature distribution in the Cu-Cl cycle considering internal heat recovery

Temperature	Inlet temperature of Cu-Cl cycle, T_i, K	Outlet temperature of hydrolysis, T_{32}, K	Outlet temperature of Cu-Cl cycle, T_o, K
No heat recovery	949	668	569
60% of internal heat is recovered and transferred to steps 2 and 3	903	740	684

4.6 Closing remarks

In this chapter, the pinch analysis is used to find the maximum heat recovery within the copper-chlorine cycle, and where in the cycle the recovered heat can be used efficiently. It is shown that about 88% of the heat recovery can be achieved by cooling and solidifying molten cooper(I) chloride exiting the oxygen reactor step. Two options for using the recovered heat in the Cu-Cl cycle are presented. All of the recovered heat can be used in the drying step, or 58% of heat recovery can be used to in the hydrolysis and the remainder in the drying step. The second option is shown to be more appropriate. It is also shown that by transferring 60% of the recovered heat to steps 2 and 3, inlet temperature of the Cu-Cl cycle can be decreases from 949 K to 903 K, while outlet temperature of the cycle increases from 569 K to 684 K. In the next chapters, several configurations for heat recovery from molten CuCl will be presented and predictive models will be developed to investigate the selected methods.

Chapter 5 Methods of Heat Recovery from Molten Copper(I) Chloride

5.1 Introduction

As discussed in the previous chapters, recovering heat during the solidification of molten copper(I) chloride is crucial to the efficient performance of the copper-chlorine cycle. A number of processes for recovering heat from molten CuCl will be discussed [120,121], and assessed in terms of applicability to the Cu-Cl thermochemical cycle for hydrogen production. These methods are based on existing industrial processes for molten materials, which were developed for heat recovery from molten CuCl in the copper-chlorine cycle. A comparative assessment will be presented to find the most promising processes for heat recovery from molten CuCl. It is assumed that there is no CuCl loss in the cycle. However, in reality, additional supply or recovering CuCl in the cycle may be required to compensate for the CuCl loss.

5.2 Atomization and steam generation with a quench bath

This process, as shown in Figure 5-1, involves the atomization of molten CuCl in high temperature steam [122]. The atomized salt falls into a quenching water bath. During the descent, the droplets or particles of CuCl further transfer their residual heat to the upward flowing steam. The goal of this process is to generate high temperature steam with the atomization process, and low temperature steam when solidification is finalized in the quench bath. Another goal of this method is to avoid introducing other atomization gases

into the Cu-Cl cycle. Since CuCl has little reactivity with water and has weak solubility in water, the mixture of CuCl and water can be directly produced for the preparation of the aqueous solution of CuCl for the copper-chlorine cycle.

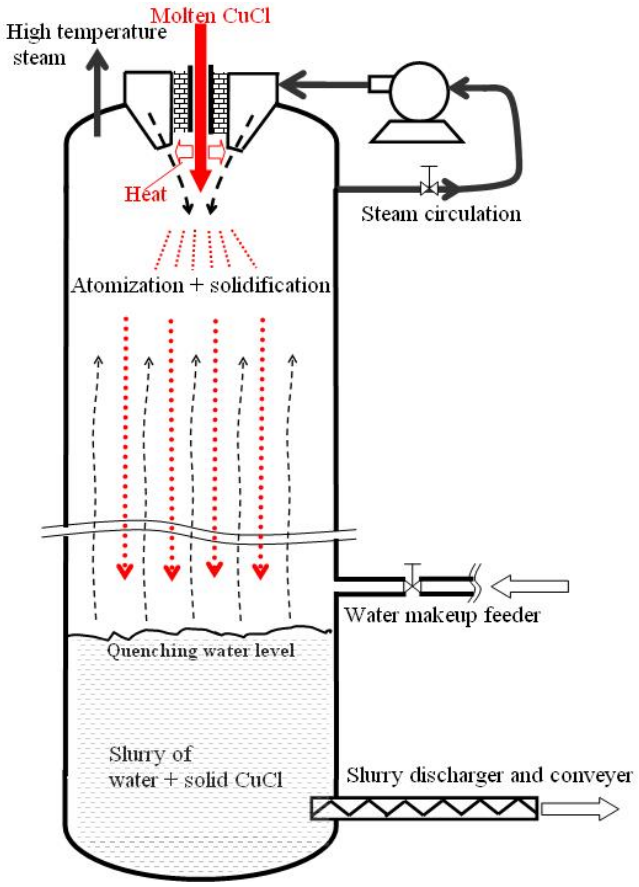

Figure 5-1 Atomization and steam generation with quench bath

In this process, high temperature steam will be diluted by saturated water vapor rising from the quench bath. This will limit the steam production to saturated steam, unless the vessel is pressurized.. If the vessel needs to be pressurized, then the molten CuCl will also need to be pressurized. This can be achieved with molten salt pumps. This would entail high cost components due to the high temperature and corrosivity of the working fluid. When liquid water is present in the system, it is not possible to generate superheated

steam. A superheater would be required to raise the temperature and pressure of the steam prior to recirculation to the atomizer. Heat losses will also be experienced in the steam circulation loop (through blower, ducting, valves, buffer and settlement tanks, among other components). The dimensions of the droplets, or the solidification extent before the droplets fall into the water bath, should prevent a steam explosion [123]. To reduce the build-up of CuCl salt on the vessel walls, the diameter of the vessel should be large enough, or the vessel walls can be rapped with rapping hammers, which create vibrations and dislodge solidified material.

5.3 Atomization and steam generation with a separate vessel

This method is similar to the previous method, however the quench bath is removed from the granulation vessel and CuCl is solidified completely in the vessel freeboard. It forms a bed of hot solid particles (see Figure 5-2). Solids from this bed are then discharged by a conveyor to a quenching vessel, and steam from the quenching vessel flows into the granulation vessel.

This method allows the generation of superheated steam due to the absence of a water bath in the atomization vessel. Moreover, the control of droplet dimensions is not critical because the risk of steam explosion is eliminated. However, this method requires corrosion protection to discharge high temperature solid CuCl particles.

5.4 Atomization and droplet descent in counter-current flow

This approach is based on a method used to make lead shot and ball bearings. In this process, molten material is dropped through a vessel (see Figure 5-3). As the material falls, it naturally breaks up, or is shaken into smaller droplets which solidify before reaching the

bottom of the vessel. A counter-current air flow is used to recover heat from the process. A fluidized bed at the base of the column could be used to remove the additional latent energy.

Pumping CuCl to the top of the vessel may be difficult due to chemical attack on piping and pump components, and the need to keep the material at elevated temperatures to prevent solidification during transport. This may consume an excessive amount of power. The viscosity of CuCl changes from 2.6 mPa.s at 436^{o}C to 1.7 mPa.sat 627^{o}C [50]. Comparing with the viscosity of water which is about 0.9 mPa.s at 25^{o}C, the viscosity of molten CuCl could not be problematic in pumping. Integration of this process into the complete Cu-Cl cycle may require the previous step to be carried out at an elevation. This would avoid pumping of molten CuCl.

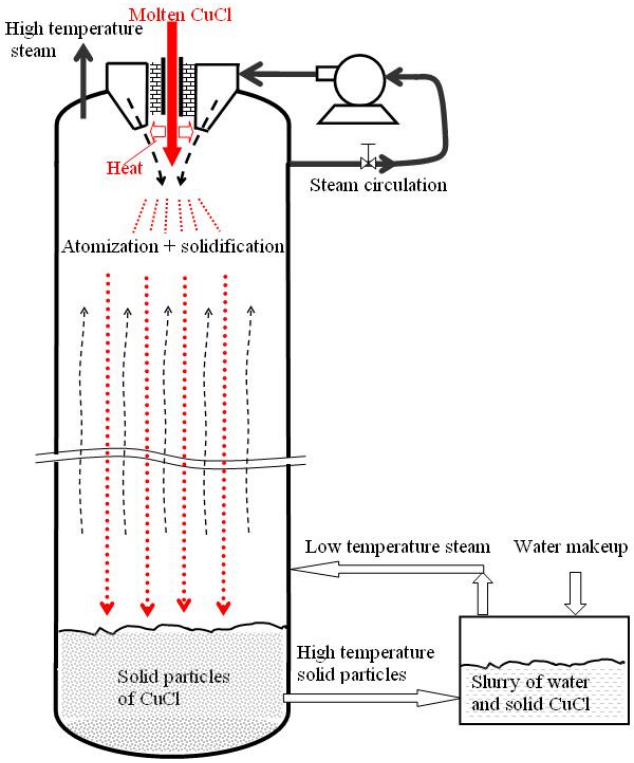

Figure 5-2 Atomization and steam generation with a separate vessel

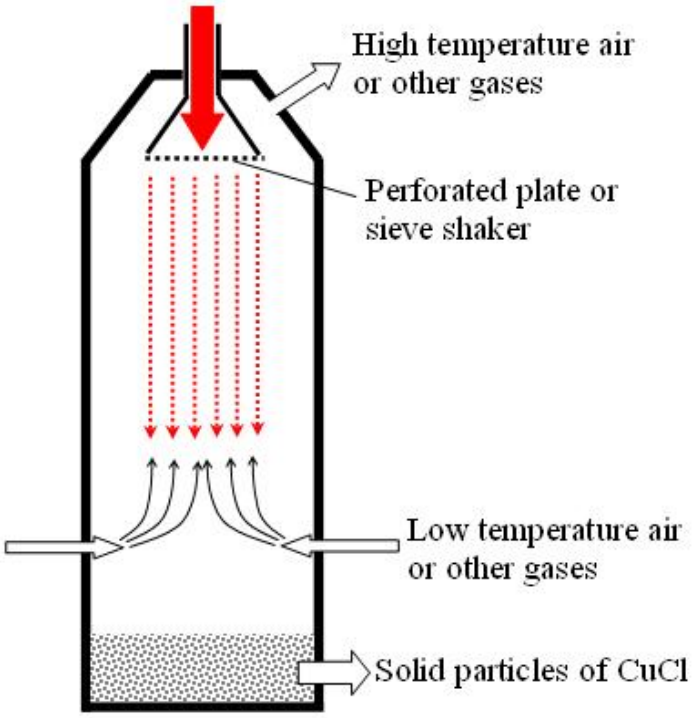

Figure 5-3 Atomization by falling through counter-current flow

5.5 Atomization and solidification by air or other inert gases in co-current flow

In this method, shown in Figure 5-4, molten CuCl is granulated through atomization, and solidification with air or an inert gas. Hot gas produced by the process is intended to supply heat to downstream processes. Horizontal arrangements may need larger horizontal space with respect to the molten salt trajectory and atomization behavior. A build-up of CuCl on equipment and vessel walls should be avoided as noted earlier. This is more difficult to achieve with a horizontal configuration, compared with a vertical configuration. Entrainment of hot CuCl dust in the air to downstream equipment with hot gas could become a problematic issue. Entrained dust could be captured by a cyclone separator that is placed immediately downstream of the air outlet.

In another possible process, the molten salt is mixed with water and sprayed into a vessel. The droplets should be solidified before coming into contact with the walls of the vessel.

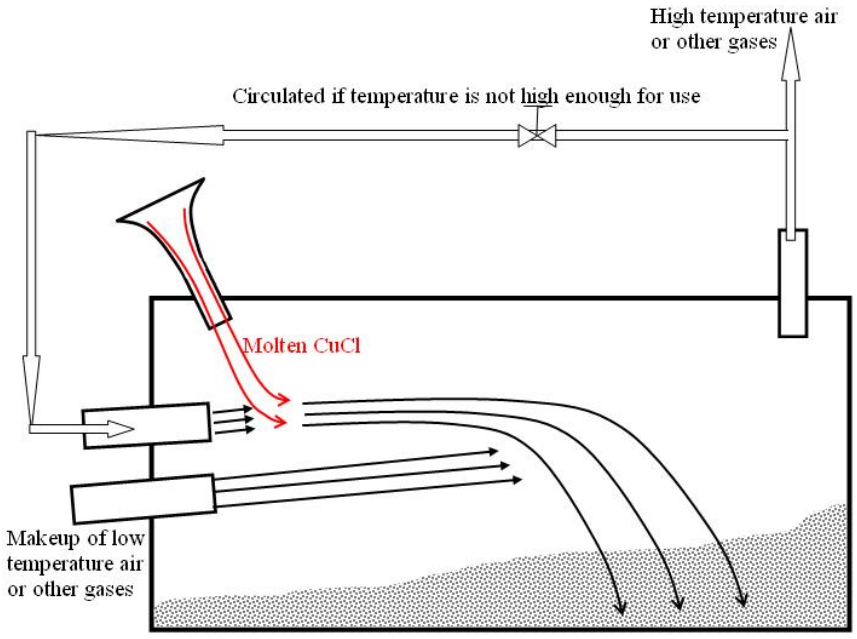

Figure 5-4 Atomization and solidification by air or other inert gases

5.6 Rotary/spinning atomization

In this method, as illustrated in Figure 5-5, a nozzle introduces the molten salt at the centre of a spinning disk or rotary cup. A centrifugal force carries the fluid to the edge of the disk and throws the fluid off the edge. The liquid forms sheets that break into droplets. The spray pattern tends to move radially away from the disk or cup in all directions.

The reactivity of molten CuCl should be considered in choosing the materials of the moving parts in contact with the salt. Like previous methods, the diameter of the vessel should be large enough to avoid build-up of the molten salt on the walls. The transport of CuCl dust through the hot gas exit should also be considered.

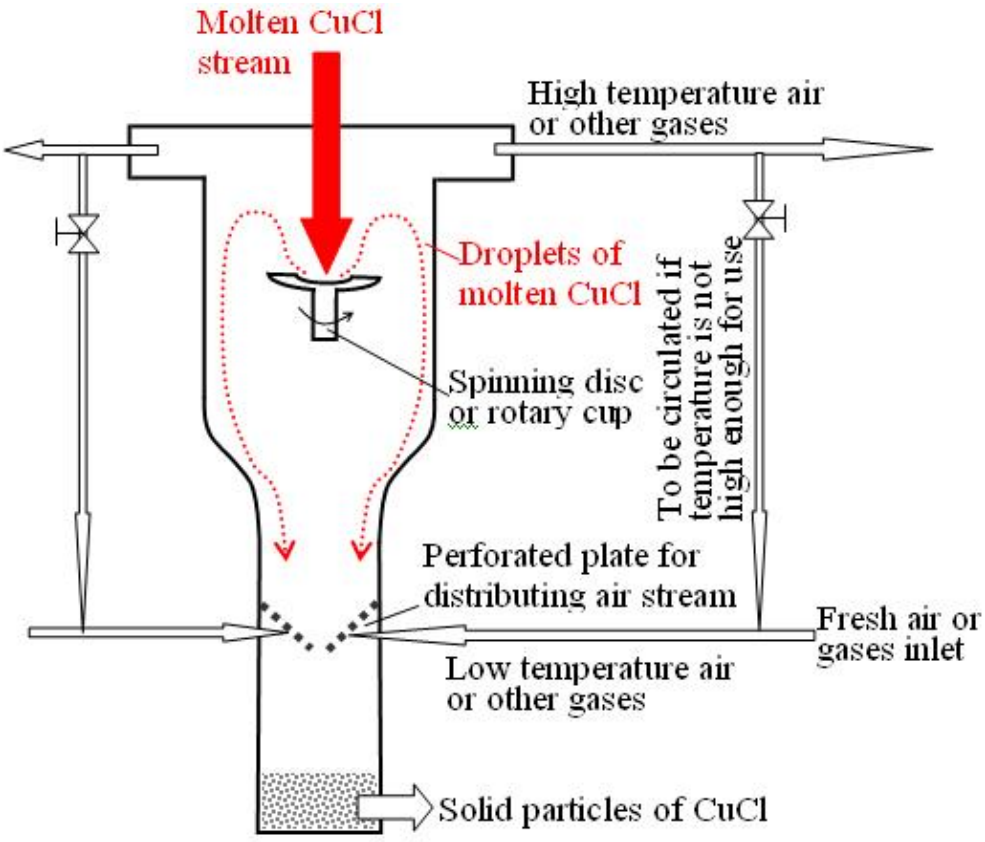

Figure 5-5 Rotary/spinning atomizer

5.7 Casting/extrusion method

The system consists of a channel which is cooled by a coolant (Figure 5-6). A similar process is used for steam generation in a molten salt nuclear reactor except that the molten salt in a molten salt reactor always retains a molten state.

Molten material flows through the channel. A screw extruder, similar to the extrusion method in processing of plastics, is set into the solidified material at the exit of the channel. Once the molten material is cooled and solidified, it is removed by the extruder to prevent plugging of the channel. An alternative way to remove the solidified material is to use a flexible scraping pull bar at the bottom of the channel.

This method seems simpler and more compact than atomization methods. Materials that can withstand molten CuCl should be considered in the present application.

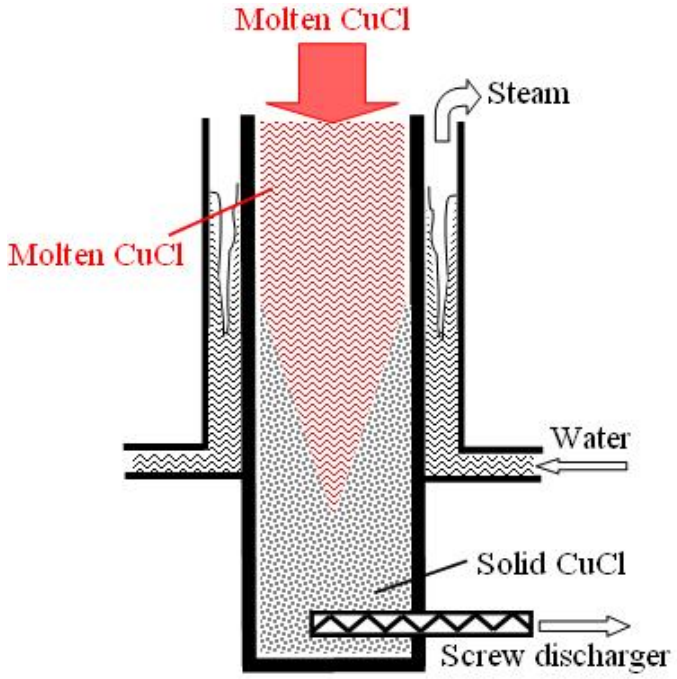

Figure 5-6 Casting/extrusion method

5.8 Drum flaker

Drum flakers are used commercially to solidify melts continuously. A typical drum flaker is shown in Figure 5-7. The solidification of the molten material is accomplished by applying a layer of material onto the outer surface of a hollow metal cylinder rotating around a horizontal axis, while the inner surface is cooled by a coolant [124]. The material is solidified, cooled and removed by a knife or blade. In this operation, the surface temperature of the drum is controlled to be lower than the melting point of the molten salt. The coolant could be air, other gases or water. At the time when air passes through the inside wall of the rotary drum, the molten salt would solidify at the outside wall of the drum and form a solid layer.

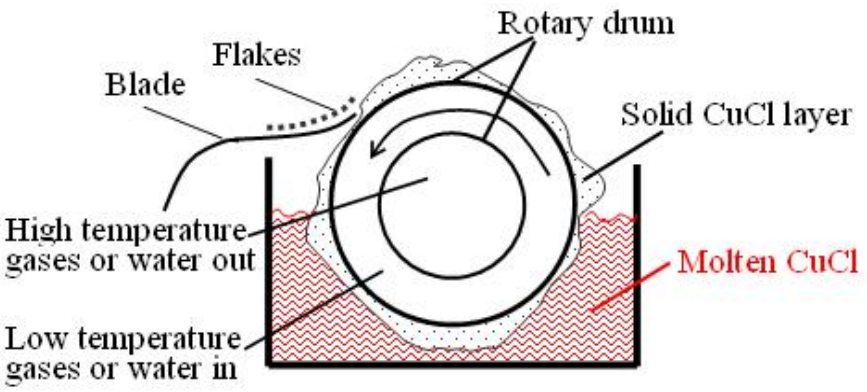

Figure 5-7 Drum flaker

5.9 Comparative assessment of heat recovery processes

The objective of this section is to comparatively assess the methods discussed previously for recovering heat from molten CuCl in the Cu-Cl thermochemical cycle of hydrogen production (see Table 5-1). The assessment yields a ranking of the methods, from most to least advantageous. This comparative analysis is required to limit the number of heat recovery options examined to a tractable number of processes which are most likely to be beneficial.

The comparative assessment was done using the following approach. Various parameters are considered in the ranking of the proposed methods. In each category, if a method has a considerable advantage in comparison with other methods, it is given a score of (+1). If a method has a significant disadvantage compared with other presented methods, it is given a score of (-1) in that category. If the method does not seem to be advantageous or disadvantageous, a score of (0) is given. In case where available data are inadequate to perform a comparative assessment, it is considered as “unknown”. The results of the present comparative analysis are given in Table 5-1. Table 5-1 is a two-part table, with the second part showing a horizontal continuation of the first part.

Regarding heat transfer, three parameters are considered: secondary heat exchanger, heat flux, and heat transfer area. In water systems, the heat is recovered by water which can be used in the cycle directly and an additional heat exchanger is not required. Therefore, these systems were given a score of (+1) in the category of secondary heat exchanger. In air systems, an extra heat exchanger is required to use the recovered heat in the cycle. This additional heat exchanger will reduce the overall efficiency and increase the costs. Thus, these methods are given a score of (-1) in the category of secondary heat exchanger.

The heat transfer coefficient of cooling with water is much more than that of air. In the quench bath, since the water is boiling, its temperature is 100^{o}C, so the temperature of the CuCl droplets will potentially reduce to 100^{o}C, while in other methods, the CuCl temperature cannot be reduced as low as 100^{o}C. Therefore, atomization with quench bath and separate vessel are given a score of (+1) in the category of heat flux. In the rotary/spinning atomization method, since the droplets fall on the plates, the heat flux is more than falling through a counter-current flow. Therefore, rotary/spinning atomization is given a score of (+1) while atomization by falling through counter-current flow is given a score of (0) in the category of heat flux. Co-current flow has a lower heat flux in comparison with counter-current flow. Therefore, atomization by air through a co-current flow is given a score of (-1) in the category of heat flux. In casting/extrusion and drum flaker methods, because of indirect contact between the molten salt and coolant, the overall heat transfer coefficient is potentially less than that in other methods. Therefore, considering the fact that the heat transfer coefficient in water systems is more than that in air systems, a comparative assessment yields casting/extrusion method and drum flaker

with water be given a score of (0). The drum flaker with air is given a score of (-1) in the category of heat flux.

The heat transfer area in atomization methods is more than casting/extrusion, which is more than that of a drum flaker. Therefore all atomization methods are given a score of (+1) while casting/extrusion method is given a score of (0) and drum flaker is given a score of (-1) in the category of heat transfer area.

Another parameter considered was the introduction of any additional chemical or substances into the cycle. The substances in the copper-chlorine cycle are copper, chlorine, hydrogen, and oxygen. Introducing any extra substances into the cycle will make the cycle more complicated. Also additional equipments may be required to use the recovered heat in different steps of the cycle. This may reduce the overall efficiency of the cycle. Therefore, it is desirable to avoid introducing any extra substances into the cycle. Therefore, air systems were given a score of (-1) in the corresponding category as they introduce air into the cycle. Water systems were given a score of (+1) in the category corresponds to introduction of extra substances to the cycle.

It seems that energy efficiency (percentage of recovered heat from molten CuCl) is very similar in different methods, except a drum flaker where insulation is very difficult as explained e. Therefore, drum flaker was given a score of (-1) in the category of energy efficiency while other methods were given a score of (0).

In atomization with a quench bath, it is required to pressurize the whole vessel to produce high temperature steam; otherwise a very tall vessel is needed. Therefore producing high temperature steam is difficult. Regarding a drum flaker, pressurizing the

rotating component is also challenging. In addition, since the contact area between the coolant and molten salt gets fresh frequently, producing high temperature water or air is difficult. Other methods are similar in the case of temperature retention. Therefore, atomization with quench bath and drum flaker were given a score of (-1) while other methods were given a score of (0) in the category of temperature retention.

Regarding economics, sufficient data were not available for comparing the methods. However, it appears that the casting/extrusion method is simpler than the drum flaker, whereas a rotating mechanism and sealing are more challenging. Therefore, casting/extrusion was given a score of (+1) and drum flake was given a score of (-1) in the category of economics.

All methods except the drum flaker are similar, regarding the materials in contact with CuCl. The material of the drum, because of its rotation, is challenging. Also, in the methods that use air as a coolant, corrosion from the working fluid is an issue. Therefore, drum flaker and all air methods were given a score of (-1) while other methods were given a score of (0) in the category of materials.

In the design category, three factors are considered: complexity of the system, ease of scale-up and ease of pressurization. Regarding complexity of the system, the atomizer is an issue in all atomization methods. Therefore, all atomization methods were given a score of (0) while casting/extrusion was given a score of (+1) in the category of complexity. A rotating mechanism and sealing are challenging for the drum flaker. Therefore, this method was given a score of (-1) in the complexity category.

Atomization systems which use air as a coolant are much easier for scaling up than water systems, hence these methods were given a score of (+1) in the category of scale-up. Scale-up of the casting/extrusion method is also challenging, as designing an extruder with a large diameter is challenging, hence this method was given a score of (-1) in the corresponding category. Atomization methods with water were given a score of (0) in the category of scale-up.

Regarding pressurization, increasing the pressure of steam is more difficult than that of air. Therefore, air atomization systems were given a score of (+1) while water systems were given a score of (-1) in the category of pressurizing. In a drum flaker, because of its rotating mechanism, pressurizing is more difficult. Considering the fact that pressurizing of air is easier than steam, drum flaker with water was given a score of (-1) while drum flaker with air was given a score of (0) in the pressurizing category.

Regarding safety, two parameters were considered: explosion and risk of injury. In all water systems, steam explosion is an issue because of sudden exposure of molten CuCl to water. Therefore, all of these methods were given a score of (-1) in the corresponding category. In addition, in water systems, potential injury is more serious than air systems, if an accident happens. Therefore, all water systems were given a score of (-1) in the category of injury, while air systems were given a score of (-1).

Table 5-1 Comparison of various methods of heat recovery from molten CuCl (continued horizontally below)[1]

Method	Heat transfer			Introduction of extra substances to the cycle	Desired product		Economics	Material
	Secondary heat exchanger	Heat flux	Heat transfer area		Energy efficiency	Temperature retention		
Atomization with quench bath	(+1)	(+1)	(+1)	(+1)	(0)	(-1)	Unknown	(0)
Atomization with separate vessel	(+1)	(+1)	(+1)	(+1)	(0)	(-1)	Unknown	(0)
Atomization by falling through counter-current flow	(-1)	(0)	(+1)	(-1)	(0)	(0)	Unknown	(-1)
Atomization by air (co-current flow)	(-1)	(-1)	(+1)	(-1)	(0)	(0)	Unknown	(-1)
Rotary/spinning atomization	(-1)	(+1)	(+1)	(-1)	(0)	(0)	Unknown	(-1)
Casting/extrusion	(+1)	(0)	(0)	(+1)	(0)	(0)	(+1)	(0)
Drum flaker	Water:(+1) Air:(-1)	Water:(0) Air:(-1)	(-1)	Water:(+1) Air:(-1)	(-1)	Water:(0) Air:(-1)	(-1)	(-1)

Table 5-1 Continued

Method	Design			Safety		Total
	Complexity of system	Ease of scale-up	Ease of pressurizing	Explosion	Risk of injury	
Atomization with quench bath	(0)	(0)	(-1)	(-1)	(-1)	(0)
Atomization with separate vessel	(0)	(0)	(-1)	(-1)	(-1)	(+1)
Atomization by falling through counter-current flow	(0)	(+1)	(+1)	(0)	(0)	(0)
Atomization by air (concurrent flow)	(0)	(+1)	(+1)	(0)	(0)	(-1)
Rotary/spinning atomization	(0)	(+1)	(+1)	(0)	(0)	(+1)
Casting/extrusion	(+1)	(-1)	(+1)	(-1)	(-1)	(+2)
Drum flaker	(-1)	(-1)	Water:(-1) Air:(0)	Water:(-1) Air:(0)	Water:(-1) Air:(0)	Water:(-7) Air:(-10)

(1) As mentioned in the text, in each column, a qualitatively score of (+1) is given to a method if the method has a considerable advantage in comparison with other methods. If the method has a significant disadvantage compared with other methods, it is given a score of (-1) in that column. If the method does not seem to be advantageous or disadvantageous, a score of (0) is given.

Finally, the scores given to each heat recovery process were added and a total score for each process was presented. Based on the total score obtained for each process, the methods can be ranked from the most to least advantageous. It is noted that all the parameters are weighted equally here, and the comparative assessment presented in this chapter is by necessity approximate due to the lack of practical data for the copper-chlorine cycle. Therefore, overlaps between different parameters which were defined and used in the present analysis may be recognized. This inaccuracy would make the utilization of weighting factors for different parameters pointless. When sufficient data for the Cu-Cl cycle are available, a more realistic comparison may be achieved by defining more appropriate parameters and introducing weighting factors to the parameters analyzed.

5.10 Closing remarks

In this chapter several processes for heat recovery from molten copper(I) chloride, based on existing industrial technologies for molten materials, are presented. These methods are assessed comparatively to find the most advantageous methods. Based on the comparative analysis presented in this chapter, the casting/extrusion process, atomization with separate vessel using water/steam as coolant, and rotary/spinning atomization using air as a coolant are recommended for further investigation. Casting/extrusion process can be considered as a double-pipe heat exchanger in which indirect contact heat transfer occurs, while atomization processes represent a spray column heat exchanger where direct contact heat transfer takes place. These two types of heat exchangers will be modeled analytically in the next chapter.

Chapter 6 Modeling of Selected Processes for Heat Recovery from Molten CuCl

6.1 Introduction

In the previous chapter, two heat recovery processes (i.e. casting/extrusion and atomization using air or steam) were recommended for further consideration. Based on the selected processes, two types of heat exchangers will be investigated in this chapter: indirect and direct contact types. In an indirect contact heat exchanger, the fluid streams remain separate and the heat transfers continuously through a dividing wall. In a direct contact heat exchanger, heat transfer occurs while the two fluid streams are in direct contact. Without a dividing wall, heat transfer between the two streams can take place across small thermal resistances. In addition, mass transfer can also occur.

6.2 Indirect contact heat recovery process

This section investigates the transient solidification of a hot liquid flowing through a pipe which is cooled by convection. This represents the casting/extrusion configuration that was presented in the previous chapter. Hot liquid enters the pipe at z=0 with a uniform temperature T_f, which is greater than the freezing temperature of the liquid, T_f (see Figure 6-1). A coolant at temperature $T_c < T_f$ is flowing in the shell side, counter-currently. The convection heat transfer coefficient of the coolant is assumed to be constant. The schematic of the problem is shown in Figure 6-1.

6.2.1 Governing equations

Solidification of a hot liquid flowing in a tube, subjected to an air flow with constant temperature, will be modeled. Later, a double-pipe heat exchanger in which air flows through the outer tube will be investigated. An instantaneous energy balance is applied to a differential element. The enthalpy drop of the flowing liquid is equal to the heat convection from the liquid to the growing solid layer.

$$-[\rho v_{in}(\pi r_i^2)]c_{p_l}(dT_b) = h_i\left(2\pi r_f dz\right)\left(T_b - T_f\right) \tag{6.1}$$

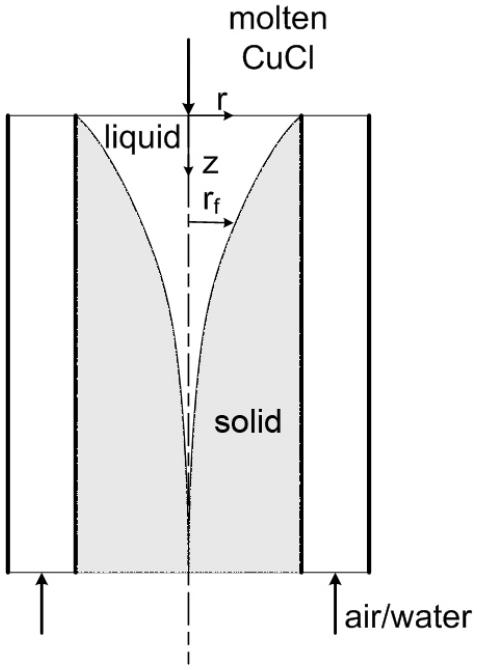

Figure 6-1 Schematic of a counter-flow heat exchanger with solidification

By introducing the following non-dimensional variables,

$$z^* = \frac{z}{r_i} \tag{6.2}$$

$$\theta_b^* = \frac{T_b - T_f}{T_{in} - T_f} \tag{6.3}$$

the energy balance becomes

$$Pe \frac{\partial \theta_b^*}{\partial z^*} + 2Nu_i \theta_b^* = 0 \tag{6.4}$$

where

$$Pe = Re\ Pr \tag{6.5}$$

$$Re = \frac{2\rho v_{in} r_i}{\mu} \tag{6.6}$$

$$Nu = \frac{2h_i r_f}{k_l} \tag{6.7}$$

At the solid-liquid interface, the sum of the heat released due to solidification, and the heat flux from the warm liquid to the solidified layer, is equal to the heat flux conducted through the solid layer.

$$-\rho_s \frac{\partial r_f}{\partial t} L + h_i (T_b - T_f) = k_s \left(\frac{\partial T_s}{\partial r}\right)_{r=r_f} \tag{6.8}$$

By introducing non-dimensional variables and parameters,

$$r^* = \frac{r}{r_i} \tag{6.9}$$

$$\tau = \frac{\alpha_s t}{r_i^2} \tag{6.10}$$

$$Ste_s = \frac{(T_f - T_c) c_{p_s}}{L} \tag{6.11}$$

$$Ste_l = \frac{(T_{in} - T_f)c_{p_l}}{L} \tag{6.12}$$

$$\theta_s^* = \frac{T_f - T_s}{T_f - T_c} \tag{6.13}$$

the non-dimensional form of equation (6-8) becomes

$$\frac{\partial r_f^*}{\partial \tau} = -Ste_s \left(\frac{\partial \theta_s^*}{\partial r^*}\right)_{r^*=r_f^*} + \left(\frac{\phi \theta_b^*}{r_f^*}\right) \tag{6.14}$$

where

$$\phi = 0.5 \left(\frac{C_p}{k}\right)_{sl} Ste_l Nu_i \tag{6.15}$$

As stated in Chapter 3, the axial growth of the solidified layer is slower than the rate of change of the temperature of the liquid with time. This allows us to neglect the time derivative of the temperature in the heat conduction equation for the solid layer. The axial conduction in the solid layer is negligible with respect to the bulk transport in the axial direction. Therefore, a quasi-steady condition in the solid layer can be assumed. The conduction equation and boundary conditions can be written as

$$\frac{\partial^2 T_s}{\partial r^2} + \frac{1}{r}\frac{\partial T_s}{\partial r} = 0 \tag{6.16}$$

$$T_s = T_f \quad at \quad r = r_f \tag{6.17}$$

$$-k_s \frac{\partial T_s}{\partial r} = h_o (T_s - T_c) \quad at \ r = r_i \tag{6.18}$$

It is noted that r_f in Equation (6.16) is a function of time and axial position.

The non-dimensional form of the equation and boundary conditions become

$$\frac{\partial^2 \theta_s^*}{\partial r^{*2}} + \frac{1}{r^*}\frac{\partial \theta_s^*}{\partial r^*} = 0 \tag{6.19}$$

$$\theta_s^* = 0 \quad at \;\; r^* = r_f^* \tag{6.20}$$

$$\frac{\partial \theta_s^*}{\partial r^*} = Bi(1 - \theta_s^*) \;\; at \;\; r^* = 1 \tag{6.21}$$

where

$$Bi = \frac{h_o r_i}{k_s} \tag{6.22}$$

The temperature distribution in the solid layer is

$$\theta_s^* = \left(\frac{Bi}{1 - Bi \; ln \; r_f^*}\right) Ln(\frac{r^*}{r_f^*}) \tag{6.23}$$

The value of $(\partial\theta_s^* / \partial r^*)_{r^*=r_f^*}$ is obtained from Equation (6.23) and substituted in Equation (6.14).

$$r_f^*(\frac{\partial r_f^*}{\partial \tau}) = -Ste_s(\frac{Bi}{1 - Bi \; lnR_f}) + \phi\theta_b^* \tag{6.24}$$

Equations (6.4) and (6.24) form a set of coupled non-linear partial differential equations with the initial and boundary conditions as follows:

$$\begin{cases} \theta_b^* = 1 \\ r_f^* = 1 \end{cases} at \; \tau = 0, z^* \geq 0 \tag{6.25}$$

$$\theta_b^* = 1 \;\; at \;\; z^* = 0, \tau \geq 0 \tag{6.26}$$

The solidification of the flowing hot liquid is possible only for a certain range of values of parameters. For solidification to commence, $(\partial r_f^* / \partial \tau)$ should be less than zero when $\tau \rightarrow 0$. Therefore, from Equation (6.24)

$$\left(\frac{\partial r_f^*}{\partial \tau}\right)_{\tau=0} = -Ste_s\, Bi + \phi \tag{6.27}$$

The condition for commencement of solidification is

$$Bi\ Ste_s > \phi \tag{6.28}$$

(*Bi Ste*$_s$) characterizes the amount of heat absorbed by the coolant and ϕ indicates heat transfer from the hot liquid by convection. Solidification would begin only when the heat extracted by the coolant is greater than the heat added by the liquid flowing in the pipe.

Using Equation (6.15), the limiting condition for solidification becomes

$$Bi\ Ste_{sl} > 0.5\left(\frac{C_p}{k}\right)_{sl} Nu_i \tag{6.29}$$

6.2.2 Solution method

6.2.2.1 Laminar flow

Considering laminar, fully developed conditions with a constant surface temperature, the Nusselt number is a constant [123].

$$Nu_i = 3.66 \tag{6.30}$$

The spatial distribution of the bulk mean temperature can be found by integrating Equation (6.4) with respect to z^*,

$$\theta_b^* = \exp\left(\frac{-7.32}{Pe} z^*\right) \tag{6.31}$$

Substituting Equation (6.31) into (6.24) yields

$$r_f^*\left(\frac{\partial r_f^*}{\partial \tau}\right) = -Ste_s\left(\frac{Bi}{1 - Bi\ Lnr_f^*}\right) + \phi \exp\left(\frac{-7.32}{Pe} z^*\right) \tag{6.32}$$

$r_f^*(z^*, \tau)$ is obtained by solving Equation (6.32) numerically.

The thickness of the solid layer reaches a steady state when the heat flux from the hot liquid at the interface is equal to the heat transfer to the coolant by convection. By replacing $\partial r_f^* / \partial \tau = 0$, Equation (6.32) becomes

$$-Ste_s \left(\frac{Bi}{1 - Bi\, Ln r_f^*} \right) + \phi \exp\left(\frac{-7.32}{Pe} z^* \right) = 0 \tag{6.33}$$

Therefore,

$$r_f^* = \exp\left[\frac{1}{Bi} - \frac{Ste_s}{\phi} exp\left(\frac{7.32}{Pe} z^* \right) \right] \tag{6.34}$$

6.2.2.2 Turbulent flow

The correlation proposed by Gnielinski for fully developed turbulent flow Nusselt number in a smooth tube [126] is modified to find *Nu* as a function of r_f^*, as follows.

$$Nu_i = 0.012 \left[\left(\frac{Re}{r_f^*} \right)^{0.87} - 280 \right] Pr^{0.4} \tag{6.35}$$

This correlation is valid over the following range of conditions:

$$\begin{cases} 1.5 \le Pr \le 500 \\ 3 \times 10^3 \le Re \le 10^6 \end{cases} \tag{6.36}$$

The Nusselt number obtained from (6.35) is substituted in Equations (6.4) and (6.24). These equations are solved numerically by employing the finite difference method. The effects of time step and mesh size on the numerical results are investigated. The optimum time step and mesh size are found as 0.01 and 0.001, respectively. Further

reduction of the time step and mesh size by a factor of 2 will cause up to 1% change in the computed results.

In the next stage, counter-current flow in the outer tube is considered. For fully developed laminar flow in the tube annulus, assuming that one surface is insulated and the other is held at a constant temperature, the Nusselt number is obtained from the tabulated data presented in Ref. [123]. An energy balance is applied to a differential element of the fluid.

$$\dot{m}_c C_{p_c} dT_c = -h_c(2\pi r_i dz)(T_w - T_c) \tag{6.37}$$

In each step, T_c is updated using Equation (6.37). Equations (6.4) and (6.24) are solved simultaneously as described above.

6.3 Direct contact heat recovery process

This section describes a mathematical model which predicts thermal behavior of a falling droplet during cooling and solidification.

6.3.1 Dynamics of the droplet

Newton's second law of motion for a freely-falling droplet gives:

$$m_d\left(\frac{dv}{dt}\right) = F_G - F_D - F_B \tag{6.38}$$

where v is the droplet velocity. F_G is the gravitational force:

$$F_G = m_d g \tag{6.39}$$

where g=9.81 m/s^2 is the gravitational acceleration. F_D is the drag force, defined as:

$$F_D = \frac{1}{2}\rho_d A_c C_D v^2 \tag{6.40}$$

where A_c is the cross-sectional area of the droplet:

$$A_c = \frac{\pi d^2}{4} \tag{6.41}$$

and C_D is the drag coefficient. F_B is the buoyancy force:

$$F_B = m_d g \frac{\rho_g}{\rho_d} \tag{6.42}$$

Substituting Equations (6.39), (6.40), and (6.42) into (6.38) gives:

$$m_d \left(\frac{dv}{dt}\right) = m_d g \left(1 - \frac{\rho_g}{\rho_d}\right) - \frac{1}{8}\pi d^2 \rho_g C_D v^2 \tag{6.43}$$

Assuming the drag coefficient to be constant, Equation (6.43) can be rewritten as:

$$a\left(\frac{d.}{dt}\right) + bv^2 - c = 0 \tag{6.44}$$

where the coefficients a, b, and c are:

$$a = m_d \tag{6.45}$$

$$b = \frac{1}{8}\pi d^2 \rho_g C_D \tag{6.46}$$

$$c = m_d g \left(1 - \frac{\rho_g}{\rho_d}\right) \tag{6.47}$$

Solving Equation (6.44), using the initial condition $v(t) = 0$, yields:

$$v(t) = \sqrt{\frac{c}{b}}\, tanh\left(\frac{\sqrt{bc}}{a} t\right) \tag{6.48}$$

Substituting Equations (6-45)-(6-47) into (6-48) gives:

$$v(t) = v_t tanh\left(\frac{g\left(1 - \frac{\rho_g}{\rho_d}\right) t}{v_t}\right) \tag{6.49}$$

where v_t is the terminal velocity at which the weight of the droplet is balanced by the upward buoyancy and drag forces. That is,

$$v_t = \sqrt{\frac{4gd}{3C_D}\frac{(\rho_d - \rho_g)}{\rho_g}} \tag{6.50}$$

Equation (6.50) is integrated over time to find the vertical position as a function of time:

$$y(t) = \frac{v_t^2}{g\left(1 - \frac{\rho_g}{\rho_d}\right)} ln\ cosh\left[\frac{g\left(1 - \frac{\rho_g}{\rho_d}\right)t}{v_t}\right] \tag{6.51}$$

Neglecting the buoyancy force, the solution to Equation (6.44) becomes:

$$v(t) = v_t tanh\left(\frac{gt}{v_t}\right) \tag{6.52}$$

where the terminal velocity v_t is:

$$v_t = \sqrt{\frac{4gd\rho_d}{3C_D\rho_g}} \tag{6.53}$$

Therefore, the vertical position of the droplet becomes:

$$y(t) = \frac{v_t^2}{g} ln\ cosh\left(\frac{gt}{v_t}\right) \tag{6.54}$$

Neglecting the drag and buoyancy forces, the acceleration of the droplet is constant and equal to the gravitational acceleration. This is a good approximation in air as long as the force of gravity is much greater than the force of air resistance and the velocity of the droplet is much less than the terminal velocity. In this case, the velocity and vertical position of the droplet become:

$$v(t) = gt \tag{6.55}$$

$$y(t) = \frac{1}{2}gt^2 \tag{6.56}$$

6.3.1.1 Drag coefficient

The conventional correlation for the drag on a sphere in steady motion is presented as a graph, called the standard drag curve, where C_D is plotted as a function of Re. Many empirical and semi-empirical equations have been proposed to approximate this curve [127].

Schiller and Nauman proposed the following correlation for $Re<800$:

$$C_D = \frac{24}{Re}(1 + 0.15Re^{0.687}) \tag{6.57}$$

The following equation was suggested by Langmuir and Blodgett for $1<Re<100$:

$$C_D = \frac{24}{Re}(1 + 0.197Re^{0.63} + 2.6 \times 10^{-4}Re^{1.38}) \tag{6.58}$$

Clift and Gauvin suggested the following correlation for $Re<3\times10^5$:

$$C_D = \frac{24}{Re}(1 + 0.15Re^{0.687}) + \frac{0.42}{1 + 4.25 \times 10^4 Re^{-1.16}} \tag{6.59}$$

The following correlation, recommended by Bailey and Hiatt can be used for $20<Re<260$:

$$C_D = \frac{24}{Re}[1 + 0.1935\ Re^{0.6305}] \tag{6.60}$$

6.3.2 Mass transfer from the droplet

Mass transfer is the transport of a component from one phase to another. It can happen either by evaporation or sublimation from the droplet surface. The rate of mass convection from a droplet can be expressed as [128]:

$$\dot{m} = h_m A(\rho_{v,s} - \rho_{v,\infty}) \tag{6.61}$$

where h_m is the mass transfer coefficient, A is the surface area of the droplet, and $\rho_{v,s}$ and $\rho_{v,\infty}$ are vapor density at the droplet surface and away from surface, respectively. The mass transfer coefficient is given by:

$$h_m = \frac{Sh\, D_{vg}}{d} \tag{6.62}$$

where Sh is the Sherwood number, D_{vg} is the vapor-gas mass diffusivity, and d is the droplet diameter.

The vapor-gas diffusivity is calculated from the following empirical equation [129]:

$$D_{vg} = \frac{10^{-3} T^{1.75} \left(\frac{1}{M_v} + \frac{1}{M_g}\right)^{\frac{1}{2}}}{P\left[\left(\sum V_v\right)^{\frac{1}{3}} + \left(\sum V_g\right)^{\frac{1}{3}}\right]^2} \tag{6.63}$$

where V is the special diffusion volume to be summed over atoms, T is temperature, and P is pressure. Table 6-1 lists the special atomic diffusion volumes.

Table 6-1 Special atomic diffusion volumes

Element	Diffusion volume
C	16.5
H	1.98
O	5.48
N	5.69
Cl	19.5
S	17

The Sherwood number can be calculated using the Ranz-Marshall equation [65]:

$$Sh = 2 + 0.6 Re_d^{\frac{1}{2}} Sc^{\frac{1}{3}} \tag{6.64}$$

where Sc is the Schmidt number, defined as:

$$Sc = \frac{\mu_g}{\rho_g D_{vg}} \tag{6.65}$$

Assuming the vapor to be an ideal gas,

$$\rho_v = \frac{P_v}{R_v T} \tag{6.66}$$

Equation (6-61) becomes:

$$\dot{m} = \frac{h_m A}{R_v}\left(\frac{P_{v,s}}{T_s} - \frac{P_{v,\infty}}{T_\infty}\right) \tag{6.67}$$

where R_v is the gas constant for the vapor and given by:

$$R_v = \frac{R_u}{M_v} \tag{6.68}$$

where R_u=8.314 J/mol.K is the universal gas constant and M_v is the molar mass of the vapor.

Using Chilton-Colburn analogy [128],

$$h_c = \rho c_p h_m Le^{\frac{2}{3}} \tag{6.69}$$

the mass transfer rate, Equation (6-61), becomes:

$$\dot{m} = \frac{h_c A}{\rho c_p Le^{\frac{2}{3}} R_v}\left(\frac{P_{v,s}}{T_s} - \frac{P_{v,\infty}}{T_\infty}\right) \tag{6.70}$$

where Le is the Lewis number, defined as:

$$Le = \frac{\alpha_g}{D_{vg}} \tag{6.71}$$

Here, α_g is thermal diffusivity of the ambient gas.

6.3.3 Heat transfer from the droplet

Heat transfer from the droplet occurs by three main mechanisms: convection heat transfer, mass transfer, and radiation heat transfer. The convection heat transfer rate from the droplet can be expressed as:

$$\dot{q}_c = h_c A(T_{d,s} - T_\infty) \tag{6.72}$$

where h_c is convection heat transfer coefficient, A is the droplet surface area, $T_{d,s}$ and T_∞ are the droplet surface and ambient gas temperatures, respectively. The convection heat transfer coefficient is calculated by:

$$h_c = \frac{Nu\, k_g}{d} \tag{6.73}$$

where Nu is the Nusselt number, k_g is the thermal conductivity of the ambient gas, and d is the diameter of the droplet.

Different correlations have been proposed for the average Nusselt number for flow over a sphere. Whitaker recommends the following comprehensive correlation [64]:

$$Nu = 2 + \left[0.4Re^{\frac{1}{2}} + 0.06Re^{\frac{2}{3}}\right] Pr^{0.4} \left(\frac{\mu_\infty}{\mu_s}\right)^{\frac{1}{4}} \tag{6.74}$$

which is valid for $3.5 \leq Re \leq 80{,}000$ and $0.7 \leq Pr \leq 380$. The fluid properties are evaluated at the free-stream temperature T_∞, except for μ_s which is evaluated at the surface temperature T_s. In Equation (6.74), Re is the Reynolds number and Pr is the Prandtl number, given by:

$$Re = \frac{\rho_g V d}{\mu_g} \tag{6.75}$$

$$Pr = \frac{C_{p,g}\mu_g}{k_g} \tag{6.76}$$

where V is the relative droplet-gas velocity, ρ_g and μ_g are the density and viscosity of the ambient gas, and $C_{p,g}$ is the gas heat capacity at constant pressure.

The following equation was suggested by Ranz and Marshall [65] for freely falling liquid drops:

$$Nu = 2 + 0.6Re_D^{\frac{1}{2}}Pr^{\frac{1}{3}} \tag{6.77}$$

In the limit $Re_D \rightarrow 0$, Equations (6.74) and (6.77) reduce to $Nu=2$, which corresponds to heat transfer by conduction from a spherical surface to a stationary infinite medium around the surface.

Yao and Schrock [66] proposed a correction factor that corrects the Ranz-Marshall equation for the effect of distortion of drop shape during the flight. The modified Ranz-Marshall equation is:

$$Nu = 2 + 15Re_D^{\frac{1}{2}}Pr^{\frac{1}{3}}\left(\frac{y}{d}\right)^{-0.7} \tag{6.78}$$

where y is the flight distance measured from rest. The equation is valid for $3\text{mm} \leq d \leq 6\text{mm}$ and $10 \leq y/d \leq 600$.

The heat transfer rate due to mass convection is given by:

$$\dot{q}_m = Lh_m A(\rho_{v,s} - \rho_{v,\infty}) \tag{6.79}$$

where L is the latent heat of phase change (evaporation or sublimation).

The heat transfer rate from the surface of the droplet due to thermal radiation is:

$$\dot{q}_r = \varepsilon\sigma A(T_{d,s}^4 - T_\infty^4) \tag{6.80}$$

where ε is the emissivity of the surface and σ=5.67×10^{-8} W/m^2.K^4 is the Stefan-Boltzmann constant. Equation (6.80) provides the difference between thermal energy that is released due to radiation emission and that which is gained due to radiation absorption.

There are many applications for which it is convenient to model the radiation mode in a manner similar to convection. In this sense, the radiation rate equation is linearized, making the heat rate proportional to a temperature difference rather than to the difference between two temperatures to the fourth power [126]. With this simplification, the net radiation heat exchange can be expressed as

$$\dot{q}_r = h_r A(T_{d,s} - T_\infty) \tag{6.81}$$

where the radiation heat transfer coefficient h_r is

$$h_r = \epsilon\sigma(T_s + T_\infty)(T_s^2 + T_\infty^2) \tag{6.82}$$

6.3.4 Modeling of droplet solidification

Solidification of a droplet can be described in four stages (see Figure 6-2) [78]:

1. Liquid cooling and supercooling: The liquid droplet is cooled from its initial temperature to a temperature below the equilibrium freezing point until crystal nucleation occurs.

2. Recalescence: Supercooling causes rapid crystal growth from the crystal nuclei. An abrupt temperature rise occurs due to liberation of latent heat of fusion. This stage is terminated when the droplet reaches an equilibrium freezing temperature.

3. Solidification: Further growth of solid phase, governed by the heat transfer rate from the droplet to the environment, continues until the droplet is completely frozen.

4. Solid cooling: The temperature of the solidified droplet reduces to a steady-state value near that of the ambient temperature.

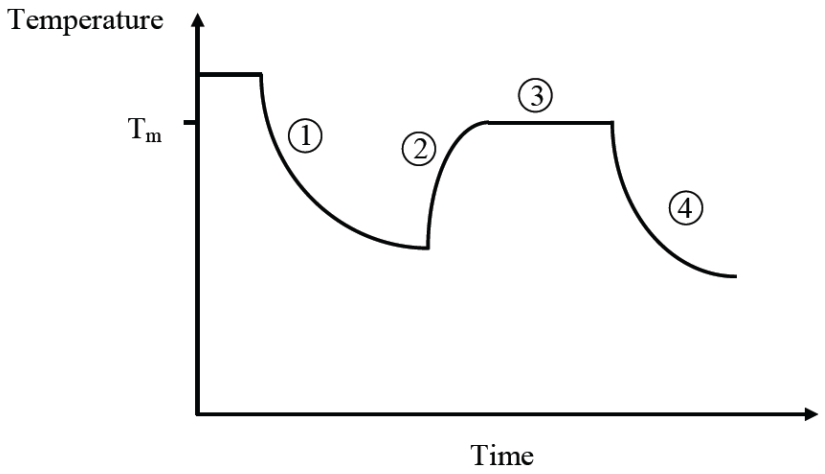

Figure 6-2 Temperature transition for the four stages of a droplet solidification

6.3.4.1 Cooling stages

The internal energy balance of the liquid and solid cooling stages (stages 1 and 4) can be solved by solving the internal heat conduction (i.e., non-mixing model) or assuming a uniform temperature distribution (i.e., complete-mixing model) [66].

6.3.4.1.1 Non-mixing model

The non-mixing model assumes that there is no internal motion in the droplet and the temperature distribution is governed by the heat equation. It is assumed that the droplet shape is constant and spherical; hence it can be described with a one-dimensional model.

The heat equation for one-dimensional transient heat conduction in a spherical droplet reduces to [125]:

$$\rho_d c_{p,d} \frac{\partial T}{\partial t} = \frac{\partial}{\partial r}\left(k_d \frac{\partial T}{\partial r}\right) + \frac{2k_d}{r}\left(\frac{\partial T}{\partial r}\right) \tag{6.83}$$

The initial and boundary conditions are as follows:

$$T(r, 0) = T_i \tag{6.84}$$

$$\left.\frac{\partial T}{\partial r}\right|_{r=0} = 0 \tag{6.85}$$

$$-k_d A_d \left.\frac{\partial T}{\partial r}\right|_{r=R} = \dot{q}_c + \dot{q}_m + \dot{q}_r \tag{6.86}$$

The solution to Equation (6.83), for convective boundary conditions is as follows [92]:

$$\theta^* = \sum_{n=1}^{\infty} C_n exp(-\zeta_n^2 Fo) \frac{1}{\zeta_n r^*} sin\,(\zeta_n r^*) \tag{6.87}$$

where θ* and r* are dimensionless temperature and spatial coordinate, respectively, defined as:

$$\theta^* = \frac{T - T_\infty}{T_i - T_\infty} \tag{6.88}$$

$$r^* = \frac{r}{R} \tag{6.89}$$

where T_i is the initial temperature, $T_\infty$is the ambient temperature, and R is the droplet radius. Fo is the Fourier number, defined as:

$$Fo = \frac{\alpha t}{r_0^2} \tag{6.90}$$

The discrete values of ζ_n are positive roots of the transcendental equation:

$$1 - \zeta_n cot\, \zeta_n = Bi \tag{6.91}$$

The first six routes of Equation (6.91) are presented in the Appendix. The values of coefficients C_n are determined from:

$$C_n = \frac{4(sin\zeta_n - \zeta_n cos\zeta_n)}{2\zeta_n - \sin(2\zeta_n)} \tag{6.92}$$

6.3.4.1.2 Complete-mixing model

This model assumes that the internal motion of the droplet is so vigorous that complete mixing is assumed. The temperature profile in the droplet is essentially flat and resistance to heat transfer exists only in the surrounding gas. Assuming uniform temperature for the droplet, the rate of temperature change is described by the heat balance between the droplet and the surrounding gas:

$$m_d c_{p,d} \frac{dT_d}{dt} = -(\dot{q}_c + \dot{q}_m + \dot{q}_r) \tag{6.93}$$

6.3.4.2 Recalescence stage

A droplet with a large undercooling at the time of nucleation, experiences a rapid temperature increase until it reaches the equilibrium freezing temperature, T_f. The heat balance gives:

$$\forall_s \rho_s L = \forall_d \rho_l c_{p,l} \left(T_f - T_n\right) \tag{6.94}$$

where $\forall_s$ is the volume of the solid produced from nucleation, ρ_s is the solid particle density, and L is the latent heat of fusion. The nucleation temperature, T_n is usually an empirical value. Therefore,

$$\forall_s = \forall_d \frac{\rho_l c_{p,l}}{\rho_s} \frac{\left(T_f - T_n\right)}{L} \tag{6.95}$$

6.3.4.3 Solidification stage

After nucleation produces a solidified volume fraction, solidifying of the remaining liquid is controlled by the heat transfer rate from the droplet. A heat balance model is used in this study. It is assumed that the solid fraction increases uniformly within the droplet as the latent heat of fusion is removed by external heat transfer. The droplet solidifies at a constant temperature T_f, hence the rate of solidification is given by the heat balance:

$$L\rho_s \frac{d\forall_s}{dt} = \dot{q}_c + \dot{q}_m + \dot{q}_r \tag{6.96}$$

The outer surface of the droplet is solid during this stage, so the mass transfer from the droplet is due to sublimation.

6.4 Closing remarks

In this chapter, predictive analytical models were developed to analyze an indirect contact and a direct contact system for heat recovery from molten CuCl. Since molten CuCl solidifies (at about 430^{o}C) as it cools, the solidification should be considered in the modeling of the heat recovery process. In an indirect contact heat recovery system (i.e a double-pipe heat exchanger), molten CuCl flows in the inner pipe while air or water flows through the outer pipe. The governing equations were derived and solved to predict the temperature distribution of the fluid as well as the thickness of the solid layer. In a direct

contact heat recovery system (i.e. a spray column), molten CuCl droplets are released from the top while air or steam flows from the bottom of the system. The velocity and flight distance equations for a freely-falling droplet were obtained. Heat transfer rate from a droplet surface was calculated, considering heat transfer due to convection, mass transfer, and radiation. Finally, a four stage solidification model was developed. The results, which will be presented in Chapter 8, will help design heat recovery systems for the copper-chlorine cycle.

Chapter 7 Experimental Studies

7.1 Apparatus

Figure 7-1 shows the experimental set-up for heat recovery from molten CuCl. A torch is used to melt CuCl and produce molten salt droplets in air. The droplets are then released into a vessel of water. A thermal imaging system is used to measure the temperature of the droplets during the descent. To investigate the possible reactions with air and water, the composition of the solidified product is determined using an X-ray diffraction system.

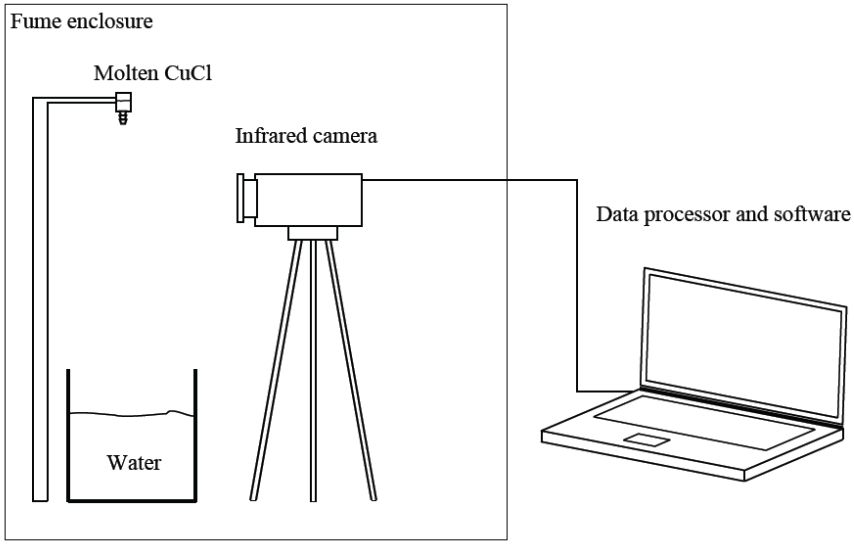

Figure 7-1 Schematic of the experimental set-up

7.1.1 Thermal imaging system

7.1.1.1 IR thermography

Although infrared radiation (IR) is not detectable by the human eye, an IR camera can convert it to a visual image of thermal variations across an object. Infrared radiation

covers a portion of the electromagnetic spectrum from approximately 0.9 to 14 micrometers. It is emitted by all objects at temperatures above absolute zero and its magnitude increases with temperature.

The main IR camera components are the lens that focuses IR onto a detector, a cooler for the detector, and the electronics and software for processing and displaying the images. The IR camera detector is a focal plane array (FPA) of micrometer size pixels made of various wavelengths. FPA resolution can range from about 160×120 pixels up to 1024×1024 pixels. The IR camera has built-in software that allows the user to focus on specific areas of the FPA and calculate the temperature. Other systems use a computer or data acquisition system with specialized software that provides temperature analysis. Both methods can supply temperature data of accuracy better than $\pm 1^{o}C$ [130].

FPA detector technologies are divided into two categories: thermal detectors and quantum detectors. The majority of IR cameras have a microbolometer type detector,. Microbolometer FPAs can be created from metal or semiconductor materials. Microbolometers respond to incident radiant energy in a way that causes a change of state in the bulk material (i.e., the bolometer effect). Generally, microbolometers do not require cooling, which allows compact camera designs that are relatively lower cost. Other characteristics of microbolometers are:

- Relatively low detectivity;
- Broad response curve;
- Slow response time (time constant of about 12 ms).

Typically, IR cameras are designed and calibrated for a specific range of the IR spectrum. Therefore, the optics and the detector materials must be selected for the desired range. Since IR has the same properties as visible light regarding reflection, refraction, and transmission, the optics for thermal cameras are designed in a fashion similar to those of a visual wavelength camera. However, the types of glass used in optics for visible light cameras cannot be used for optics in an infrared camera, as they do not transmit IR wavelength well enough. IR camera lenses typically use silicon (Si) and germanium (Ge) materials. Normally Ge is used in long wavelength cameras and Si is used for medium wavelength camera systems. Si and Ge have good mechanical properties. They are non-hygroscopic, and they can be formed into lenses with modern turning methods. As in visible light cameras, IR camera lenses have antireflective coatings. With a proper design, IR camera lenses can transmit close to 100% of incident radiation.

7.1.1.2 Quantum detectors

Electrons exist at different energy levels. Some electrons have sufficient thermal energy to be in the conduction band. This means that the electrons are free to move and the material can conduct an electrical current. However, most electrons are in the valence band, where they cannot move freely and do not conduct any current.

When the material is cooled to a low enough temperature, none of the electrons are in the conduction band due to the low thermal energy. Hence the material cannot carry any current. When these materials are exposed to incident photons with sufficient energy, this energy can stimulate an electron in the valence band, causing it to move up into the conduction band. Thus the material can carry a photocurrent, which is proportional to the

intensity of the incident radiation. The lowest energy of the incident photons that will allow an electron to jump from the valence band into the conduction band is related to a certain wavelength. Since photon energy is inversely proportional to its wavelength, the energies are higher in the SW/MW band than in the LW band. Therefore, the operating temperatures for LW detectors are lower than for SW/MW detectors. For an InSb MW detector, the necessary temperature must be less than 173K, although it may be operated at a much lower temperature. An HgCdTe LW detector must be cooled to 77 K or lower. A QWIP detector typically needs to operate at about 70K or lower [130].

Quantum detectors operate on the basis of an intrinsic photoelectric effect. These materials respond to IR by absorbing photons that elevate the material's electrons to a higher energy state, causing a change in conductivity, voltage, or current. By cooling these detectors to cryogenic temperatures, they can be very sensitive to the IR focused on them. They react very quickly to changes in IR levels, i.e., temperatures, having a constant response time on the order of 1 μs. Therefore, a camera with this type of detector is very useful in recording transient thermal events. Table (7-1) lists some of the most commonly used detectors in IR cameras.

Table 7-1 Detector types and materials commonly used in IR cameras

Detector type/ material	Operation	Operating temperature, K
Microbolometer	Broad band detector	Uncooled (300)
HgCdTe	SW photon detector	200
HgCdTe	LW photon detector	77
InSb	MW photon detector	77
PtSi	MW photon detector	77
QWIP	LW photon detector	70

The first detectors used in infrared radiometric instruments were cooled with liquid nitrogen. The detector was attached by a Dewar flask that held the liquid nitrogen, thus keeping the detector at a very stable and low temperature (77 K). Later, other cooling methods were developed. The first solid-state cooling method was developed by AGEMA in 1986, when it introduced a Peltier effect cooler for a commercial IR camera. In a Peltier cooler (see Figure 7-2), DC current is supplied through a thermoelectric material, removing heat from one junction and creating a cold side and a hot side. The hot side is connected to a heat sink, whereas the cold side cools the component attached to it.

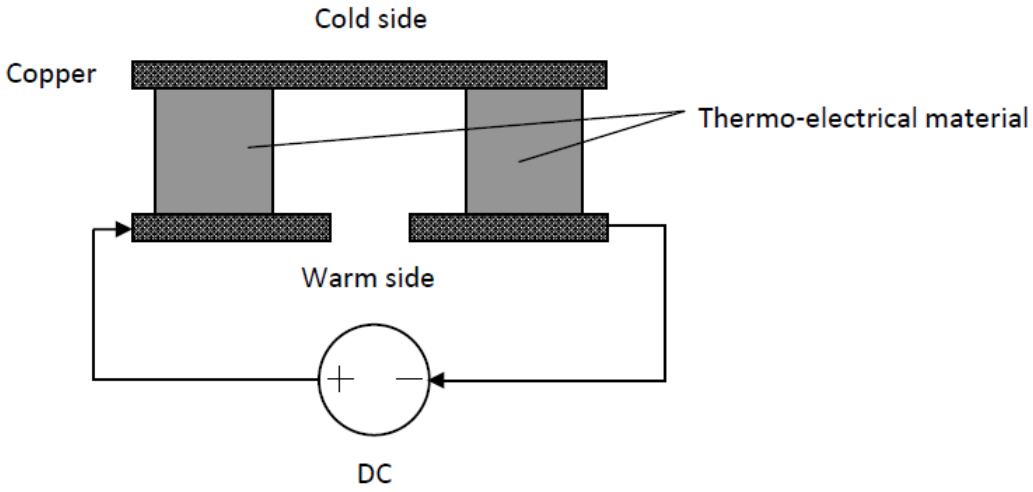

Figure 7-2 Peltier cooler

When the highest possible sensitivity is needed, the Stirling cooler can be used. Only in the last 15 to 20 years, manufacturers were able to extend the life of Stirling coolers to 8,000 hours or more, which is sufficient for use in thermal cameras. The efficiency of this type of cooler is relatively low, but sufficient for cooling an IR camera detector.

Photon detectors offer a number of advantages:

- High thermal sensitivity;
- High uniformity of the detectors, i.e., very low fixed pattern noise;
- Degree of selectability in their spectral sensitivity;
- High yield in the production process;
- Resistance to high temperatures and high radiation;
- Very good image quality.

7.1.1.3 Temperature measurement

The IR camera receives radiation from the target object, plus radiation from its surroundings that has been reflected onto the object's surface. Both of these radiation components become attenuated when they pass through the atmosphere. The atmosphere itself also radiates some energy.

The total radiation power received by the camera can be written as:

$$W = W_1 + W_2 + W_3 \tag{7.1}$$

where W_1 is the energy received due to emission from the object, given by

$$W_1 = \tau \, \epsilon \, E_b(T_{obj}) \tag{7.2}$$

where ε is the emissivity of the object, τ is the transmittance of the atmosphere, and $E_b(T_{obj})$ is the blackbody emission at the object temperature. Also, W_2 is the energy received due to the reflected emission from surrounding sources, given by:

$$W_2 = \tau \, (1 - \epsilon) \, E_b(T_{sur}) \tag{7.3}$$

where (1-ε) is the reflectivity of the object.W_3 is the emission from the atmosphere, given by:

$$W_3 = (1 - \tau)\, E_b(T_{atm}) \quad (7.4)$$

where (1-τ) is the emissivity of the atmosphere. To calculate the correct target object, the IR camera software requires inputs for the emissivity of the object, atmospheric attenuation and temperature, and the surrounding temperature. These parameters may be measured, assumed, or found from tables.

A Flir SC5600 camera (Figure 7-3) with Altair software was used for thermography of the molten copper(I) chloride droplets. The technical specifications of the IR camera are shown in Table 7-2.

Figure 7-3 Flir SC5600 Infrared camera

Table 7-2 Technical specifications of Flir Sc5600

Sensor type	InSb
Waveband	3-5 µm
Pixel resolution	640×512
Pitch	15 µm
Cooler	Close cycle Stirling cooler
Maximum frame rate (full frame)	100 Hz
Integration time	200 ns to 20 ms
Temperature measurement range	5 -1500^{o}C
Temperature measurement accuracy	±1^{o}C or ±1%

7.1.2 X-ray diffraction system

X-ray diffraction (XRD) is a versatile, non-destructive technique that reveals detailed information about the chemical composition of materials. When X-rays are incident on an atom, they make the electron cloud move. The movement of these charges re-radiates the waves with the same frequency. This phenomenon is known as Rayleigh scattering. These re-emitted wave fields interfere with each other, either constructively or destructively, producing a diffraction pattern on a detector. The resulting wave interference pattern is the basis of diffraction analysis which is called Bragg diffraction. Bragg diffraction was first proposed by W. L. Bragg and W. H. Bragg in 1913 in response to their discovery that crystalline solids produced surprising patterns of reflected X-rays. They found that these crystals, at certain specific wavelengths and incident angles, produced intense peaks of reflected radiation, known as Bragg peaks. Bragg explained this result by modeling the crystal as a set of discrete parallel planes separated by a constant parameter, d. It was proposed that the incident X-ray radiation would produce a Bragg peak if their reflections off the various planes interfered constructively. The interference is constructive when the phase shift is a multiple of 2π. This condition can be expressed by Bragg's law [129]:

$$n\lambda = 2dsin\theta \tag{7.5}$$

where n is an integer, λ is the wavelength of the incident wave, d is the spacing between the planes in the atomic lattice, and θ is the angle between the incident ray and the scattering planes.

Each crystalline substance has a unique X-ray diffraction pattern. The number of observed peaks is related to the symmetry of the unit cell (higher symmetry generally

means fewer peaks). The d-spacings of the observed peaks are related to the repeating distances between planes of atoms in the structure. The intensities of the peaks are related to the types of atoms in the repeating planes. The scattering intensities for X-rays are directly related to the number of electrons in the atom. Hence, light atoms scatter X-rays weakly, while heavy atoms scatter X-rays more effectively. Therefore, three features of a diffraction pattern (i.e., the number of peaks, the positions of the peaks, and the intensities of the peaks) define a unique, fingerprint X-ray powder pattern for every crystalline material [131].

A typical diffractometer consists of a source of radiation, a monochromator to choose the wavelength, slits to adjust the shape of the beam, a sample, a detector, and a goniometer to adjust the sample and detector positions. In this study, a Philips XRD system, at the University of Toronto - Department of Earth Sciences, was used. The basic components of the system are a PW 1830 HT generator, a PW 1050 goniometer, PW 3710 control electronics, and X-Pert system software. During data collection, the sample remains in a fixed position and the X-ray source and detector are programmed to scan over a range of 2θ values. Here 2θ is the sum of the angle between the X-ray source and the sample and that between the sample and the detector. Routinely, a 2θ range of 2˚ to 60˚ is sufficient to cover the most useful part of the powder pattern. Choosing an appropriate scanning speed (measured in ˚ 2θ/min) depends on balancing the desire to collect a powder pattern quickly with obtaining a reasonable signal-to-noise ratio for the diffraction peaks. One can begin with a scanning speed of 2˚/min and recollect the diffraction pattern at a slower speed if the background is too noisy.

7.2 Procedures

In the heat transfer experiments, a heating mantle is used to produce molten copper(I) chloride. Then, molten CuCl is poured into a small container with a nozzle at the bottom. A torch is used to heat and re-melt the solidified CuCl and produce droplets of molten CuCl. The molten droplets exiting the nozzle fall through air and eventually into a water vessel. The distance of the droplet in air is about 80 cm. The surface temperature of the droplet during the flight is measured by an infrared camera.

To investigate the possible reactions between copper(I) chloride and water or air, two sets of experiments are performed. In one set of experiments, the solidified product in water is collected and dried in air. In the other set of experiments, the solidified material is kept in a small container filled with water, in a nitrogen glove box, to avoid exposure to air. The composition of each prepared sample was then determined by an X-ray diffractometer.

7.3 Measurement uncertainties

It is well known that all measurements have errors, δ_k [130]. These errors are the differences between the measurements and actual values (see Figure 7-4). The total error is expressed in terms of two components: a fixed (bias) error, β, and a random (precision) error, ε_k, such that

$$\delta_k = \beta + \epsilon_k \tag{7.6}$$

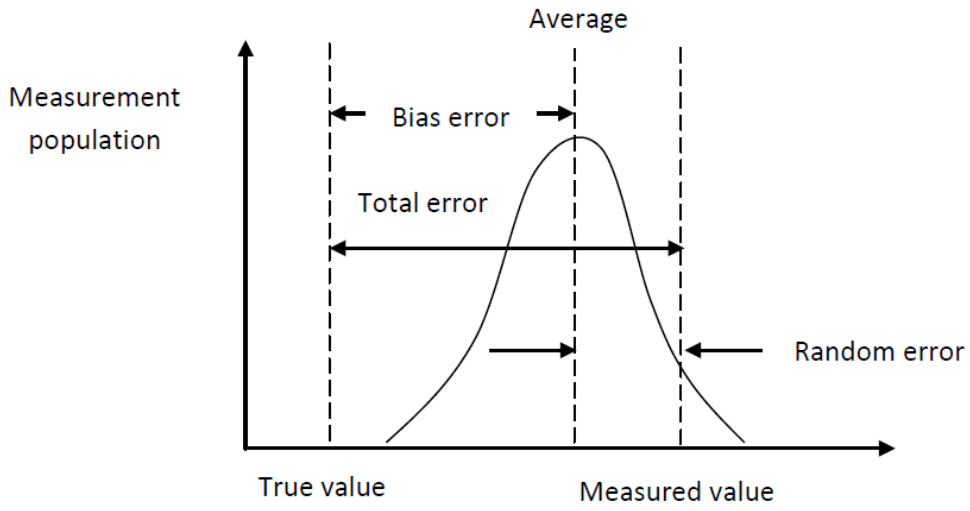

Figure 7-4 Measurement error

7.3.1 Precision index

The precision error is determined by taking N repeated measurements from the parameter population. Their characteristics are approximated by the precision index, S, which is defined by [131]:

$$S = \left[\sum_{i=1}^{N} \frac{(X_i - \bar{X})^2}{N-1}\right]^{\frac{1}{2}} \tag{7.7}$$

where $\bar{X}$ is the average value of X. The precision index of the average of a set of measurements is always less than that of an individual measurement, according to:

$$S_{\bar{X}} = \frac{S}{\sqrt{N}} \tag{7.8}$$

7.3.2 Bias error

The bias error, B, is the systematic error which is assumed to remain constant during a given test. Therefore, in repeated measurements of a given test, each measurement has the

same bias error. Estimation of the bias error is difficult since the true value is not known. Calibrations or a comparison of measurements by independent methods may help, however the estimate of bias is based on judgment generally.

7.3.3 Combining errors

Errors may be divided into three categories: calibration errors, data acquisition errors, and data reduction errors [132]. To obtain the precision of a given parameter, the root sum square (RSS) method is used to combine the precision indices from the K sources of error.

$$S = [S_1^2 + S_2^2 + \cdots + S_K^2]^{\frac{1}{2}} \tag{7.9}$$

Similarly, the bias of a given parameter is given by

$$B = [B_1^2 + B_2^2 + \cdots + B_K^2]^{\frac{1}{2}} \tag{7.10}$$

7.3.4 Uncertainty of a parameter

A single variable, U, can be used to express the limit of error for a given parameter. The interval ($\overline{X}$-U, $\overline{X}$+U) represents a band within which the true value of the parameter is expected to lie, for a specific coverage.

While no exact confidence level is associated with the uncertainty, coverage analogous to the 95% and 99% confidence levels may be given for the two recommended uncertainty models. Therefore,

$$U = B + tS_{\bar{X}} \tag{7.11}$$

provides 99% coverage, and

$$U = [B^2 + (tS_{\bar{X}})^2]^{\frac{1}{2}} \tag{7.12}$$

provides 95% coverage. Here $t$is the Student's t multiplier and a function of the degrees of freedom, used in calculating $S_{\bar{X}}$. For large samples, i.e., N>30, t is set equal to 2. Otherwise the Welch-Satterthwaite formula can be used to evaluate ν.

7.3.5 Uncertainty of a result

Errors in measurements of various parameters, P, are propagated into a derived result, R, through the functional relationship between the result and its independent parameters. The relationship provides the sensitivity factor, θ_i, which indicates the error propagated to the result because of unit error in the parameter. Therefore,

$$\theta_i = \frac{\partial R}{\partial P_i} \tag{7.13}$$

where i is the index of the parameter.

The uncertainty of a result can be computed based on the precision and bias errors. The precision index of a result is given by [133]:

$$S_R = \left[\sum_{i=1}^{I} \left(\theta_i S_{P_i}\right)^2\right]^{\frac{1}{2}} \tag{7.14}$$

The bias limit of the result is given by:

$$B_R = \left[\sum_{i=1}^{I} \left(\theta_i B_{P_i}\right)^2\right]^{\frac{1}{2}} \tag{7.15}$$

The uncertainty of a result is again given by:

$$U_R = B_R + tS_R \tag{7.16}$$

for 99% coverage, and

$$U_R = [B_R^2 + (tS_R)^2]^{\frac{1}{2}} \tag{7.17}$$

for 95% coverage. Again, t is the Student's t multiplier and a function of the degrees of freedom used in calculating S_R. For large samples of all parameters, t is set to 2.

Chapter 8 Results of Analytical and Experimental Analysis of Heat Recovery from Molten Cu-Cl

8.1 Indirect contact heat transfer

8.1.1 Validation of results

In this section, the computed results for indirect contact heat transfer from a solidifying flow in a pipe are compared with past results reported by Seeniraj and Hari [102] for selected values of parameters for water. The coolant temperature is assumed to be constant. Figures 8-1 and 8-2 show the axial variation of the bulk mean temperature and axial growth of solid layer for laminar flow, respectively. In these figures, Bi=10, Ste_s/Ste_l=0.5, and τ=0.5.

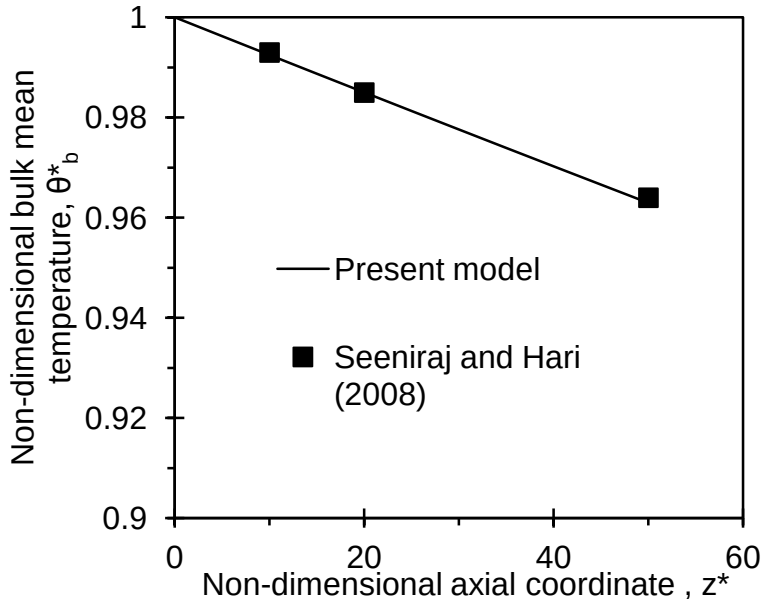

Figure 8-1 Axial variation of bulk mean temperature for laminar flow

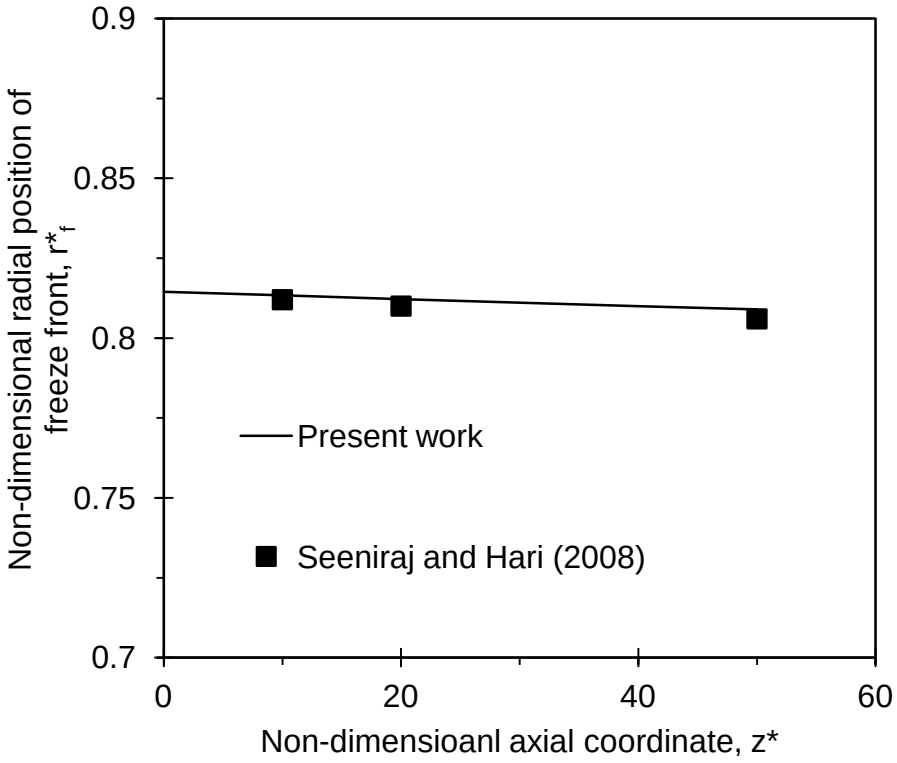

Figure 8-2 Axial growth of solid layer for laminar flow

Figures 8-3 and 8-4 show comparisons between the present work and the results obtained by Seeniraj and Hari [102] for turbulent flow. The results show good agreement with past data presented by other authors. Comparing the laminar and turbulent flow cases shows that the solid layer grows much faster in turbulent flow due to a larger convection heat transfer coefficient. This also affects the liquid bulk mean temperature. The variation of the bulk temperature along the tube is more significant in the turbulent flow.

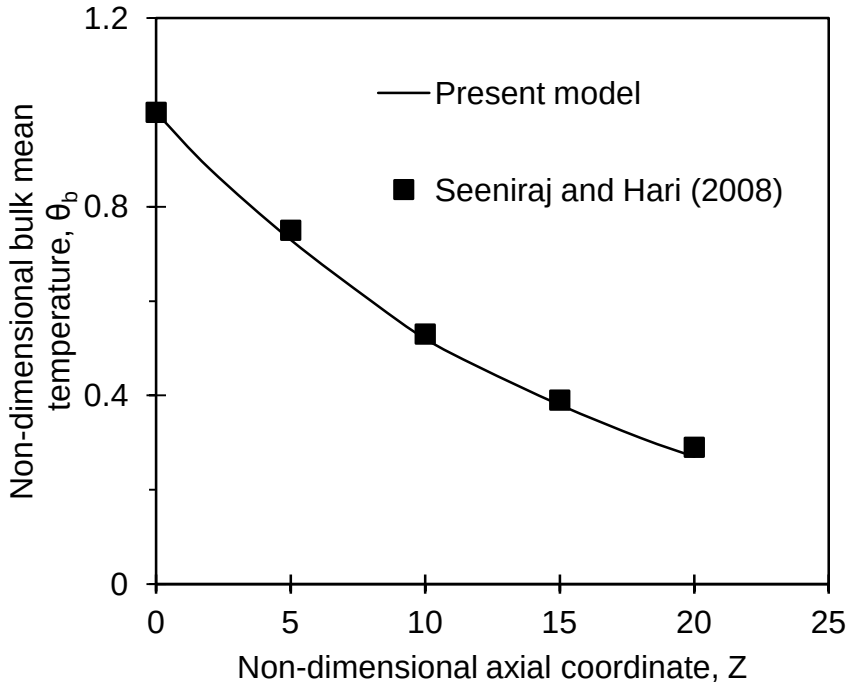

Figure 8-3 Fluid bulk temperature variation along the tube for turbulent flow

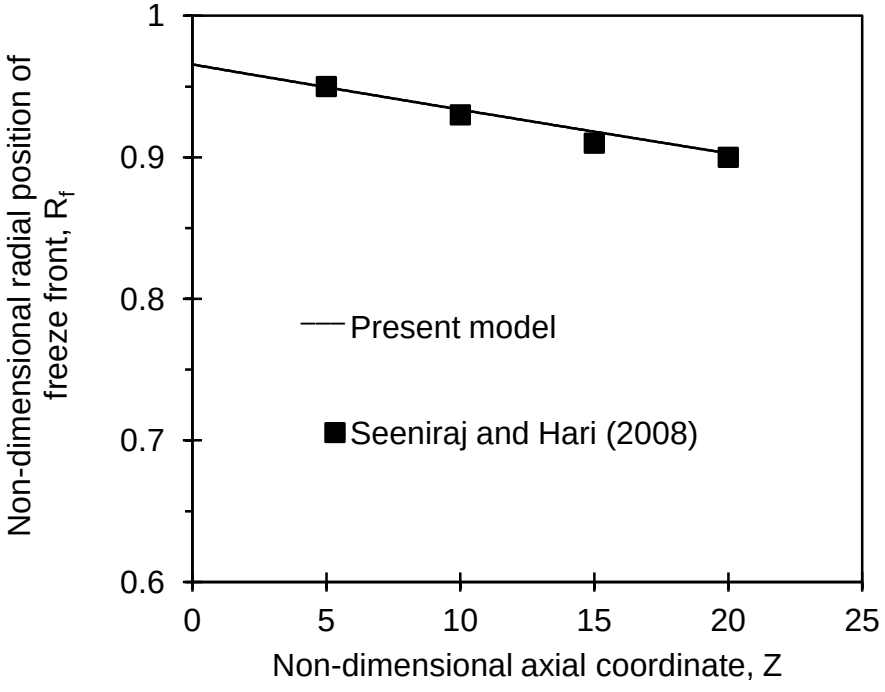

Figure 8-4 Axial growth of solid layer for turbulent flow

8.1.2 Heat recovery from molten CuCl

In this section, a counter-current double-pipe heat exchanger, for recovering heat from molten CuCl during its solidification, is analyzed. The diameter of the inner tube is 20 cm and the outer tube diameter is 25 cm. The mass flow rate of molten CuCl is 4.17 g/s, based on a hydrogen production rate of 3 kg/s. Air, with an inlet temperature of 25^{o}C, is considered as a coolant. CuCl properties at the melting point (430^{o}C) are used for both solid and liquid phases [50].

Figure 8-5 shows the variation of the coolant temperature along the tube. The mass flow rate of air is 3 g/s and its bulk velocity is 0.14 m/s. The air temperature is increased to 190^{o}C in a heat exchanger with a length of 15 cm.

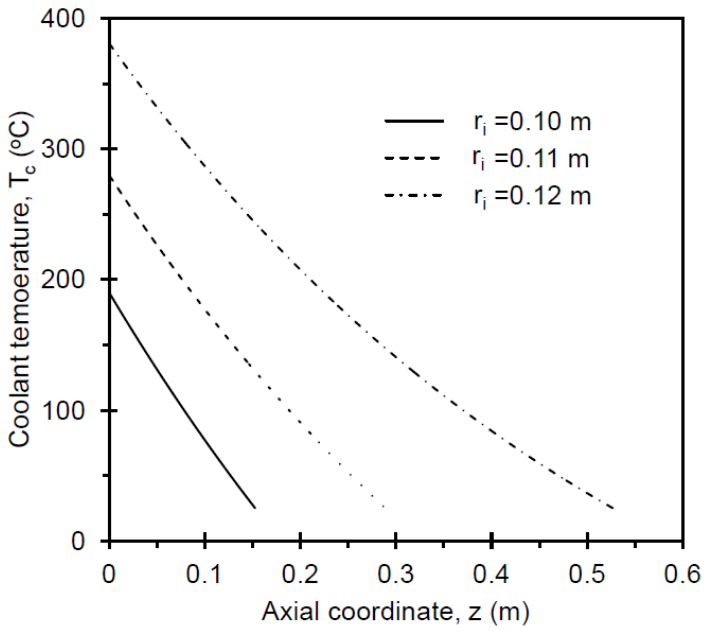

Figure 8-5 Axial variation of the coolant temperature and effect of inner tube dimension

The effect of the inner tube radius on the coolant temperature and the length of the heat exchanger is also shown in this figure. The outer tube radius is fixed. Since the

flow in the shell is laminar, the Nusselt number is almost constant. Therefore, increasing the inner tube radius, and hence decreasing the hydraulic diameter, will cause an increase in the convection heat transfer coefficient in the shell. Therefore, the coolant temperature will increase by increasing the inner tube radius. The outlet temperature of the coolant and the length of the heat exchanger are increased significantly by increasing the inner tube radius. As a result, the heat transfer from the molten salt will be increased. Increasing the inner tube diameter will also affect the growth of solid layer. This is illustrated in Figure 8-6. For the tube with r_i =0.1 m, the length of the heat exchanger is not sufficient to solidify the entire molten salt flow in the tube. For a hydrogen production rate of 3 kg/day, a heat exchanger with a diameter of 25 cm and height of 53 cm is required. By increasing the hydrogen production rate, the number of heat exchangers required is increased proportionally.

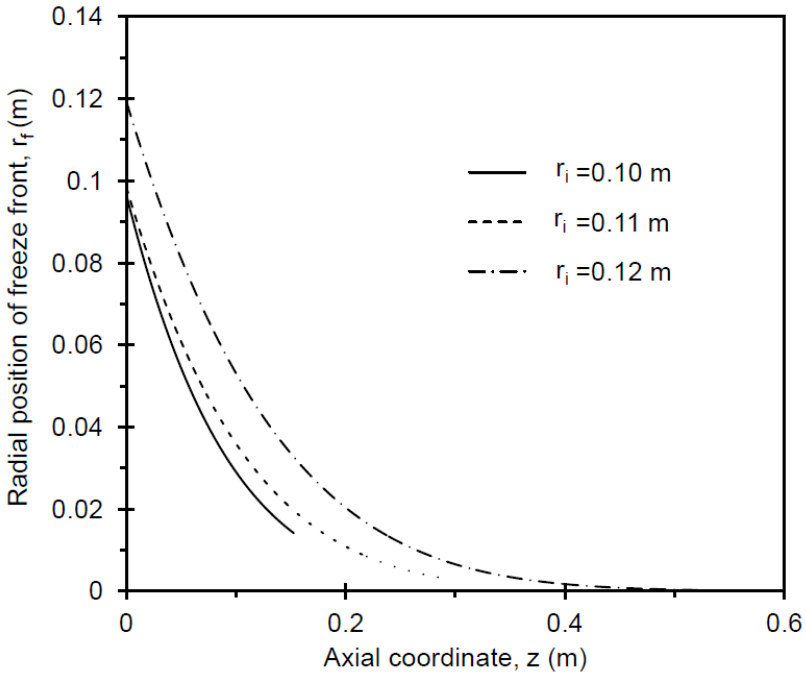

Figure 8-6 Axial growth of solid layer for different inner tube radii

For a heat exchanger with an inner tube diameter of 24 cm, the effect of mass flow rate is investigated. Figure 8-7 demonstrates the variation of the inner wall temperature along the tube. Increasing the air flow rate causes an increase in the heat exchanger length. Since the wall temperature at the top and bottom of the tube is almost the same for both air flow rates, the variation of wall temperature along the tube is slower for the longer tube.

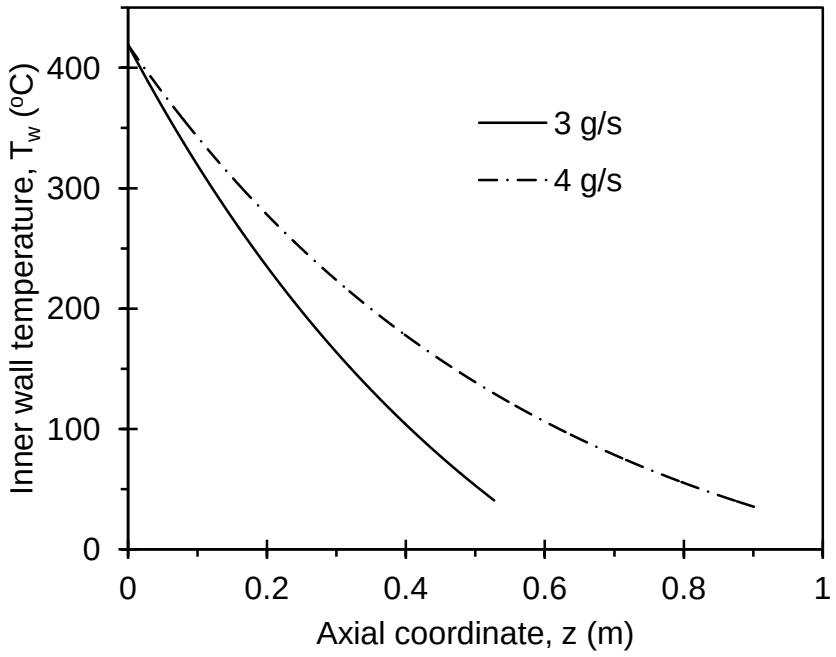

Figure 8-7 Wall temperature variation along the tube for two different air flow rates

Although the coolant and wall temperatures increase when increasing the air flow rate, the temperature difference, (T_w-T_c), and hence the heat flux, is almost constant for both air flow rates. However, the total heat transfer is higher for the heat exchanger with a larger air flow rate, due to its longer length. The heat flux along the tube is shown in Figure 8-8.

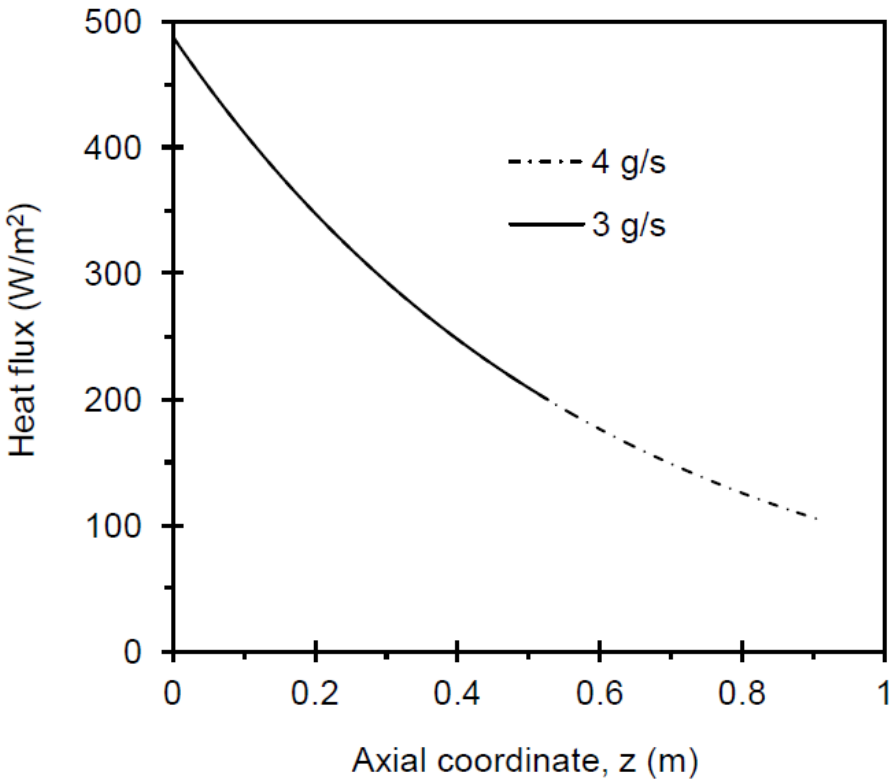

Figure 8-8 Heat flux along the tube for two different air flow rates

8.2 Direct contact heat transfer

8.2.1 Dynamics of a droplet

Figure 8-9 illustrates the variation of the drag coefficient versus Reynolds number using different correlations from Chapter 6. A comparison between these correlations shows relatively low deviations. The correlation suggested by Clift and Gauvin [125] is used in the following calculations.

Figure 8-10 shows the effect of drag coefficient on the acceleration of the falling droplet. At the initial time, the acceleration is equal to gravitational acceleration. The drag force increases with flight time, hence the acceleration of the droplet decreases. If the drag force is neglected, the acceleration of the droplet remains constant, equal to the

gravitational acceleration. Since the drag coefficient is a function of velocity, it varies during the trajectory. However, Figure 8-10 shows that a constant drag coefficient results in an error of less than 0.5% which is small. Therefore, the drag coefficient is assumed constant in the following calculations.

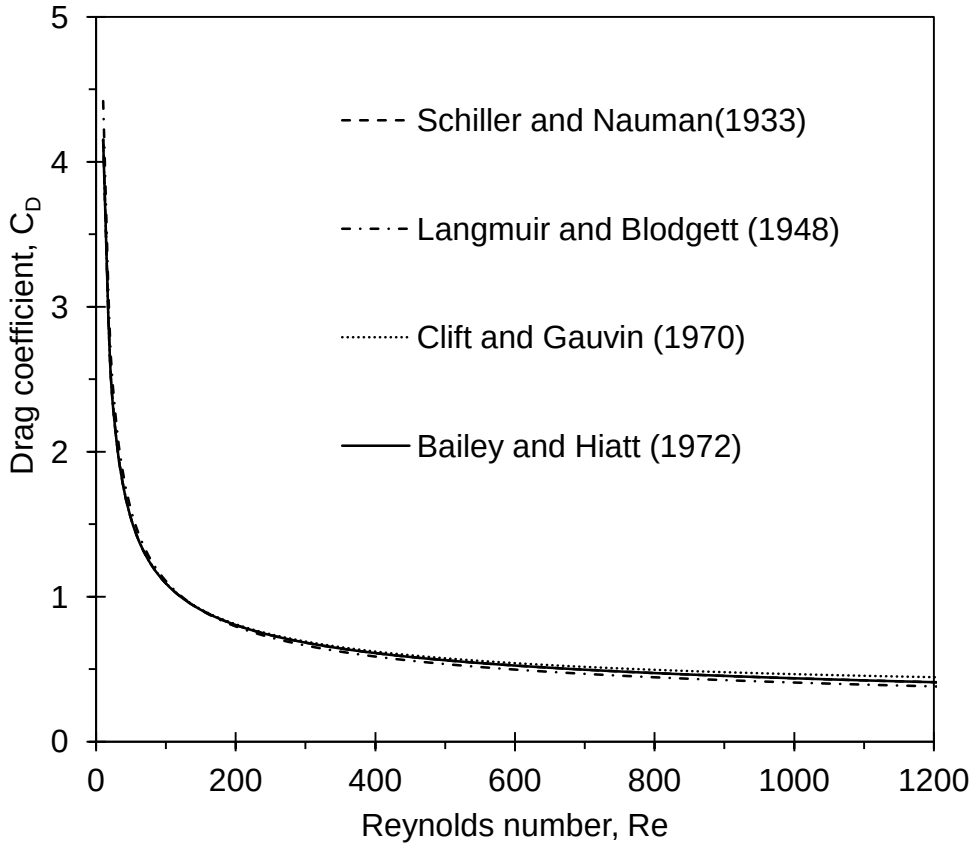

Figure 8-9 Drag coefficient as a function of Reynolds number

Figures 8-11 to 8-13 illustrate the effect of buoyancy and drag forces on the velocity and flight distance of the droplet, respectively. It is shown that the effect of buoyancy force on the velocity and the flight distance is minor. Therefore, the buoyancy force will be neglected.

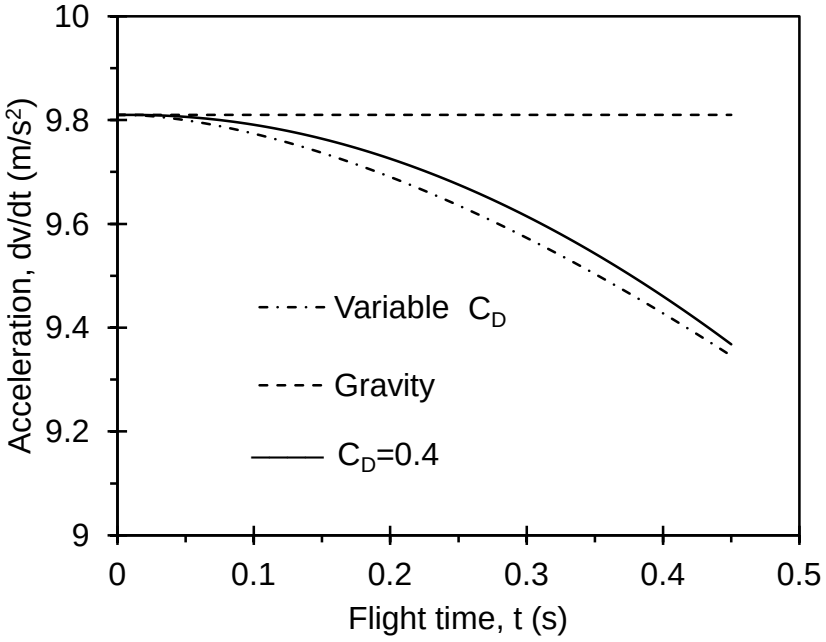

Figure 8-10 Droplet acceleration as a function of flight time

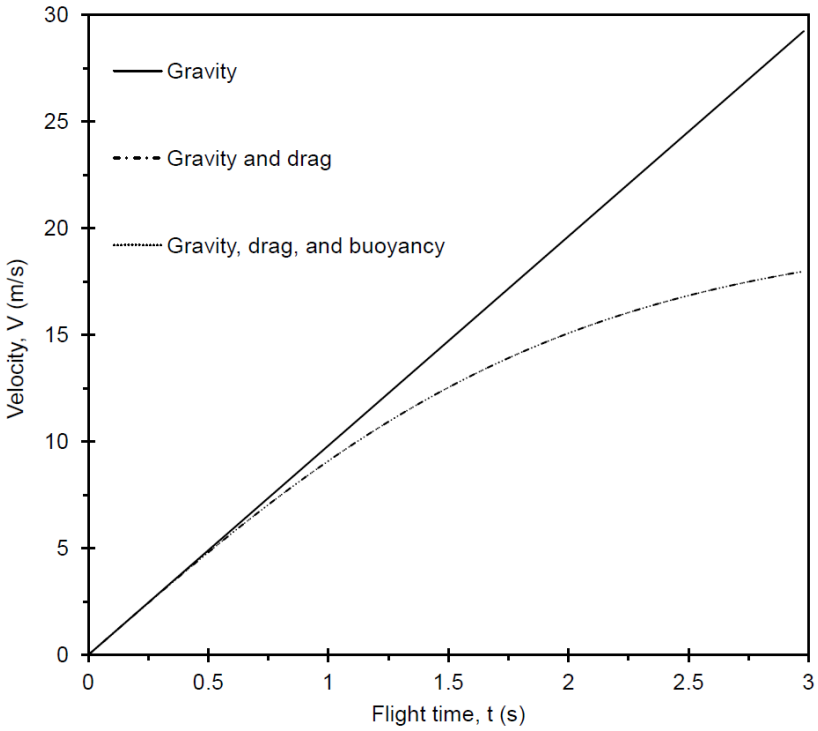

Figure 8-11 Velocity of the falling droplet as a function of flight time for different assumptions

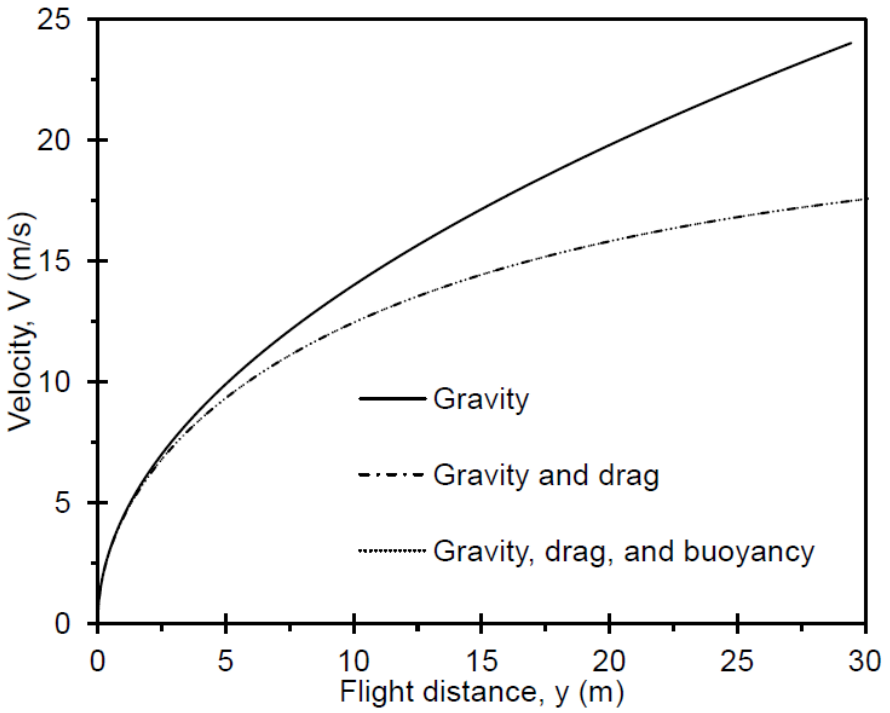

Figure 8-12 Velocity of the falling droplet as a function of flight distance for different assumptions

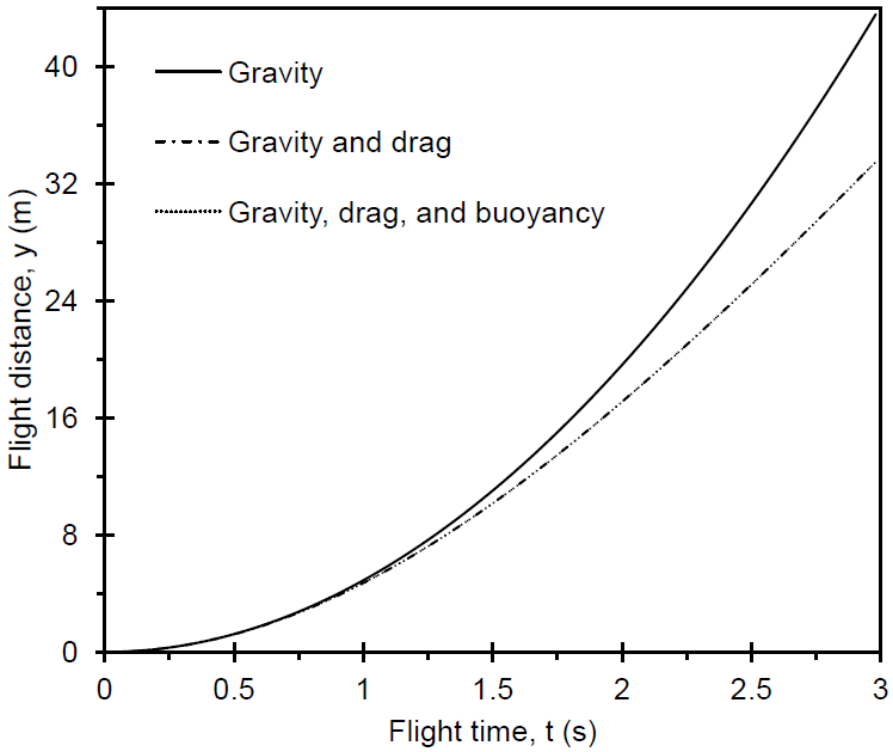

Figure 8-13 Flight distance of a droplet as a function of flight time for different assumptions

Figure 8-14 shows the Reynolds number as a function of flight distance. The initial velocity of the droplet is zero. The droplet accelerates as it moves downward. Therefore, the velocity of the droplet, hence the Reynolds number, increases with the falling distance.

8.2.2 Mass transfer from a droplet

Figure 8-15 shows the diffusivity of CuCl vapor in air as a function of temperature. The diffusivity increases slightly with temperature. Its variation over the temperature range of interest is about 25%. In this study, the average value of 6.3×10^{-5} m^2/s is used for the vapor-air diffusivity and assumed to remain constant during the flight.

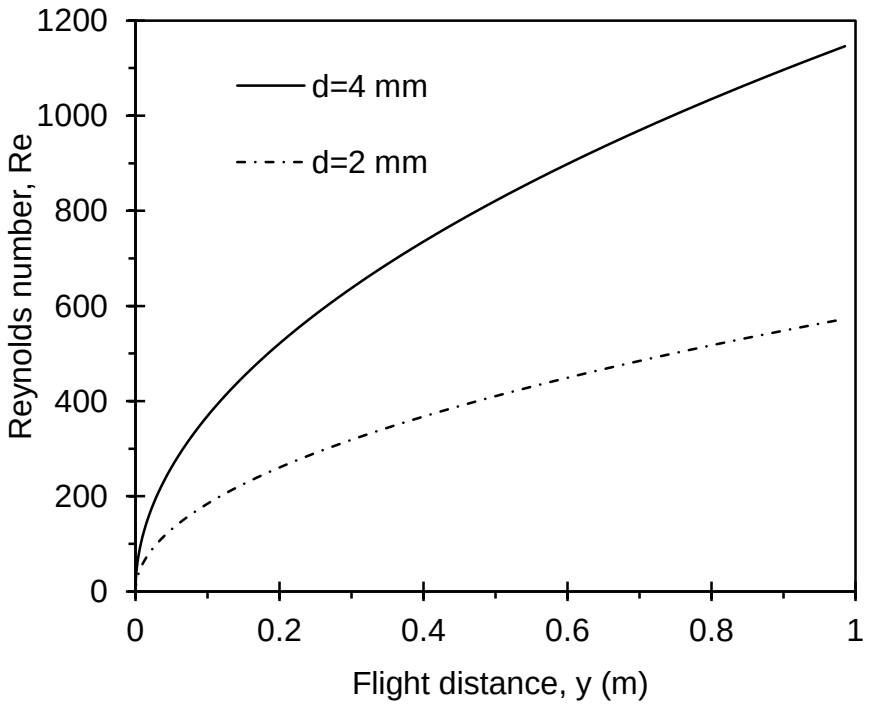

Figure 8-14 Reynolds number as a function of flight distance

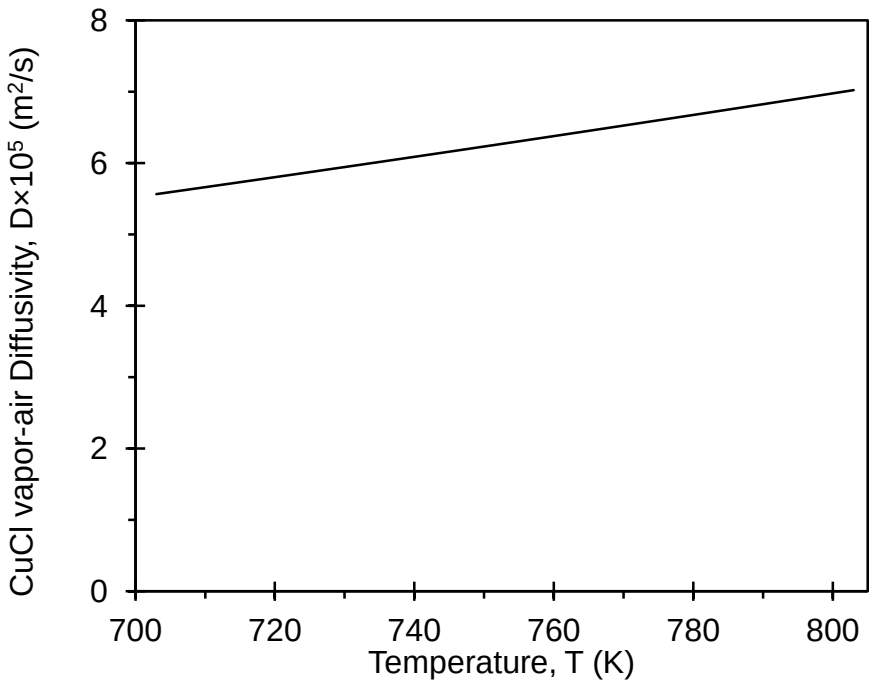

Figure 8-15 Diffusivity of CuCl vapor in air

Figure 8-16 shows the mass transfer coefficient using the Ranz-Marshall correlation and Chilton-Colburn analogy, as stated in Chapter 6. The mass transfer coefficient for a falling droplet increases with flight time until the droplet reaches the terminal velocity, and then remains constant. The Ranz-Marshall correlation predicts the mass transfer coefficient up to 8% higher than results obtained using the Chilton-Colburn analogy.

Figure 8-17 shows the mass transfer rate by convection from the droplet surface as a function of surface temperature. By decreasing the surface temperature during the flight, the mass convection rate decreases. As expected, the rate of mass transfer from the droplet surface decreases by decreasing the droplet size, due to a decrease in surface area. The effect of mass transfer on heat transfer from the droplet is shown in the following section.

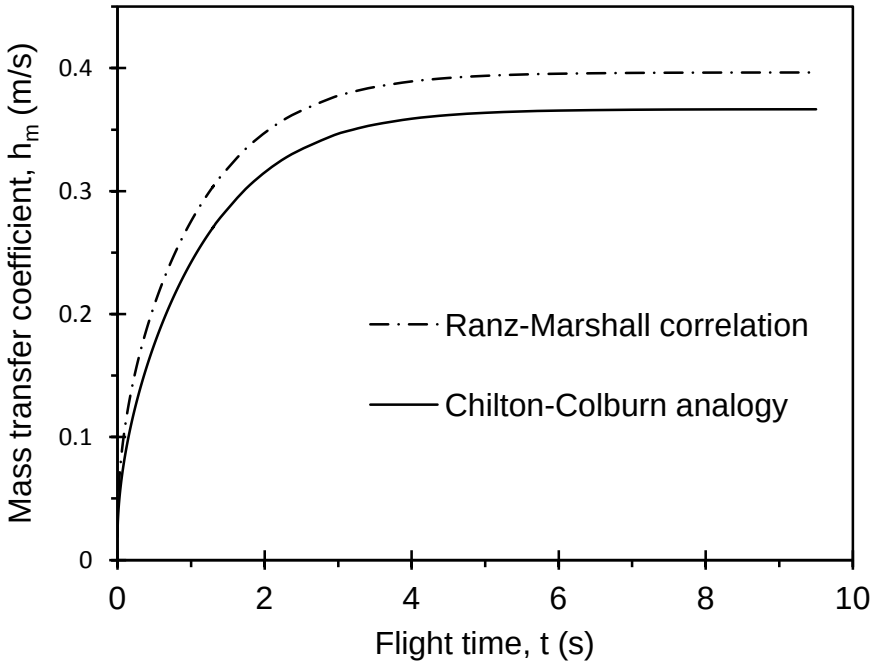

Figure 8-16 Mass transfer coefficient as a function of flight time

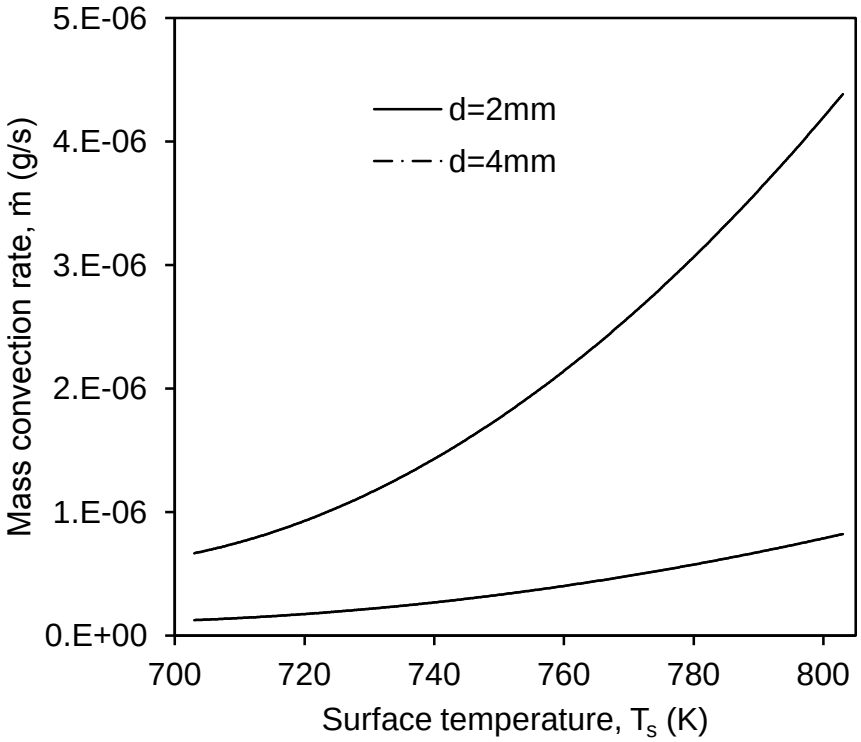

Figure 8-17 Mass convection rate as a function of droplet surface temperature

8.2.3 Heat transfer from a droplet

The Ranz-Marshall and Whitaker correlations, presented in Chapter 6, are compared in Figure 8-18. The Whitaker correlation predicts the Nusselt number up to 6% smaller than the Ranz-Marshall correlation. Doubling the Reynolds number from 2,000 to 4,000 results in an increase in the Nusselt number by about 39%. Figure 8-18 demonstrates the Nusselt number as a function of flight distance. The results obtained from the Ranz-Marshall and Whitaker correlations are compared with the correlation of Yao and Schrock [66] for freely falling droplets.

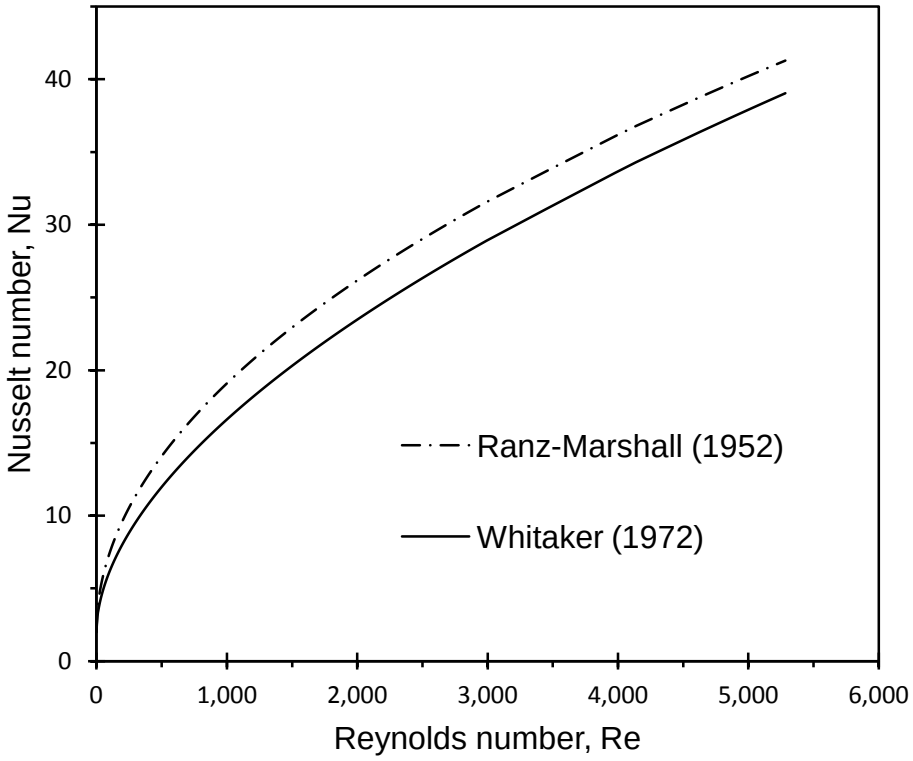

Figure 8-18 Nusselt number as a function of Reynolds number

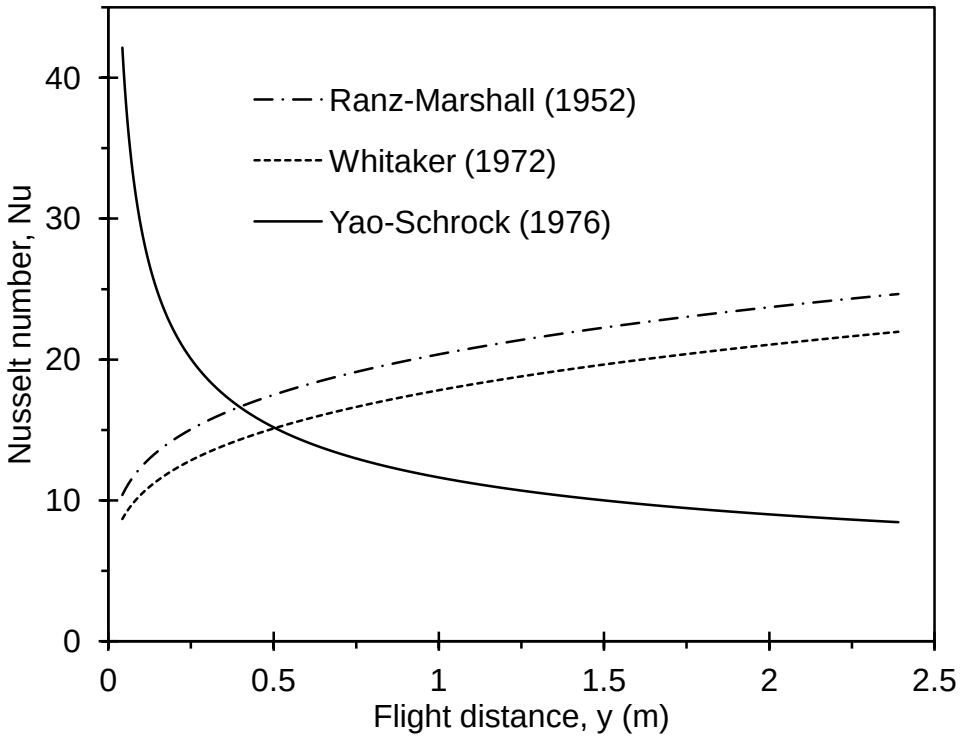

Figure 8-19 Nusselt number as a function of flight distance

The Ranz-Marshall and Whitaker equations overpredict the Nusselt number for a falling droplet for y/d>100. Another explanation is that the droplets may experience less than complete mixing for y/d>100. For y/d<100, the effect of vibration is to enhance the transport and the Nusselt number from the Yao-Schrock correlation is greater than that from the Whitaker or Ranz-Marshall equations.

Figure 8-20 illustrates the convection heat transfer coefficient for two droplet sizes. The heat transfer coefficient increases as the droplet falls until the droplet reaches a terminal velocity. The Reynolds and Nusselt numbers decrease by reducing the droplet size, however, the convection heat transfer coefficient increases by decreasing the droplet diameter.

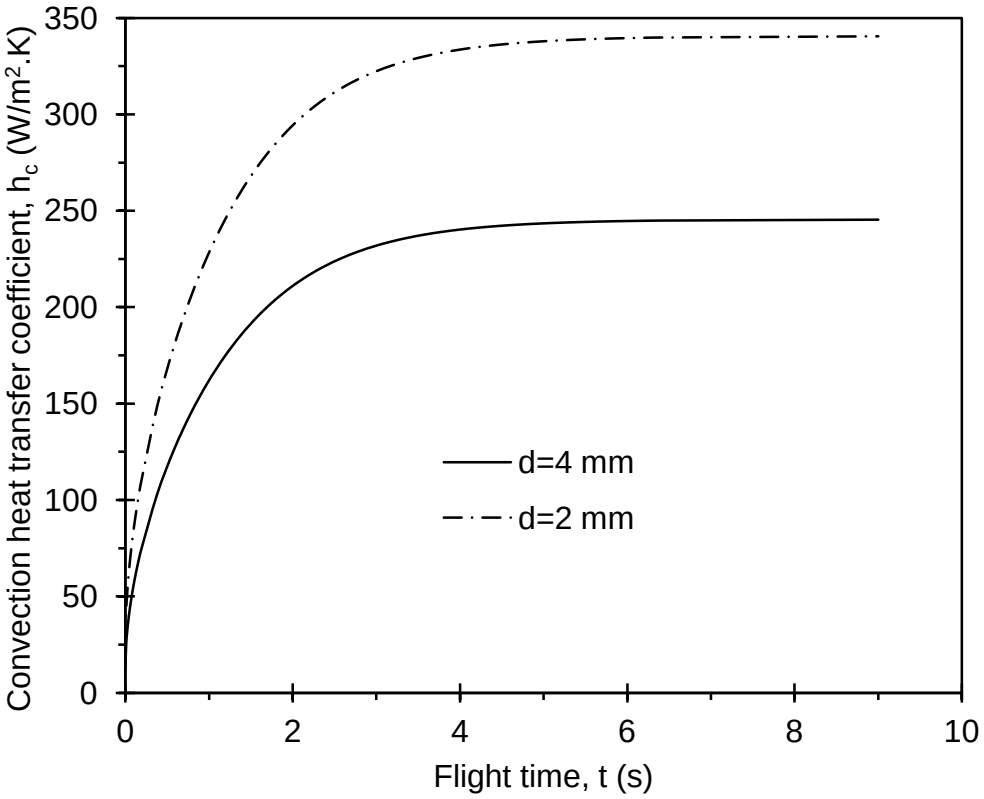

Figure 8-20 Convection heat transfer coefficient versus the flight time

Figure 8-21 shows a comparison between the convection heat transfer coefficient, h_c, and the radiation heat transfer coefficient, h_r, obtained from linearization of the radiation equation. Unlike convection, the radiation heat transfer coefficient decreases with flight time because of a decrease in the surface temperature. It is noted that h_r depends strongly on temperature, while the temperature dependence of the convection heat transfer coefficient is generally weak. In the first half second of the flight, h_r is about 30% of h_c, however, the radiation effect becomes negligible compared with convection as the droplet falls.

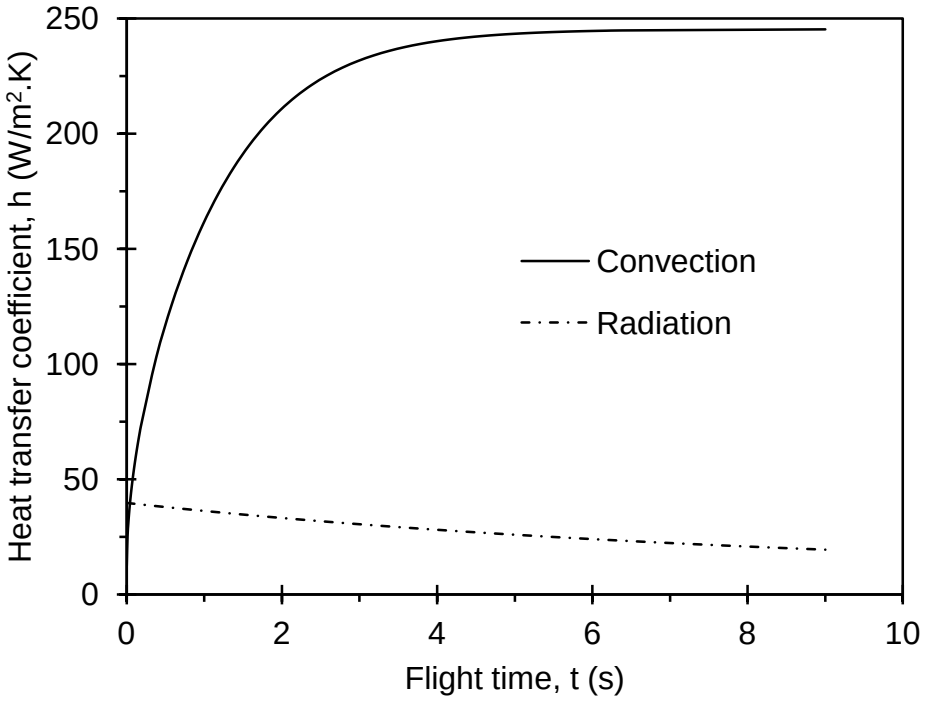

Figure 8-21 Heat transfer coefficient versus flight time

Figure 8-22 compares different mechanisms of heat transfer as a function of surface temperature of the droplet. As the droplet falls, its surface temperature decreases due to heat transfer from the surface. The rate of heat transfer due to radiation decreases by reducing the surface temperature during flight. However, the rate of heat transfer due to convection increases at first and then tends to decrease. As the droplet accelerates, the Reynolds number, and hence the convection heat transfer coefficient, increases rapidly which yields a significant rise in the convection heat transfer rate. Afterwards, the rate of convection heat transfer is dominated by the temperature difference between the droplet surface and the ambient gas, and hence decreases by reducing the temperature. It is observed that the heat transfer due to mass transfer from the droplet surface is negligible compared with radiation and convection.

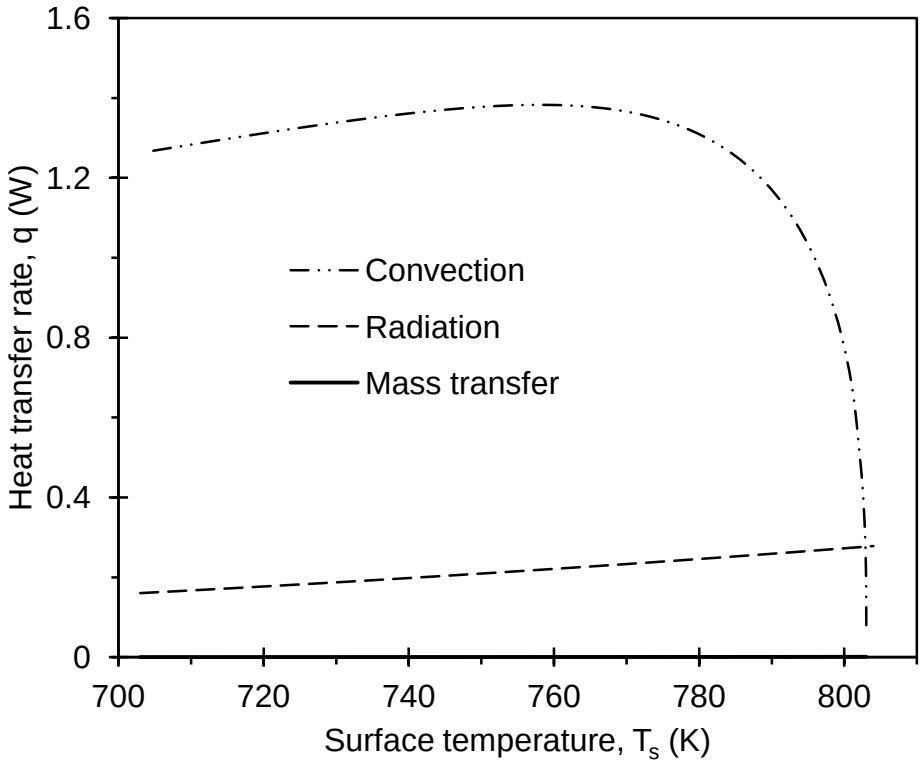

Figure 8-22 Heat transfer rate from the droplet surface versus surface temperature

8.2.4 Solidification of a droplet

The predicted temperature distribution within the droplet is shown in Figure 8-23. The results from the non-mixing model and complete-mixing model are compared in this figure. As discussed in Chapter 6, the complete-mixing model assumes that internal motion of the droplet is so strong that complete mixing is achieved. Therefore, the temperature profile in the droplet is flat. The non-mixing model assumes there is no internal motion and the energy equation is reduced to a transient heat conduction equation. The first six terms of the series solution, given in Chapter 6, are used to approximate the temperature profile in the droplet.

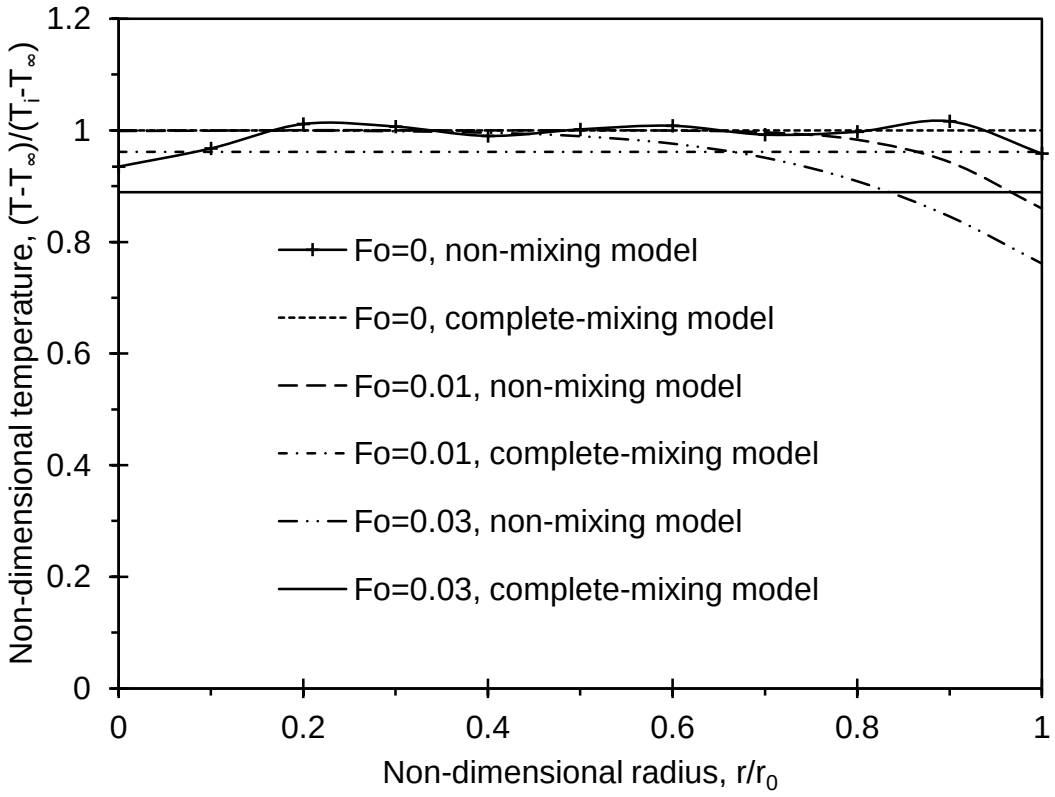

Figure 8-23 Comparison of models for different Fourier numbers

For Fo=0, the maximum error caused by the six-term approximation is less than 7%. The accuracy of the six-term approximation improves by increasing the Fourier number and fluctuations in the temperature profile are reduced. It is observed that the maximum difference between the non-mixing and complete-mixing models occurs at the droplet surface less than 16%. It is noteworthy to mention that these two models represent the bounds on the droplet temperature. The actual temperature profile of the droplet is expected to lie between these proposed models.

Figure 8-24 shows the surface temperature of the droplet versus the flight time. The experimental results represent the maximum temperature of the surface measured by the infrared camera. Unfortunately, due to budgetary constraints, only one set of

experimental data are available at this time. In future, when more measurements are taken, the measurement uncertainty can be evaluated as discussed in Chapter 7.

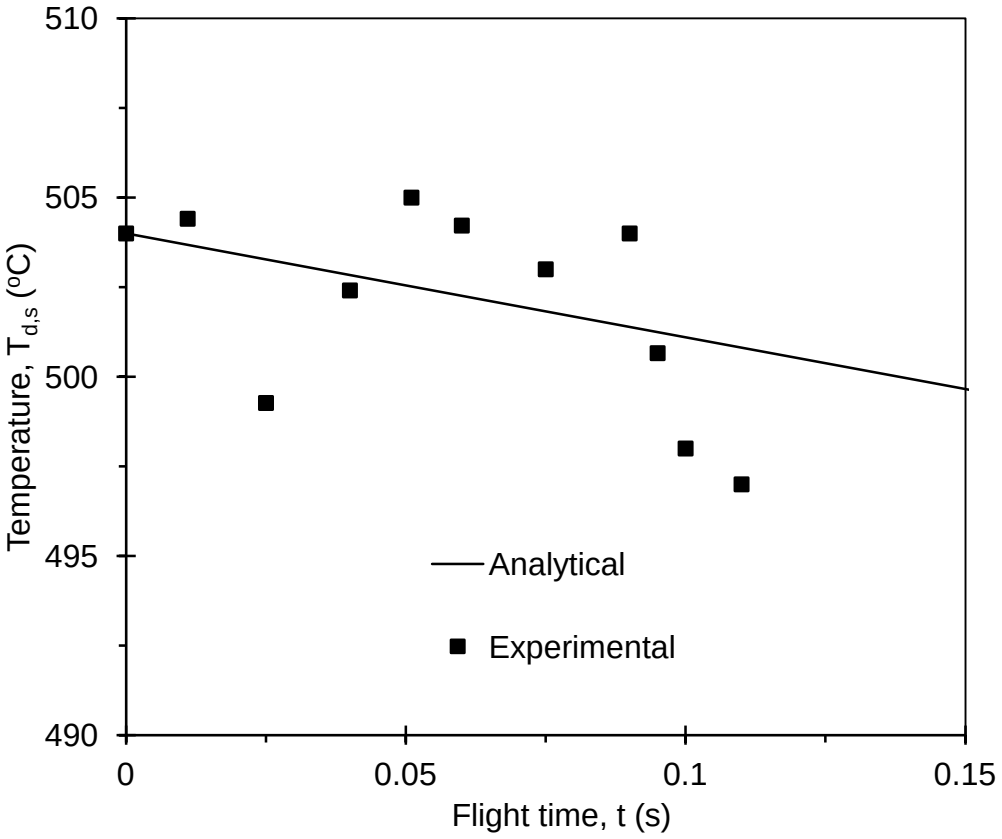

Figure 8-24 Droplet temperature versus flight time. The maximum difference between the analytical and experimental results is less than 2%.

The effect of nucleation temperature on the volume of the solid produced from nucleation is shown in Figure 8-25. As expected, by reducing the nucleation temperature, the solid volume increases steadily. The effect on nucleation temperature becomes more significant for a larger droplet.

Figure 8-26 illustrates the rate of solidification of the droplet as a function of the relative droplet-gas velocity during the flight. The solid fraction increases within the droplet as the latent heat of fusion is removed by external heat transfer. The droplet

velocity increases during the flight, hence the heat transfer rate increases, which yields an increase in the solidification rate. The heat transfer rate from the droplet surface, and hence the solidification rate within the droplet, are higher for a larger droplet due to a larger surface area.

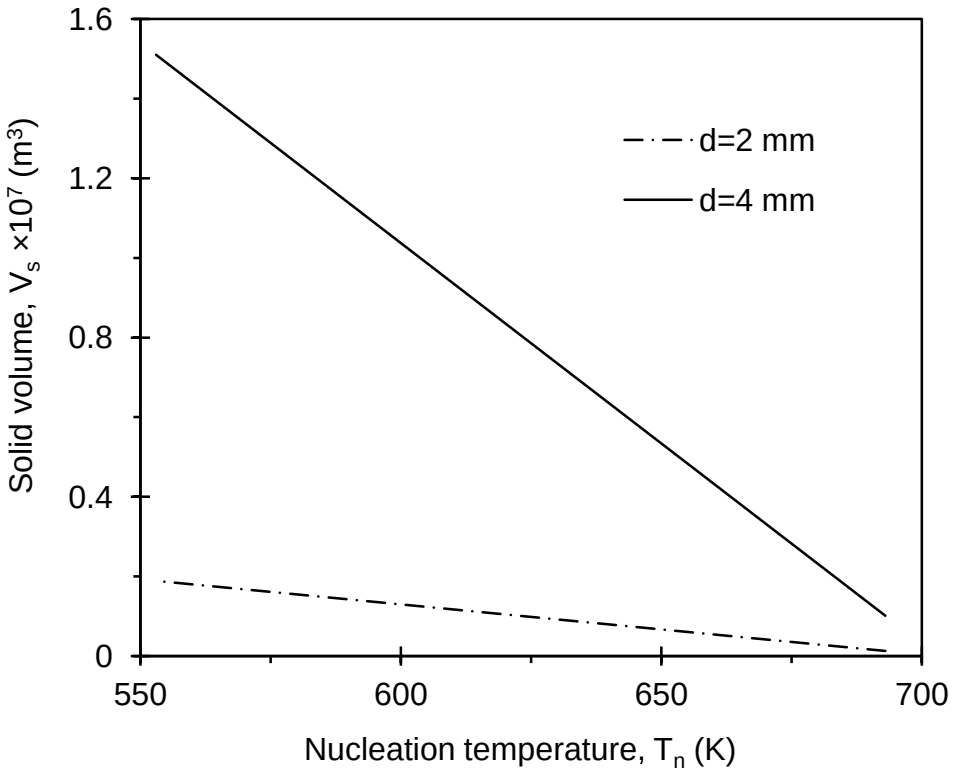

Figure 8-25 Solid volume versus nucleation temperature

The solidification model is validated by comparing the results with experimental data for a water droplet by Strub et al. [133]. Figure 8-27 shows the droplet temperature versus time. In this figure, the droplet diameter is 2.2 mm, air temperature is -7^{o}C, air velocity is 1.5 m/s, and relative humidity of air is 70%.

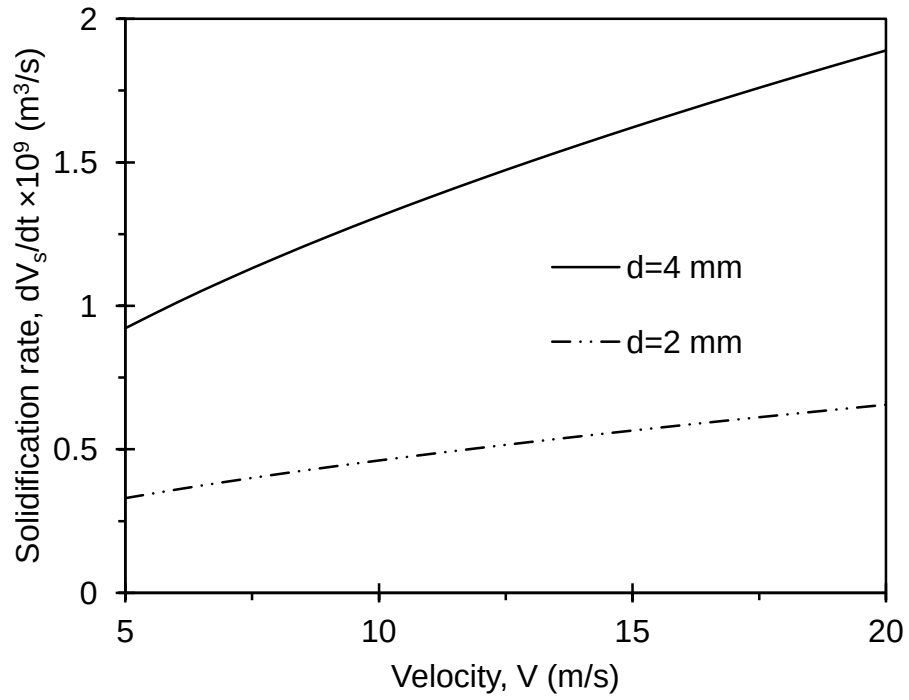

Figure 8-26 Solidification rate of a droplet during flight

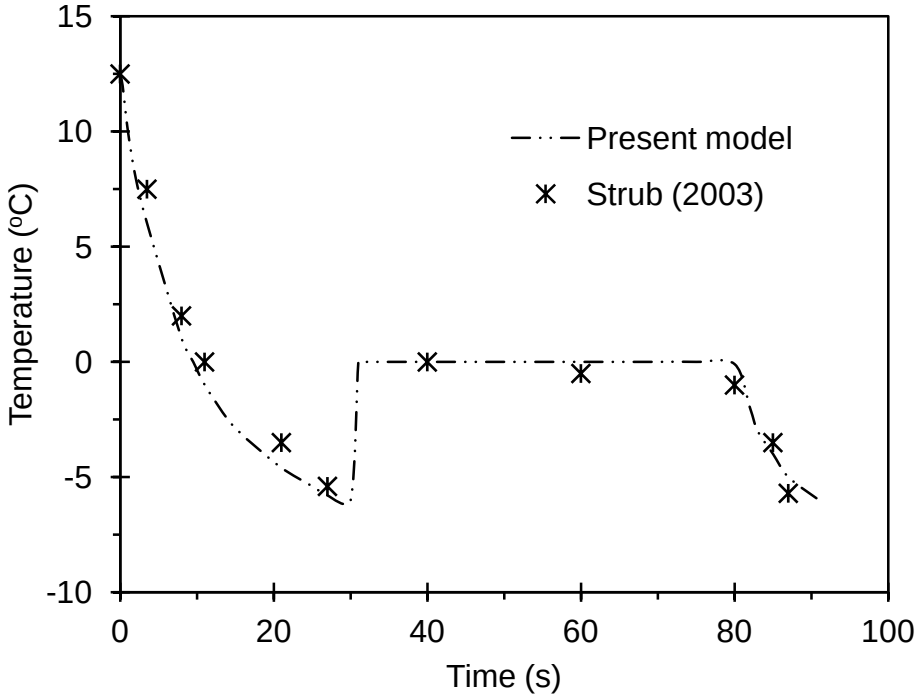

Figure 8-27 Comparison of the solidification model with experimental data for a water droplet

8.2.5 Heat Exchanger for Cu-Cl cycle

The previous results are useful to design a better heat exchanger for heat recovery from molten CuCl (see Table 8-1). Heat loss to the environment is assumed to be 30% of the heat recovered from molten CuCl. As stated in Chapter 4, the recovered heat from molten CuCl is used to produce superheated steam for the hydrolysis step of the cycle. The mass flow rates of molten CuCl and steam are calculated based on a hydrogen production rate of 1 kg/day, considering 20% excess steam.

Table 8-1 Specifications of a heat exchanger for heat recovery from molten CuCl

CuCl mass flow rate (g/s)	1.15	
CuCl inlet temperature (^{o}C)	500	
CuCl outlet temperature (^{o}C)	350	
Steam mass flow rate (g/s)	0.12	
Steam inlet temperature (^{o}C)	100	
Steam outlet temperature (^{o}C)	400	
Droplet size (m)	0.002	0.001
Heat exchanger height (m)	23	7
Heat exchanger diameter (m)	0.07	0.1
Droplet flight time (s)	2.3	1.3
Terminal velocity (m/s)	23	15

The height of the heat exchanger for a droplet size of 2 mm is about 23 m. The height of the heat exchanger is dominated by the heat transfer rate. Decreasing the droplet size may increase the heat transfer rate from the droplet, and hence decreases the required height of the heat exchanger. Increasing the relative droplet-steam velocity increases the heat transfer rate, which yields a decrease in the cooling time and height of the heat exchanger. By increasing the rate of hydrogen production, the diameter of the heat exchanger rises steadily due to an increase in the number of droplets produced per second. Figure 8-28 shows the effect of the hydrogen production rate on the heat exchanger diameter. For a hydrogen production rate of 1 kg/day, the volume of molten

droplets is less than 0.01% of the volume of the heat exchanger while for a hydrogen production of 1000 kg/day, it increases to about 0.2%.

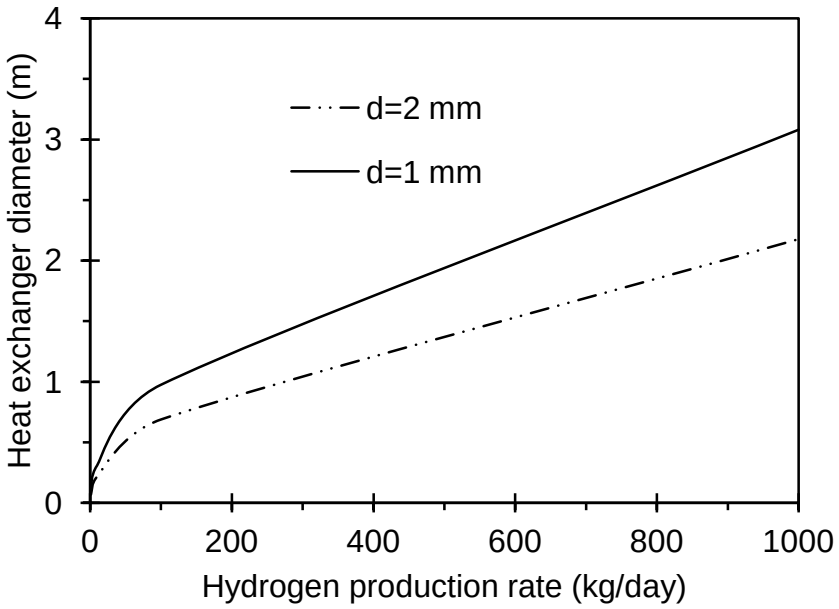

Figure 8-28 Diameter of the heat exchanger for recovering heat from molten CuCl versus the rate of hydrogen production

8.2.6 Potential chemical reactions

Copper(I) compounds are unstable in contact with air or water. The possible chemical reactions between copper(I) chloride and water or air will be examined in this section. At a temperature of less than 750^{o}C, the following reaction can occur:

$$2CuCl + {}^{1}/_{2}\, O_2 \rightarrow Cu_2O + Cl_2 \tag{8.1}$$

As the atmosphere contains moisture the following reaction may occur:

$$4CuCl + {}^{3}/_{2}\, O_2 + 3H_2O \rightarrow 2Cu_2(OH)_3Cl + Cl_2 \tag{8.2}$$

The copper(I) chloride may also react with water in the presence of oxygen as follows:

$$6CuCl + {}^{3}/_{2}\,O_2 + 7H_2O \rightarrow 2Cu_2(OH)_3Cl + 2[CuCl_2.2H_2O] \quad (8.3)$$

As stated in Chapter 7, two sets of experiments were performed at different conditions. In the first set of experiments, the solidified CuCl is taken from the water vessel and exposed to air (Figure 8-29). The color of the material changes from gray to green. Figures (8-30) and (8-31) show the x-ray diffraction results for two experiments. As expected, $Cu_2(OH)_3Cl$ and $CuCl_2.2H_2O$ are observed.

Figure 8-29 Solidified CuCl from the water vessel

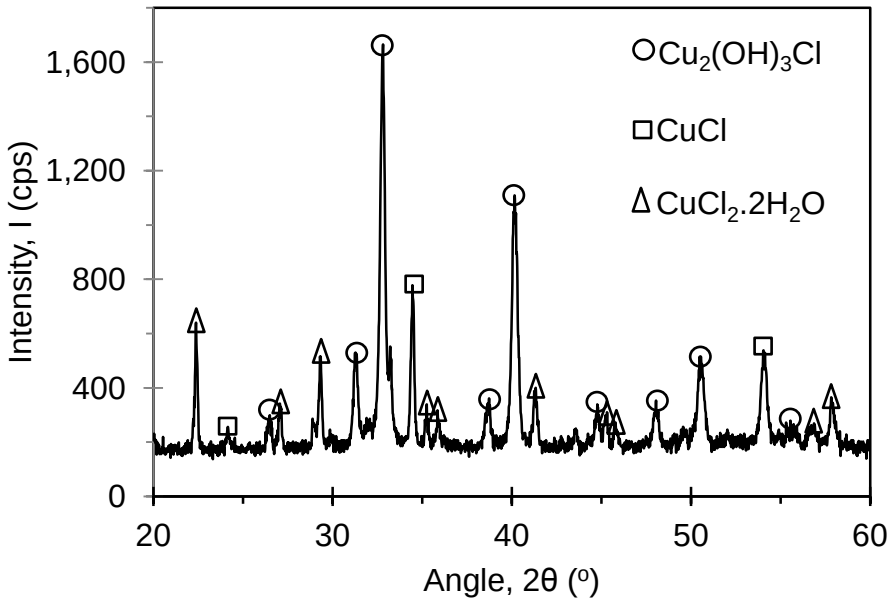

Figure 8-30 X-ray diffraction results for CuCl in contact with air and water

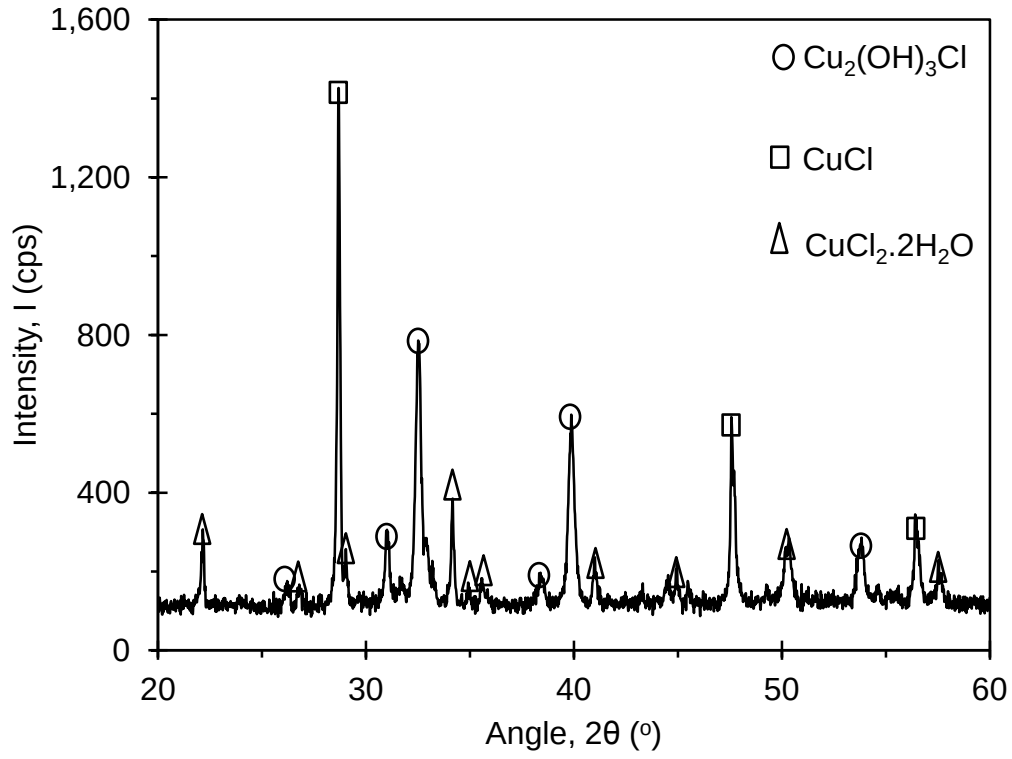

Figure 8-31 X-ray diffraction results for CuCl in contact with air and water

In the second set of experiments, solidified CuCl is kept in water in a small container, in a nitrogen glove box. Therefore, the material is not in contact with oxygen. In this case, the color of the material remains gray. The x-ray diffraction results are presented in Figures (8-32) and (8-33) for two experiments. It is observed that copper(I) chloride does not react with water in the absence of oxygen. It is also concluded that the molten droplets of CuCl do not react with air during the droplet descent. To avoid any chemical reactions, it is suggested to drop the molten CuCl droplets into water in an inert atmosphere. Also, the water might be deoxygenated. Further chemical analysis of the process is beyond the scope of this thesis and suggested for future research.

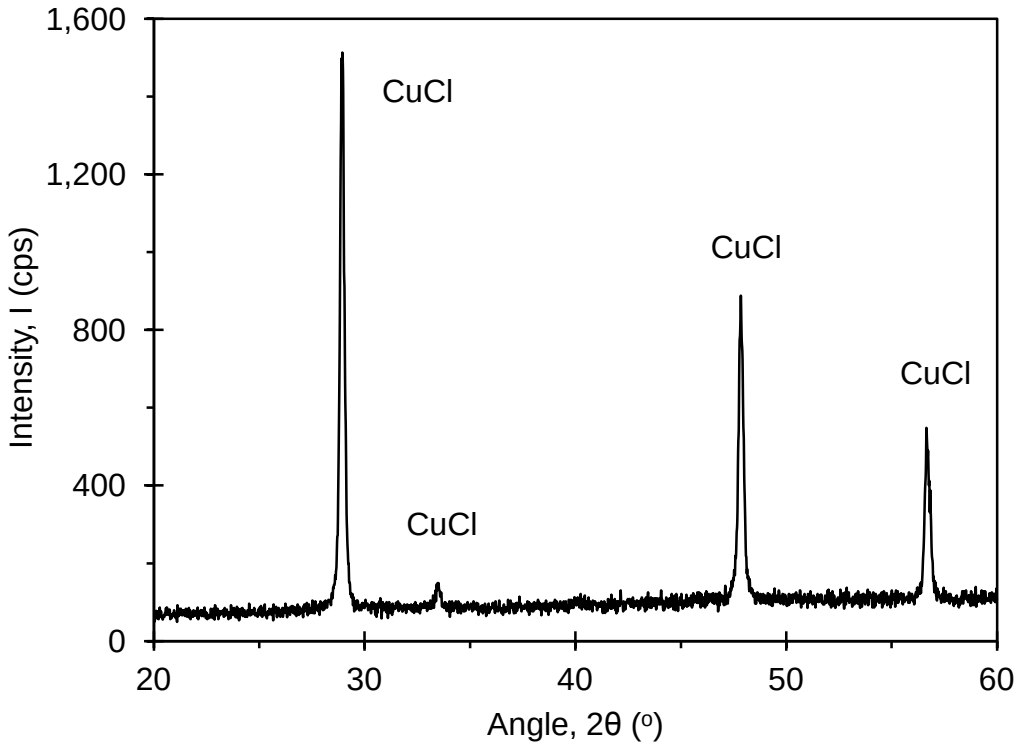

Figure 8-32 X-ray diffraction results for CuCl in contact with water

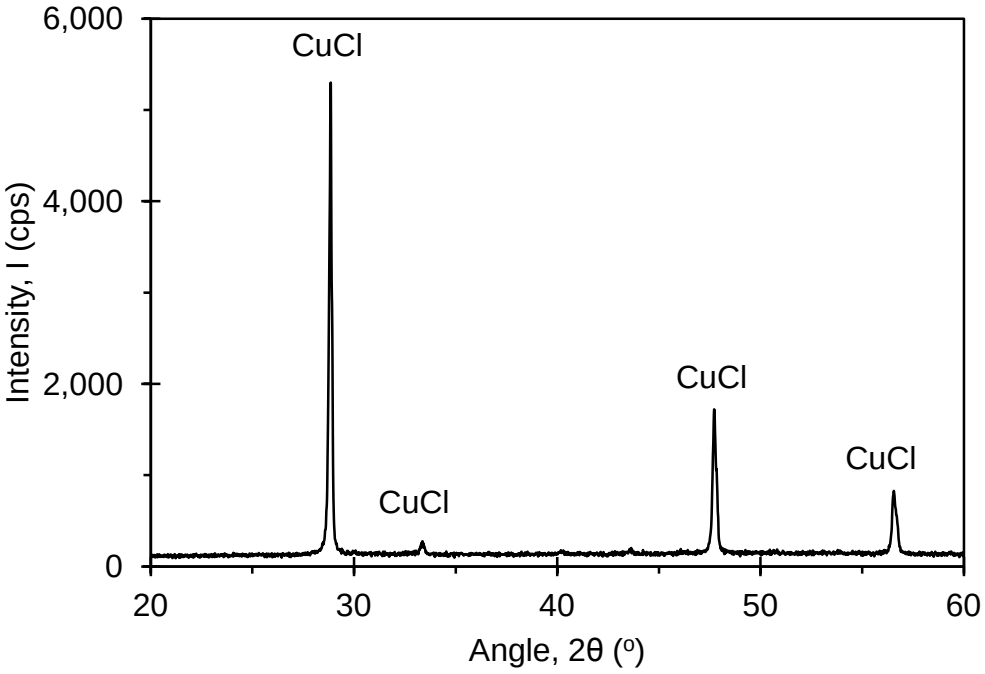

Figure 8-33 X-ray diffraction results for CuCl in contact with water

Chapter 9 Hazards Reduction

It is important to predict, control and reduce the hazards caused by the intermediate chemicals in the copper-chlorine cycle of hydrogen production. Copper(I) chloride (CuCl) is an intermediate compound that is always present regardless of the variations of the Cu-Cl cycle. CuCl may cause various health concerns, including irritation of eyes, nose and throat, pulmonary edema and congestion, anoxia, acute respiratory irritation, and metal fume fever [136].

The processing of CuCl in the cycle includes heat recovery, solidification, granulation, and dissolution. In this chapter, the hazards of CuCl are examined, from the perspectives of variations of the Cu-Cl cycle, heat recovery method, and equipment design. The hazards are examined by following the path along which CuCl is present or generated. Hazards reduction methods are explored to provide a safe working environment for operators. Besides hazards reduction, the CuCl must be recovered and returned to the Cu-Cl cycle, to avoid causing an imbalance of CuCl in the cycle. These issues were reported by Ghandehariun et al. [137].

9.1 Copper(I) chloride hazards at the generation source

As shown in Table 9-1, when oxygen is produced, molten CuCl is produced simultaneously [39]. As a consequence, CuCl vapor may be produced from its molten counterpart. Since oxygen must be transported outside of the reactor, the CuCl vapor may be entrained by oxygen gas to leave the Cu-Cl cycle. The entrainment quantity can be estimated from the partial pressure of vapor CuCl in the oxygen gas. To provide a safe

basis for a hazards reduction design, the worst scenario must be considered, wherein the oxygen gas is saturated with CuCl vapor. From thermodynamics, the saturation partial pressure is determined by the equilibrium vapor pressure of CuCl at the operating conditions. Figure 9-1 shows the equilibrium vapor pressure of the CuCl at different temperatures based on experimental data reported in past studies [138,139].

Table 9-1 Reaction steps in the Cu-Cl cycle

Variation	Step	Reaction	Temperature (^{o}C)
A (5-step)	1	$2Cu(s)+2HCl(g)\rightarrow 2CuCl(l)+H_2(g)$	450
	2	$2CuCl(s)+2HCl(aq)\rightarrow CuCl_2(aq)+Cu(s)$	25
	3	$2CuCl_2(aq)\rightarrow 2CuCl_2(s)$	60-80
	4	$2CuCl_2(s)+H_2O(g)\rightarrow Cu_2OCl_2(s)+2HCl(g)$	375
	5	$Cu_2OCl_2(s)\rightarrow 2CuCl(l)+1/2O_2(g)$	530
B (4-step)	1	$2CuCl(aq)+2HCl(aq)\rightarrow 2CuCl_2(aq)+H_2(g)$	70-90
	2	$2CuCl_2(aq)\rightarrow 2CuCl_2(s)$	60-80
	3	$2CuCl_2(s)+H_2O(g)\rightarrow Cu_2OCl_2(s)+2HCl(g)$	375
	4	$Cu_2OCl_2(s)\rightarrow 2CuCl(l)+1/2O_2(g)$	530

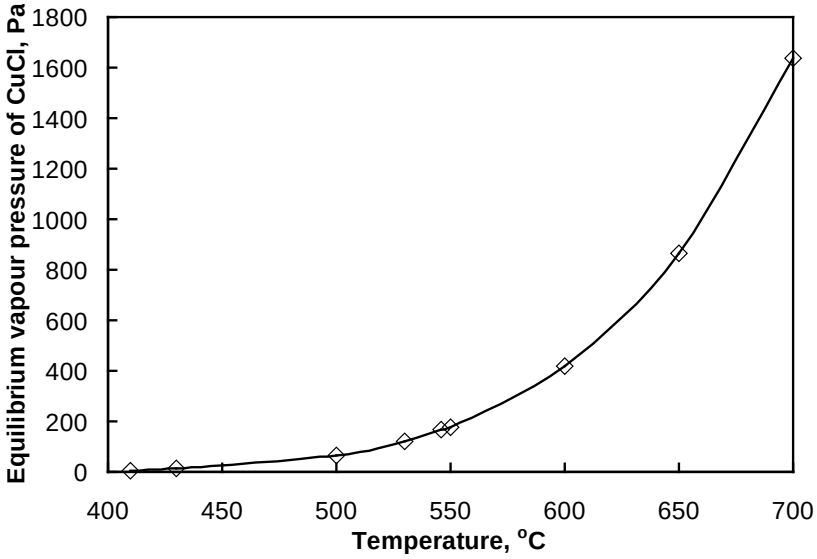

Figure 9-1 Equilibrium vapor pressure of CuCl at different temperatures

In terms of the avoidance of reverse and side reactions, the optimal operating pressure of the oxygen production reactor is suggested to be in the range of 120-200 kPa, (abs) which is about two orders of magnitude larger than the vapor pressure of CuCl in the range of oxygen production reaction temperature. Therefore, the total pressure of the reactor can be approximated by the oxygen gas pressure. If the oxygen is saturated with CuCl vapor, then the partial pressure of CuCl vapor in the oxygen gas, hence the production rate of CuCl vapor, will decrease when increasing the oxygen pressure of the reactor for the same production rate of oxygen. However, higher operating pressure may lead to an increase in the operating costs.

Table 9-2 shows the maximum copper(I) chloride vapor production rate in the oxygen production step of the 4-step Cu-Cl cycle (Variation B in Table 9-1) based on an industrial hydrogen production rate of 100 tons/day. In Table 9-2, the production rate at a temperature of 600^{o}C is also estimated by considering a scenario of accidentally losing temperature control of the oxygen production reactor. In the case of loss of control, the maximum temperature of the oxygen reactor is the heat source temperature because the oxygen production reaction is endothermic. The temperature increase will increase the CuCl vapor production rate, as the vapor pressure of CuCl increases with temperature. Therefore, a lower reactor temperature is suggested to reduce the CuCl hazards.

The maximum available temperature of the supercritical water-cooled nuclear reactors potentially serving as the heat source of the Cu-Cl cycle in the future is in the range of 550-650^{o}C. Considering the heat losses in the heat transport pipeline from the heat source to a thermochemical hydrogen production plant, 600^{o}C is adopted as the worst-case scenario of CuCl vapor generation. Higher temperatures can be supplied by

other types of Generation IV nuclear reactors and some solar thermal energy concentrating devices. The temperature of the oxygen reactor can be controlled by the heat transfer rate in the corresponding heat exchanger. The most advantageous way to reduce hazards often is to approach the reduction at the hazards production source. Therefore, a lower reaction temperature for the oxygen production reactor is preferred. For the 5-step cycle in Variation A, molten CuCl is produced in both hydrogen and oxygen production steps. Hence, the amount of CuCl vapor produced in Variation A is approximately two times the quantity in Variation B, as illustrated in Table 9-2. Therefore, Variation B for the selection of the Cu-Cl cycle is preferred from the perspective of CuCl hazards reduction.

Table 9-2 Production rate of CuCl vapor in the Cu-Cl cycle

P_{tot} (bar)	Production rate of CuCl vapor (kg/day)			
	4-step (Variation B)		5-step (Variation A)	
	T=530°C	T=600°C	T=530°C	T=600°C
1.2	2514	8584	5028	17168
1.4	2155	7358	4310	14715
1.6	1886	6438	3771	12876
1.8	1676	5723	3352	11445
2	1508	5150	3017	10300

To reduce the CuCl vapor at the production source, structures such as a mesh or filter could also be built inside the reactor. However, this may significantly increase the design and operating complexity of the oxygen production reactor. Another option is to cool the oxygen gas at the outlet of the reactor, so that CuCl vapor can be condensed. In this option, deposits of CuCl on the walls of the cooler should be cleaned regularly. The deposition is discussed in later sections of this chapter for the equipment design parameters to examine the feasibility of using cyclonic, tube-and-shell, and plate heat exchangers to collect the CuCl vapor.

9.2 Copper(I) chloride hazards on the path of process integration

As illustrated in Table 9-1, after the CuCl is produced in molten form in the oxygen production step, it is eventually utilized in the form of an aqueous solution in the electrolytic step. This means the molten salt will experience solidification, granulation, and dissolution in water for the process integration of oxygen and electrolytic steps. As presented in Chapter 4, the phase-change heat transfer can be recovered from the solidification so as to improve the overall thermal efficiency of the Cu-Cl cycle. Therefore, the reduction of the Cu-Cl hazards is dependent of the heat recovery method.

Atomization is one of the options for recovering heat from the molten CuCl due to its advantages of high heat recovery efficiency and the combination of solidification and granulation into a single process. In the atomization methods, CuCl vapor is entrained by the atomizing gas. The entrainment amount can be estimated with equilibrium vapor pressure data (Figure 9-1). However, since the drying gas flow rate may be larger than the oxygen production rate, entrainment in the drying gas may be more significant than the values presented in Table 9-2. Therefore, the heat recovery fluid should be circulated in a closed system; otherwise the CuCl vapor may enter the environment. As shown in Figure 9-2, to utilize the recovered heat, a secondary heat exchanger must be set up for heat transfer from the heated atomizing gas to an endothermic process in the Cu-Cl cycle. After the atomizing gas leaves the heat exchanger, it circulates back to the atomization chamber. In the loop, the build-up of deposited CuCl on the walls of the secondary heat exchanger and circulation pipes could become problematic due to solidification of the entrained CuCl vapor in the drying air. The deposition of CuCl is caused by the temperature decrease when the heat of atomizing gas is extracted in the secondary heat exchanger, so changing

the structure of the heat exchanger may not achieve a significant reduction of the CuCl build-up.

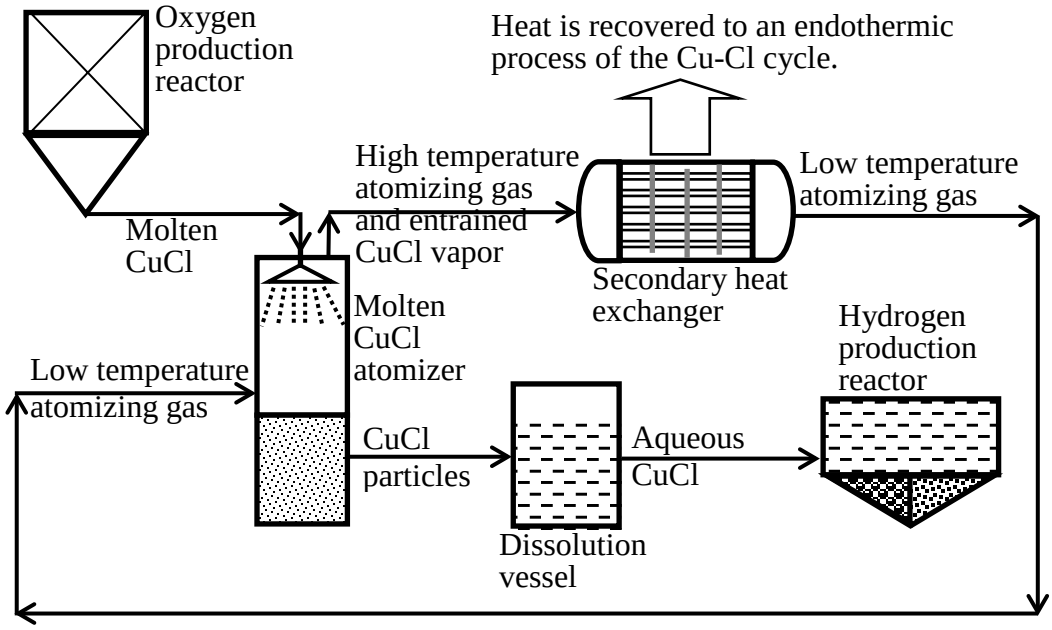

Figure 9-2 Confining the CuCl hazards in a closed loop for heat recovery with atomization of molten CuCl

Figure 9-3 illustrates another option for avoiding the secondary heat exchanger. In this method, the CuCl is atomized with liquid water to generate steam, which is utilized directly as the reactant of the hydrolysis step. However, it is very challenging to evaporate all water and generate high temperature steam in this method. An alternative of this method is to atomize the molten CuCl with steam, but with the steam generated in a separate vessel. The molten salt is pumped into the injection point at about 500-530^{o}C, and then atomized into small droplets by steam. During the descent, the droplets or particles of CuCl further transfer their residual heat to the upward flowing steam. CuCl is solidified completely in the vessel and forms a bed of hot solid particles. Solids from this bed are then discharged by a conveyor to a quenching vessel, and steam from the quenching vessel

flows into the granulation vessel. Superheated steam can be used in the hydrolysis reactor of the Cu-Cl cycle where steam is a reactant. This is also a significant advantage in terms of the direct circulation of CuCl vapor back to the Cu-Cl cycle with no need of a closed loop to process the atomizing gas. However, the steam must be pressurized in order to atomize the CuCl. The solid CuCl build-up on the wall of the conveying pipes remains an issue, except that the generated steam temperature is lower than the melting point of CuCl. Therefore, it is challenging to avoid the build-up of CuCl on the conveying pipe wall if the heat recovery with a working fluid adopts the direct contact method.

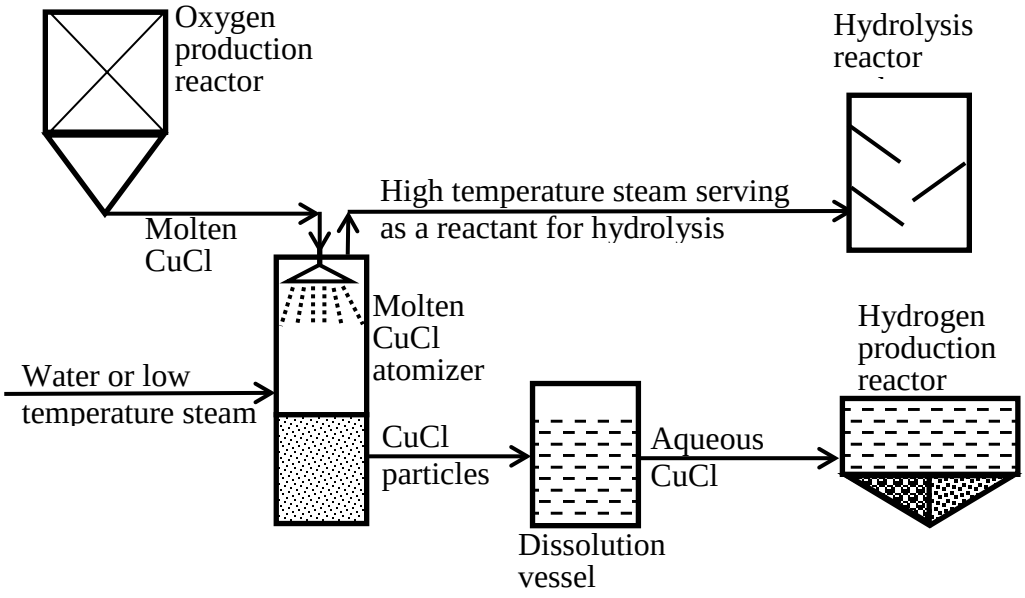

Figure 9-3 Circulating the entrained CuCl back to the Cu-Cl cycle in the heat recovery loop with water/steam atomization of molten CuCl

Figure 9-4 shows the loop of an indirect contact method for the heat recovery with casting/extrusion technology in a coaxial cylinder. In this method, the heat recovery fluid is not in direct contact with the hazards so the generated steam does not carry the CuCl vapor and high purity steam can be generated. But the solidified CuCl may need further granulation in order to improve its dissolution rate to form an aqueous solution. The

hazards accompanying the granulation are not discussed here as the solid confinement and processing is much less challenging than for the vapor.

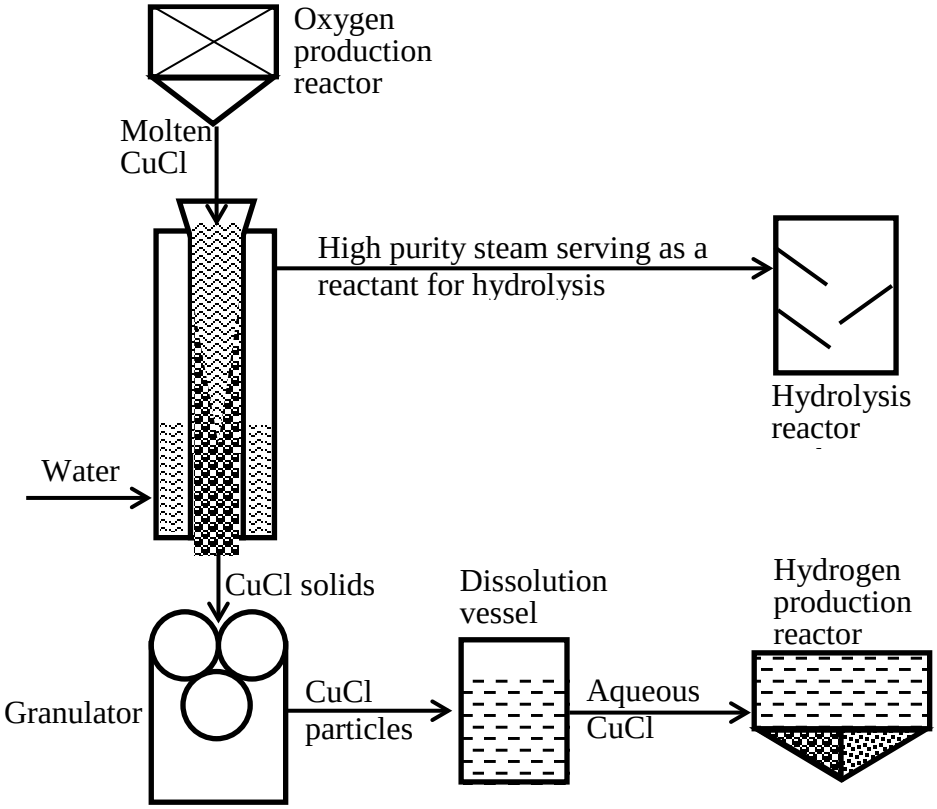

Figure 9-4 Confining the CuCl hazards in the casting/extrusion vessel in the heat recovery loop with an indirect contact method of steam generation

9.3 Major parameters for the oxygen processing and hazards reduction equipment

In addition to hydrogen, the thermochemical splitting of water produces oxygen, a potentially valuable by-product. Oxygen can be an oxidant of many fuels. Also, it can be used instead of N_2 in combustion of fossil fuels to increase CO_2 capture efficiency by eliminating the need for N_2-CO_2 separation. The oxygen normally cannot be distributed to end users with toxic CuCl entrained in it. The oxygen produced at 530^{o}C needs to be cooled to ambient temperature for storage and distribution. If the entrained CuCl vapor in the oxygen gas cannot be eliminated in the oxygen production reactor, then the CuCl

vapor will enter the oxygen cooler where the heat carried by oxygen gas is recovered or removed.

One option for removing CuCl hazards involves oxygen cooling. Oxygen gas exits the oxygen reactor at a temperature of 530°C, which is reduced to about 40°C in the cooler. The heat recovered from the oxygen can be used to heat $1{,}544\times10^3$ kg/day of water from 20 to about 80°C. Cooling the oxygen causes the CuCl vapor to condense and deposit on the walls. The deposited volume and thickness of CuCl are two major design parameters for the oxygen cooler or heat recovery apparatus. Estimates of the deposited volume of CuCl produced per day in the oxygen cooler are shown in Table 9-3. These values can also considered as the thickness of the CuCl solid per unit surface area.

Table 9-3 Deposition rate (volume) of CuCl on the walls of the oxygen cooler

P_{tot} (bar)	Rate of CuCl solid production (m^3/day)			
	Variation A (5-step)		Variation B (4-step)	
	T=530°C	T=600°C	T=530°C	T=600°C
1.2	1.21	4.14	0.61	2.07
1.4	1.04	3.55	0.52	1.77
1.6	0.91	3.11	0.45	1.55
1.8	0.81	2.76	0.40	1.38
2	0.73	2.49	0.36	1.24

The build-up of CuCl on the cooler wall will clog the oxygen flow path. To estimate the clogging rate, it is assumed that a conventional tube-and-shell cooler structured with a bundle of 1” (2.54 cm) tubes encapsulated in a large shell is used and the oxygen flows inside the tubes. The clogging rate can be characterized by the number of tubes that are filled with the volume of CuCl listed in Table 9-3. The numbers of clogged tubes at various operating conditions are illustrated in Table 9-4. The numbers are given for two cases: 1 meter long tubes, which can be utilized for the calculation of

any other lengths, and 20 meters long tubes, which is a typical value for a large industrial heat exchanger. It was found that the condensed CuCl may clog 72-120 tubes (inner diameter 2.54 cm and 20 meters long) per day. This excludes the feasibility of using a conventional tube-and-shell cooler. Although other types of coolers can be adopted in principle, the engineering feasibility of such options is low due to the high build-up rate of CuCl on the equipment wall.

Table 9-4 Clogging rate of CuCl on the walls of the oxygen cooler

Tube length (m)*	P_{tot} (bar)	Number of tubes clogged per day			
		Variation A (5-step)		Variation B (4-step)	
		T=530°C	T=600°C	T=530°C	T=600°C
1	1.2	2394	8174	1197	4087
	1.4	2052	7006	1026	3503
	1.6	1796	6130	898	3065
	1.8	1596	5450	798	2725
	2	1436	4904	718	2452
20	1.2	120	409	60	204
	1.4	103	350	51	175
	1.6	90	307	45	153
	1.8	80	273	40	136
	2	72	245	36	123

* Tube inner diameter = 2.54 cm.

The second option for removing CuCl hazards is to scrub the oxygen gas through a water bath, which removes the CuCl vapor. Figure 9-5 shows the experimental loop for scrubbing the CuCl vapor from the oxygen gas at UOIT's Clean Energy Research Laboratory (CERL). To improve the scrubbing efficiency, Pyrex Raschig rings are used to enhance the contact between oxygen gas and water. An energy balance shows that the make-up water required for the Cu-Cl cycle (900 tons/day for a hydrogen production rate of 100 tons/day) can be heated to about 123°C. This implies that water can be heated up to about 100°C in the case of 20% heat loss or 20% excess water. With this method, heated water containing CuCl can be directly transferred to the electrolysis step, which is

a significant advantage wherein all CuCl is recovered. The disadvantages of this method include oxygen gas dissolution in water, the existence of water vapor in the oxygen, and the possible loss of heat from the oxygen.

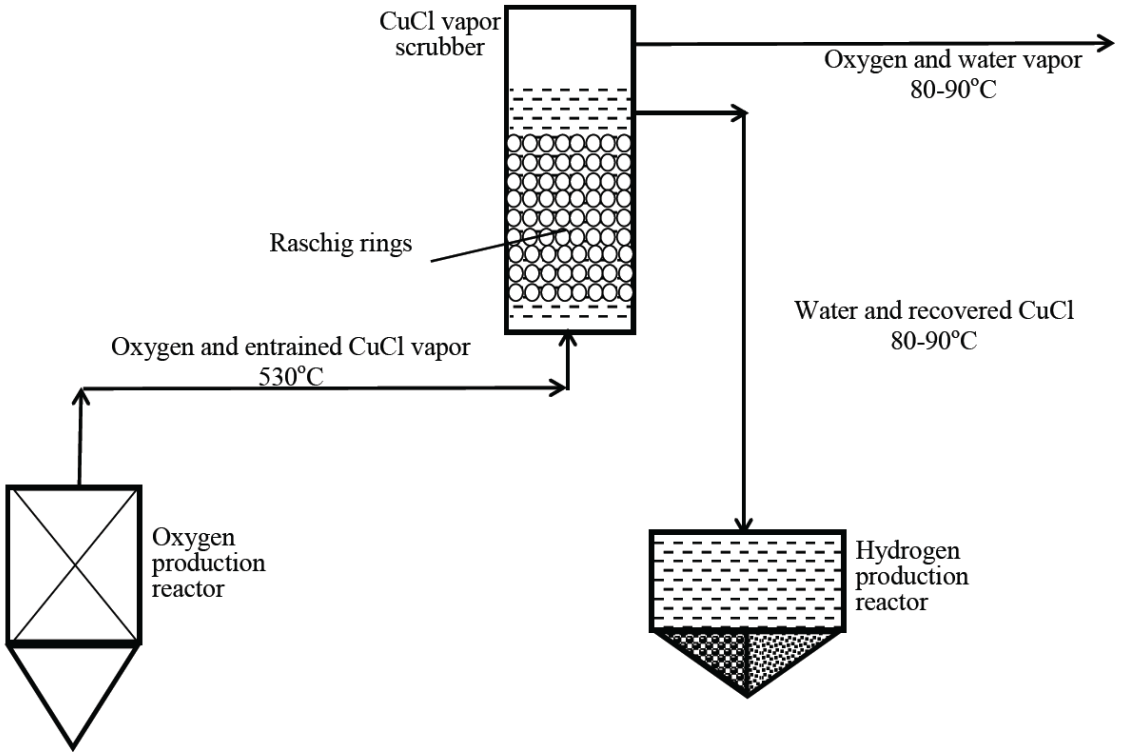

Figure 9-5 Water scrubbing for the recovery of CuCl to the hydrogen production reactor

Figure 9-6 illustrates another method for removing CuCl hazards. The oxygen is used to preheat Cu_2OCl_2 in a packed or fluidized bed heat exchanger. As shown in Table 9-1, the Cu_2OCl_2 is the reactant required for the oxygen production reactor and CuCl is a product of the decomposition of Cu_2OCl_2. Therefore, the introduction of CuCl into the oxygen production reactor does not have a disturbing effect on the composition of the reaction products. The heat recovered by cooling oxygen from 530°C to 390°C can be used for preheating copper oxychloride from 375°C to about 395°C. Since this

temperature is below the melting point of CuCl (430^{o}C), the CuCl solid is absorbed by the Cu_2OCl_2 solid and pure oxygen gas exits the packed or fluidized bed.

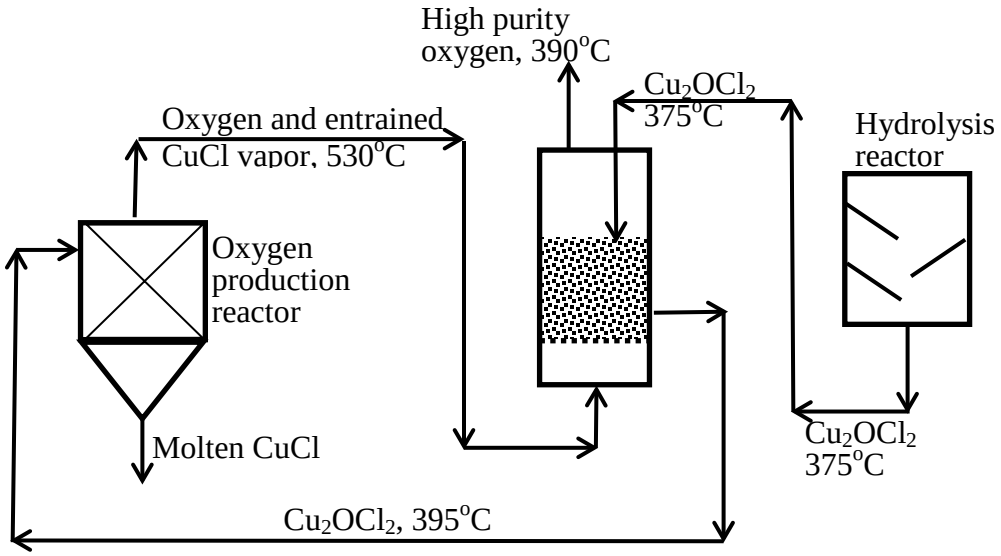

Figure 9-6 CuCl recovery with preheating of Cu_2OCl_2 by oxygen in a packed bed

In the above method, copper(II) chloride can be used as a substitute for Cu_2OCl_2 in the recovery of the CuCl vapor. As shown in Table 9.1, $CuCl_2$ is required in the hydrolysis step at 375^{o}C but it exits the drying step at about 80^{o}C. Therefore, the heat recovered from oxygen can be used to preheat $CuCl_2$ exiting the dryer at 100^{o}C and at the same time CuCl is absorbed by the $CuCl_2$ particles. The heat released during the cooling of oxygen gas from 530^{o}C to 120^{o}C can be used to heat the $CuCl_2$ to about 143^{o}C. However, our experiments show that the release of Cl_2 gas due to the decomposition of $CuCl_2$ at high temperature can be problematic in this process. Therefore, using Cu_2OCl_2 to recover the CuCl is preferred.

As mentioned above, the risk of using $CuCl_2$ to absorb CuCl vapor is the decomposition of $CuCl_2$ due to overheating by CuCl vapor. The decomposition of $CuCl_2$ will release CuCl and gaseous Cl_2, which is another hazardous gas. Similarly, the risk of

using Cu_2OCl_2 may also cause its decomposition to release CuCl and O_2. To avoid the decomposition, the operating temperature for CuCl absorption should be lower than the thermodynamically spontaneous level. Figure 9-7 shows the changes of the standard Gibbs energy of the two decomposition reactions. When the temperature is lower than 470^{o}C, the Gibbs energy change of the $CuCl_2$ decomposition reaction is positive, so the decomposition will not occur. In addition, CuCl vapor will exert a sequestration effect on the decomposition of $CuCl_2$, because CuCl is one of the decomposition products. Regarding the decomposition of Cu_2OCl_2, the Gibbs energy change is positive when the temperature is lower than 530^{o}C, so the decomposition of Cu_2OCl_2 will not take place below 395^{o}C. In addition, since CuCl vapor is produced in the oxygen production step and carried by O_2 to enter the CuCl absorption bed. The decomposition of Cu_2OCl_2 will be sequestered thermodynamically by the coexistence of O_2 and CuCl vapor in a stoichiometric ratio.

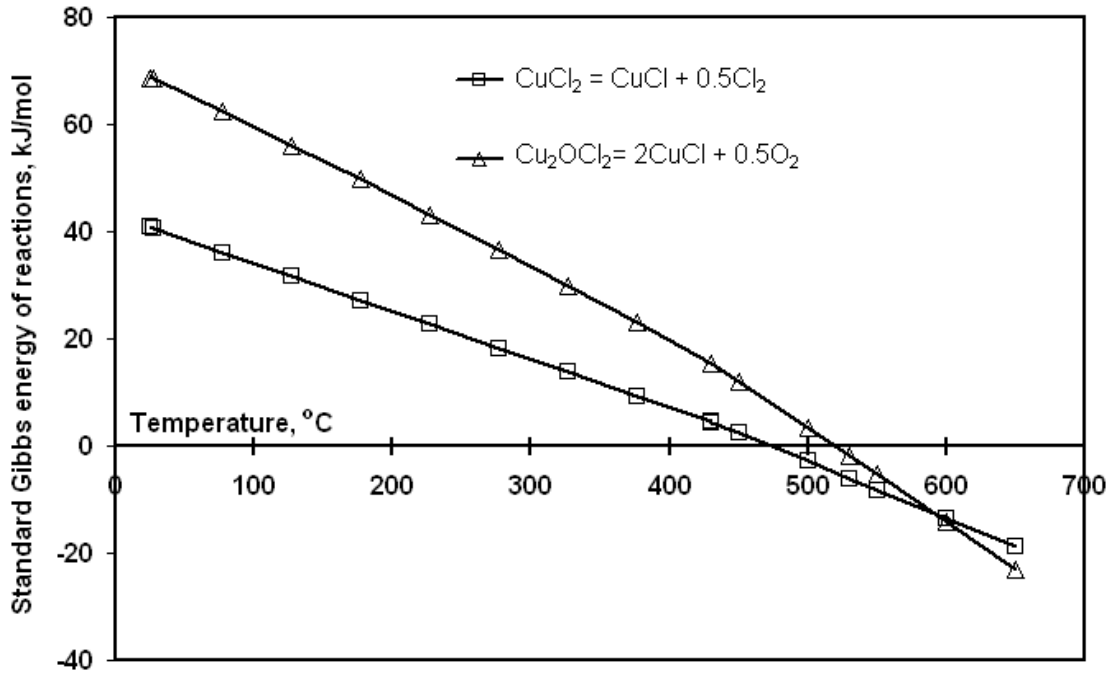

Figure 9-7 Thermodynamic spontaneity of the decomposition of $CuCl_2$ and Cu_2OCl_2

9.4 Experimental studies for CuCl recovery

Figure 9-8 shows the experimental loop prepared to investigate the feasibility of the CuCl recovery method in Figure 9-6. Molten CuCl is generated in the furnace. The temperature range is 450-600^{o}C. Raschig rings made from Pyrex glass, with a radius and height of 12 mm and a thickness of 1 mm, provide an absorption bed for CuCl vapor. Two type K thermocouples measure the temperature of the buffer chamber and the absorption bed.

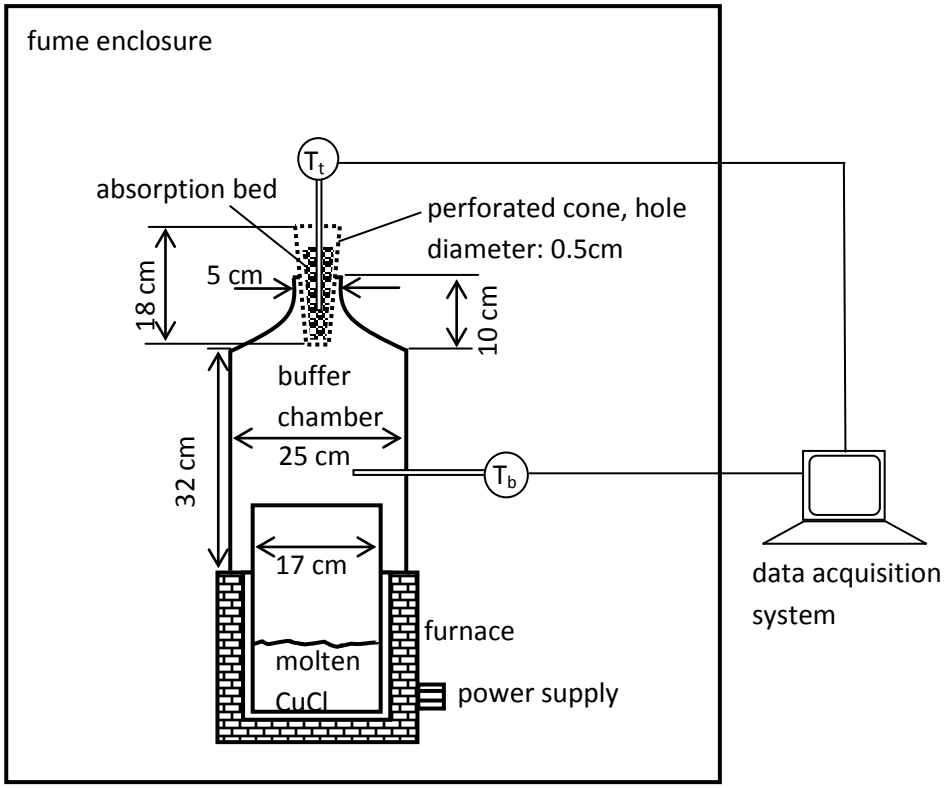

Figure 9-8 Experimental loop for recovering CuCl

The diameter of the buffer chamber is 5 times the absorption bed, thus the cross sectional area is 25 times contracted when the gas stream enters the bed. This setup simulates the future layout comprising a buffer chamber and an immediate downstream heat exchanger with a much smaller cross-sectional area than the buffer chamber. The height of the buffer chamber is larger than the absorption bed, so that the deposition

quantity of CuCl vapor on the chamber wall can be compared with the absorbed quantity of CuCl by the absorption bed. Figure 9-9 shows the raschig rings coated by CuCl. Experimental results show that 70% of the CuCl vapor was absorbed by the absorption bed, although the residence time in the buffer chamber was at least 25 times longer than the absorption bed. This suggests that the vapor would mostly enter the heat exchanger, settling immediately downstream of the buffer chamber. Figure 9-10 shows the variation of the temperature of the absorption bed with time. The temperature of the absorption bed can be increased by 50^{o}C within 40 minutes.

Figure 9-9 Raschig rings coated by CuCl

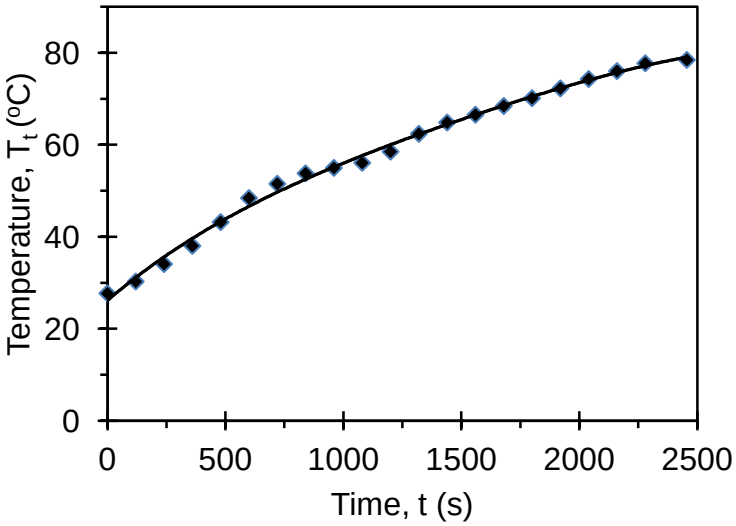

Figure 9-10 Temperature of absorption bed with time

9.5 Confined space for the integration of oxygen reactor and heat recovery

Mechanical ventilation and filtration are required in case the control of hazards with the above methods is not ideal or if malfunctions occur. Pouring molten CuCl from the oxygen reactor into the heat recovery chamber generates a cloud of fumes which is toxic and hazardous. Therefore, the entire pouring system should be confined. A confined space is defined as a space which is substantially enclosed and used where there is a reasonably foreseeable risk of serious injury from hazardous substances or conditions within the space. Entry to the confined space is restricted and usually entails the use of comprehensive personal protective equipment.

Adverse conditions of the atmosphere inside the confined space constitute the most common cause for potential accidents, serious injuries and fatalities in a confined space. Physical configurations, such as the shape and size of the space and locations of openings, significantly affect ventilation requirements and strategies. Environmental conditions outside and inside of the space are also important. There are two basic operations for ventilating confined spaces: natural ventilation and mechanical ventilation. Mechanical ventilation offers two principal alternatives: air supplied and/or exhausted from the space. Exhaust ventilation may be localized or general within the space. Ventilation alternatives exhibit different advantages and disadvantages and require careful evaluation for a given confined space.

Natural ventilation frequently is inadequate and normally not acceptable as a primary means of ventilating a confined space. Mechanical ventilation uses mechanical equipment to force and control air flow within the confined space, and has the advantages of flexibility and control for directing air movement. The primary disadvantage of

mechanical ventilation is the possibility of mechanical failure, resulting in little or no ventilation. This potential hazard should be reduced by appropriate back-up and fail-safe provisions. Mechanical ventilation involves the cost of the equipment and time to plan, prepare and implement its use. Despite possible disadvantages, mechanical ventilation is usually the best way to minimize the hazards of adverse atmospheric conditions in confined spaces. Mechanical ventilation of the workplace is also required in case of leakage of CuCl vapor out of the confined pouring system.

Chapter 10 Conclusions and Recommendations

10.1 Conclusions

In this thesis, recycling of thermal energy within the copper-chlorine (Cu-Cl) cycle of hydrogen production was investigated. A pinch analysis showed that about 88% of the recovered heat can be achieved by cooling and solidifying molten copper(I) chloride exiting the fourth step (i.e. oxygen production step) of the Cu-Cl cycle. Two alternatives for using the recovered heat in the cycle are presented. All of the recovered heat from molten CuCl and oxygen gas can be used in the drying step, or a portion of heat recovery can be used to produce superheated steam for hydrolysis and the remainder for the drying step. Considering the integration of internal and external heat flows, it is more efficient if the recovered heat is used in the hydrolysis step.

Several configurations for recovering heat from molten CuCl were presented. These processes include atomization and steam generation within a quench bath, atomization with droplets falling through counter-current flow, atomization by air or other inert gases, rotary/spinning atomization, casting/extrusion, and a drum flaker. Several parameters such as the heat transfer rate, the potential of introducing additional materials into the cycle, energy efficiency, temperature retention, economics, material issues, and design feasibility are considered in the evaluation these methods.

Based on the present comparative assessment, the casting/extrusion method, atomization with a separate vessel using water as a coolant, and rotary/spinning atomization using air as a coolant were found to be the most promising processes for heat

recovery from molten CuCl in the Cu-Cl cycle, and were recommended for further investigation.

The casting/extrusion method includes indirect-contact heat transfer while the atomization method represents direct-contact heat transfer. Predictive models were developed to study both processes of heat recovery. A double-pipe heat exchanger (i.e. indirect-contact heat exchanger) was investigated in detail for recovering heat from molten CuCl. Counter-current air flow, with rates of 3 and 4 g/s, was considered as a coolant. It was shown that the air temperature increases to 190^{o}C in a heat exchanger with a length of 15 cm and inner tube radius of 10 cm. The length of a heat exchanger with the inner tube radius of 12 cm is 53 cm. The outlet temperature of air is about 380^{o}C in this case.

The length of a heat exchanger with an inner tube diameter of 24 cm is about 53 cm and 91 cm for coolant flow rates of 3 g/s and 4 g/s, respectively. Increasing the mass flow rate of air will increase the total heat flux from the molten salt by increasing the length of the heat exchanger.

A spray column (i.e. direct contact heat exchanger) was examined for recovering heat from molten CuCl droplets to the flowing steam (or any gas). The molten droplets are released from the top of the system while steam flows upward. The heat transfer rate from the freely falling droplets to the flowing steam was evaluated. Different modes of heat transfer (i.e. convection, radiation, heat transfer due to mass transfer) were estimated and compared. It was shown that heat transfer due to evaporation was negligible compared with convection and radiation.

Characteristics of a direct-contact heat exchanger, in which recovered heat from molten CuCl was used to produce superheated steam, were presented. For a hydrogen production rate of 1 kg/day, the flow rates of CuCl and steam are 1.15 kg/s and 0.12 kg/s, respectively. The height of the heat exchanger was dominated by the heat transfer rate. Decreasing the droplet size may increase the heat transfer rate from the droplet, and hence decreases the required height of the heat exchanger. For a droplet size of 2 mm, the height of the heat exchanger is 23 m, while for a droplet of 1 mm, the height is 7 m. Increasing the relative droplet-steam velocity increases the heat transfer rate, which yields a decrease in the cooling time and height of the heat exchanger. The effect of hydrogen production on the heat exchanger diameter was also shown. For a hydrogen production rate of 1000 kg/day, the diameter of the heat exchanger is about 3 m for a droplet size of 1 mm and 2.2 m for a droplet size of 2 mm.

Experimental studies were performed to examine the behavior of molten CuCl droplets in air and water. X-ray diffraction analysis of the solidified products showed that CuCl does not react with water in the absence of oxygen.

The hazards involving copper(I) chloride were investigated, as well as corresponding hazard reduction options. The hazards accompanying the generation source and flow path were considered. The options for the CuCl hazards reduction were also evaluated from the perspectives of process integration, heat recovery and equipment design. It is concluded that using the reactant Cu_2OCl_2 in the oxygen production step to absorb CuCl vapor is the most preferable option compared to the alternatives, which include absorbing CuCl vapor with water or $CuCl_2$ and building additional structures inside the oxygen production reactor. Utilization of a cooler at the outlet of the oxygen

reactor to deposit CuCl vapor was found to be undesirable because of the large clogging rate of the oxygen flowing channels. If the atomization method is used for heat recovery from molten CuCl, the heat recovery fluid should be circulated in the thermochemical cycle so as to confine the CuCl vapor within the Cu-Cl cycle, and a secondary heat exchanger should be used to release heat to an endothermic process. Clogging of the heat exchanger by deposited CuCl is also a significant issue. Experimental studies verified the concept of CuCl recovery and hazards reduction in the thermochemical hydrogen production cycle.

10.2 Recommendations

The main suggestions and recommendations are described as follows. A double-pipe heat exchanger for heat recovery from molten CuCl should be studied further. The current model should be further expanded and the variation of properties with temperature should be considered. Experimental studies should be performed to investigate the behavior of solidified flow of CuCl and methods of removing the solid from the pipe.

More experimental studies are required for a spray column. A closed system should be tested and the increase in coolant temperature should be measured. The effect of different parameters and conditions (i.e. droplet size, droplet interactions, etc.) on the heat transfer rate from molten CuCl droplets needs to be investigated in more detail.

Detailed chemical analysis should be performed to investigate the possibility of chemical reactions between molten CuCl and the surrounding gas or steam in a direct-contact heat exchanger in a steady-state process.

Detailed material and cost analyses of the proposed heat recovery systems are suggested for future research. Also, exergy analysis of the systems is recommended to examine the processes from the exergy efficiency perspective.

The current experimental setup verifies the concept of CuCl recovery and hazards reduction in the copper-chlorine cycle. However, additional experiments including $CuCl_2$ and Cu_2OCl_2 packed beds, and more detailed analyses, are also recommended for future research. Chemical reactions that may accompany the CuCl recovery process should also be investigated experimentally.

References

[1] T. N. Veziroglu, S. Sahin, "21st century's energy", *Energy Conversion and Management*, Vol. 49, pp. 1820-1831, 2008.

[2] R. L. Nersesian, Energy for the 21st century: A comprehensive guide to conventional and alternative sources, Second Edition. M. E. Sharpe, Armonk, NY, 2010.

[3] A. F. Ghoniem, "Needs, resources and climate change: Clean and efficient conversion technologies", *Progress in Energy and Combustion Science*, Vol. 37, pp. 15-51, 2011.

[4] P. Ekins, Hydrogen energy: economic and social challenges, Earthscan, London, UK, 2010.

[5] K. Christopher, R. Dimitrios, "A review on exergy comparison of hydrogen production methods from renewable energy sources", *Energy and Environmental Science*, Vol. 5, pp. 6640-6651, 2012.

[6] A. Midilli, I. Dincer, "Hydrogen as a renewable and sustainable solution in reducing global fossil fuel consumption", *International Journal of Hydrogen Energy*, Vol. 33, pp. 4209-4222, 2008.

[7] R. Dell, Clean energy. Royal Society of Chemistry. London, UK, 2004.

[8] R. Kothari, D. Buddhiand, R. L. Sawhney, "Comparison of environmental and economic aspects of various hydrogen production methods", *Renewable and Sustainable Energy Reviews*, Vol. 12, pp. 553-563, 2008.

[9] M. A. Rosen, "Advances in hydrogen production by thermochemical water decomposition: A review", *Energy*, Vol. 35, pp. 1068-1076, 2010.

[10] M. A. Lewis, C. Sink, "High temperature thermochemical processes", DOE Hydrogen Program, Annual Progress Report, pp. 240-244, 2008.

[11] M. A. Lewis, J. G. Masin, P. A. O'Hare, "Evaluation of alternative thermochemical cycles, Part I: The methodology", *International Journal of Hydrogen Energy*, Vol. 34, pp. 4115-4124, 2009.

[12] M. A. Lewis, J. G. Masin, “The evaluation of alternative thermochemical cycles – Part II: The down-selection process”, *International Journal of Hydrogen Energy*, Vol. 34, pp. 4125-4135, 2009.

[13] M. A. Lewis, M. S. Ferrandon, D. F. Tatterson, P. Mathias, “Evaluation of alternative thermochemical cycles – Part III further development of the Cu-Cl cycle”, *International Journal of Hydrogen Energy*, Vol. 34, pp. 4136-4145, 2009.

[14] P. P. Edwards, V. I. Kuznetsov, W. I. F. David, N. P. Brandon, “Hydrogen and fuel cells: Towards a sustainable energy future”, *Energy Policy*, Vol 36, pp. 4356-4362, 2008.

[15] E. Martinot, C. Dienst, L. Weiliang, C. Qimin, “Reneable energy futures: Targets, scenarios, and pathways”, *Annual Review of Environment and Resources*, Vol. 32, 205-239, 2007.

[16] N. Lior, “Energy resources and use: The present situation and possible paths to the future”, *Energy*, Vol. 33, pp. 842-857, 2008.

[17] A. Verbruggen, “Renewable and nuclear power: A common future?”, *Energy Policy*, Vol. 36, pp. 4036-4047, 2008.

[18] J. Twidell, T. Weir, Renewable energy resources, Second Edition, Taylor and Francis, 2006.

[19] A. Midilli, M. Ay, M. A. Rosen, “On hydrogen and hydrogen energy strategies I: current status and needs”, *Renewable and sustainable energy reviews*, Vol. 9, pp. 255-271, 2005.[20] C. Winter, “Hydrogen energy - Abundant, efficient, clean: A debate over the-energy-system-of-change”, *International Journal of Hydrogen Energy*, Vol. 34, pp. 1-59, 2009.

[21] J. Nowotny, T. N. Veziroglu, “Impact of hydrogen on the environment”, *International Journal of Hydrogen Energy*, Vol. 36, 3218-3224, 2011.

[22] P. Marioarty, D. Honnery, “Hydrogen’s role in an uncertain energy future”, *International Journal of Hydrogen Energy*, Vol. 34, pp. 31-39, 2009.

[23] I. Dincer, M. A. Rosen, “Sustainability aspects of hydrogen and fuel cell systems”, Energy for Sustanable Development, Vol. 15, pp. 137-146, 2011.

[24] F. Barbir, “PEM electrolysis for production of hydrogen from renewable energy sources”, *Solar Energy*, Vol. 78, pp. 661-669, 2005.

[25] C. W. Forsberg, “Hydrogen, nuclear energy, and the advanced nuclear reactor”, *International Journal of Hydrogen Energy*, Vol. 28, pp. 1073-1081, 2003.

[26] J. M. Ogden, “Prospects for building a hydrogen energy infrastructure”, *Annual Review of Energy and Environment*, Vol. 24, pp. 227–279, 1999.

[27] S. Saito, “Nuclear energy and hydrogen production. The Japanese situation”, Policy Debate on the Potential Contribution of Nuclear Energy to Production of Hydrogen, OECD/NEA, 15 October 2004.

[28] I. Dincer, M. T. Balta, “Potential thermochemical and hybrid cycles for nuclear-based hydrogen production”, *International Journal of Energy Research*, Vol. 35, pp. 123-137, 2011.

[29] J. E. Funk, “Thermochemical hydrogen production: past and present”, *International Journal of Hydrogen Energy*, Vol. 26, pp. 185-190, 2001.

[30] S. Abanades, P. Charvin, F. Lemont, G. Flamant, “Novel two-step SnO_2/SnO water-splitting cycle for solar thermochemical production of hydrogen”, *International Journal of Hydrogen Energy*, Vol. 33, pp. 6021-6030, 2008.

[31] A. Steinfeld, “Solar hydrogen production via a two-step water splitting thermochemical cycle based on Zn/ZnO redox reactions”, *International Journal of Hydrogen Energy*, Vol. 27, pp. 611-619, 2002.

[32] M. E. Galvez, A. Frei, G. Albisetti, G. Lunardi , A. Steinfeld, “Solar hydrogen production via a two-step thermochemical process based on MgO/Mg redox reactions-thermodynamic and kinetic analyses”, *International Journal of Hydrogen Energy*, Vol. 33, pp. 2880-2890, 2008.

[33] S. Abanades, G. Flamant, “Thermochemical hydrogen production from a two-step solar-driven water-splitting cycle based on cerium oxides”, *Solar Energy*, Vol. 80, pp. 1611-1623, 2006.

[34] C. Huang, A. T. Raissi, “Analysis of sulfure iodine thermochemical cycle for solar hydrogen production. Part I: Decomposition of sulfuric acid”, *Solar Energy*, Vol. 78, pp. 632-646, 2005.

[35] W. Xinxin, O. Kaoru, “Thermochemical water splitting for hydrogen production utilizing nuclear heat from an HTGR”, *Tsinghua Science and Technology*, Vol. 10, pp. 270-276, 2005.

[36] R. Liberatore, M. Lanchi, A. Giaconia, P. Tarquini, “Energy and economic assessment of an industrial plant for the hydrogen production by water-splitting through the sulfur-iodine thermochemical cycle powered by concentrated solar energy”, *International Journal of Hydrogen Energy*, Vol. 37, 9550-9565, 2012.

[37] D. Graf, N. Monnerie, M. Roeb, M. Schmitz, C. Sattler, “Economic comparison of solar hydrogen generation by means of thermochemical cycles and electrolysis”, *International Journal of Hydrogen Energy*, Vol. 33, pp. 4511-4519, 2008.

[38] M. Granovskii, I. Dincer, M. A. Rosen, I. Pioro, “Performance assessment of a combined system to link a supercritical water-cooled nuclear reactor and a thermochemical water splitting cycle for hydrogen production”, *Energy Conversion and Management*, Vol. 49, pp. 1873-1881, 2008.

[39] Z. L. Wang, G. F. Naterer, K. S. Gabriel, R. Gravelsins, V. N. Daggupati, “Comparison of different copper-chlorine thermochemical cycles for hydrogen production”, *International Journal of Hydrogen Energy*, Vol. 34, pp. 3267-3276, 2009.

[40] M. Serban, M. A. Lewis, J. K. Basco, “Kinetic study of the hydrogen and oxygen production reactions in the copper-chloride thermochemical cycle”, AIChE 2004 Spring National Meeting, New Orleans, LA, 2004.

[41] M. T. Balta, I. Dincer, A. Hepbasli, “Energy and exergy analyses of a new four-step copper-chlorine cycle for geothermal-based hydrogen production”, *Energy*, Vol. 35, pp. 3263-3272, 2010.

[42] Z. L. Wang, G. F. Naterer, K. S. Gabriel, R. Gravelsins, V. N. Daggupati, “Comparison of sulfur-iodine and copper-chlorine thermochemical hydrogen production cycles”, *International Journal of Hydrogen Energy*, Vol. 35, pp. 4820-4830, 2010.

[43] S. Ghandehariun, G. F. Naterer, I. Dincer, M. A. Rosen, “Solar thermochemical plant analysis for hydrogen production with copper-chlorine cycle”, *International Journal of Hydrogen Energy*, Vol. 35, pp. 8511-8520, 2010.

[44] G. F. Naterer, S. Suppiah, M. Lewis, K. Gabriel, I. Dincer, M. A. Rosen, M. Fowler, G. Rizvi, E. B. Easton, B. M. Ikeda, M. H. Kaye, L. Lu, I. Pioro, P. Spekkens, P. Tremaine, J. Mostaghimi, A. Avsec, J. Jiang, “Recent Canadian advances in nuclear-based hydrogen production and the thermochemical Cu-Cl cycle”, *International Journal of Hydrogen Energy*, Vol. 34, pp. 2901-2917, 2009.

[45] G. F. Naterer, S. Suppiah, L. Stolberg, M. Lewis, M. Ferrandon, Z. Wang, I. Dincer, K. Gabriel, M. A. Rosen, E. Secnik, E. B. Easton, L. Trevani, I. Pioro, P. Tremaine, S. Lvov, J. Jiang, “Canada’s program on nuclear hydrogen production and the thermochemical Cu-Cl cycle.”, *International Journal of Hydrogen Energy*, Vol. 36, pp. 15472-15485, 2011.

[46] G. F. Naterer, S. Suppiah, L. Stolberg, M. Lewis, M. Ferrandon, Z. Wang, I. Dincer, K. Gabriel, M. A. Rosen, E. Secnik, E. B. Easton, L. Trevani, I. Pioro, P. Tremaine, S. Lvov, J. Jiang, “Clean hydrogen production with the Cu-Cl cycle – Progress of international consortium, I: Experimental unit operations”, *International Journal of Hydrogen Energy*, Vol. 36, pp. 15486-15501, 2011.

[47] G. F. Naterer, S. Suppiah, L. Stolberg, M. Lewis, M. Ferrandon, Z. Wang, I. Dincer, K. Gabriel, M. A. Rosen, E. Secnik, E. B. Easton, L. Trevani, I. Pioro, P. Tremaine, S. Lvov, J. Jiang, “Clean hydrogen production with the Cu-Cl cycle – Progress of

international consortium, II: Simulations, thermochemical data and materials", *International Journal of Hydrogen Energy*, Vol. 36, pp. 15486-15501, 2011.

[48] M. F. Orhan, I. Dincer, G. F. Naterer, M. A. Rosen, "Coupling of copper-chloride hybrid thermochemical water splitting cycle with a desalination plant for hydrogen production from nuclear energy", *International Journal of Hydrogen Energy*, Vol. 35, pp. 1560-1574, 2010.

[49] M. F. Orhan, I. Dincer, G. F. Naterer, "Cost analysis of a thermochemical Cu-Cl pilot plant for nuclear-based hydrogen production", *International Journal of Hydrogen Energy*, Vol. 33, pp. 6006-6020, 2008.

[50] C. Zamfirescu, I. Dincer, G. F. Naterer, "Thermophysical properties of copper compounds in the copper-chlorine thermochemical water splitting cycles", *International Journal of Hydrogen Energy*, Vol. 35, pp. 4839-4852, 2010.

[51] A. Ozbilen, I. Dincer, M. A. Rosen, "Environmental evaluation of hydrogen production via thermochemical water splitting using the Cu-Cl cycle: A parametric study, *International Journal of Hydrogen Energy*, Vol. 36, pp. 9514-9528, 2011.

[52] M. S. Ferrandon, M. A. Lewis, D. F. Tatterson, A. Gross, D. Doizi, L. Croize, V. Dauvois, J. L. Roujou, Y. Zanella, P. Carles, "Hydrogen production by a Cu-Cl thermochemical cycle: Investigation of the key step of hydrolysing $CuCl_2$ to Cu_2OCl_2 and HCl using a spray reactor", *International Journal of Hydrogen Energy*, Vol. 35, pp. 992-1000, 2010.

[53] G. F. Naterer, V. N. Daggupati, G. Marin, K. S. Gabriel, Z. L. Wang, "Thermochemical hydrogen production with a copper-chlorine cycle, II: Flashing and drying of aqueous cupric chloride", *International Journal of Hydrogen Energy*, Vol. 33, pp. 5451-5459, 2008.

[54] G. F. Naterer, K. Gabriel, Z. L. Wang, V. N. Daggupati, R. Gravelsins, "Thermochemical hydrogen production with a copper-chlorine cycle. I: Oxygen release from copper oxychloride decomposition", *International Journal of Hydrogen Energy*, Vol. 33, pp. 5439-5450, 2008.

[55] Z. Wang, G. F. Naterer, K. Gabriel, “Multiphase reactor scale-up for Cu-Cl thermochemical hydrogen production”, *International Journal of Hydrogen Energy*, Vol. 33, pp. 6934-6946, 2008.

[56] M. F. Orhan, I. Dincer, M. A. Rosen, “Design of systems for hydrogen production based on the Cu-Cl thermochemical water decomposition cycle: Configurations and performance”, *International Journal of Hydrogen Energy*, Vol. 36, pp. 11309-11320, 2011.

[57] O. Jaber, G. F. Naterer, I. Dincer, “Heat recovery from molten CuCl in the Cu-Cl cycle of hydrogen produuction.” *International Journal of Hydrogen Energy*, Vol. 35, pp. 6140-6151, 2010.

[58] C. Zamfirescu, G. F. Naterer, I. Dincer, “Vapor compression CuCl heat pump integrated with a thermochemical water splitting plant”, *Thermochimica Acta*, Vol. 512, pp. 40-48, 2011.

[59] M. Rabbani, I. Dincer, G. F. Naterer, M. Aydin, “Determining parameters of heat exchangers for heat recovery in a Cu-Cl thermochemical hydrogen production cycle”, *International Journal of Hydrogen Energy*, Vol. 37, pp.11021-11034, 2012.

[60] R. B. Bird, W. E. Stewart, E. N. Lightfoot, “Transport phenomena”, Wiley, New York, 1960.

[61] P. D. Richardson, “Estimation of the heat transfer from the rear of an immersed body to the region of separated flow”, WADD TN 59-1, Division of Engineering, Brown University, January 1960.

[62] G. C. Vliet, G. Leppert, “Forced convection heat transfer from an isothermal sphere to water”, *Journal of Heat Transfer*, Vol. 83, pp. 163-170, 1961.

[63] H. Kramers, “Heat transfer from spheres to flowing media”, *Physica*, Vol. 12, pp. 61-80, 1946.

[64] S. Whitaker, “Forced convection heat transfer correlations for flow in pipes, past flat plates, single cylinders, single spheres, and for flow in packed beds and tube bundles”, *AIChE Journal*, Vol. 18, pp. 361-370, 1972.

[65] W. Ranz, W. Marshall, “Evaporation from drops”, *Chemical Engineering Progress*, Vol. 48, pp. 141-146, 1952.

[66] S. C. Yao, V. E. Schrock, “Heat and mass transfer from freely falling drops”, *Journal of Heat Transfer*, Vol. 98, pp. 120-126, 1976.

[67] B. Melissari, S. A. Argyropoulos, “Development of a heat transfer dimensionless correlation for spheres immersed in a wide range of Prandtl number fluids”, *International Journal of Heat and Mass Transfer*, Vol. 48, pp. 4333-4341, 2005.

[68] E. Brunier, C. Jolivet, P. Guigon, D. Clausse, “Solidification of supercooled spherical droplets”, in: Numerical Methods in Thermal Problems, Proceedings of the 7th International Conference, Stanford, USA, Pineridge Press, Swansea, UK, pp. 291-301, 1991.

[69] E. J. Windhab, “New developments in crystallization processing”, *Thermal Analysis and Calorimitry*, Vol. 57, pp. 171-180, 1999.

[70] J. P. Hindmarsh, A. B. Russel, X. D. Chen, “Experimental and numerical analysis of the temperature transition of a freezing food solution droplet”, *Chemical Engineering Science*, Vol. 59, pp. 2503-2515, 2004.

[71] M. Flemings, “Solidification processing”, McGraw Hill, New York, 1974.

[72] H. Leuenberger, Business briefing: Pharmatech 2001, “New technologies for the manufacture of nanostructured drug carriers”, Report, World Markets Research Centre (WMRC), 2001.

[73] J. Liao, K. Ng, “Effect of ice nucleators on snow making and spray freezing”, *Industrial and Engineering Chemistry Research*, Vol. 29, pp. 361–366, 1990.

[74] J. Berriman, N. Unwin, “Analysis of transient structures by cryo-microscopy combined with rapid mixing of spray droplets”, *Ultramicroscopy*, Vol. 56, pp. 241-252, 1994.

[75] N. El-Kaddah, J. Szekely, “The electromagnetic force field, fluid flow field, and temperature profiles in levitated metal droplets”, *Metallurgical and Materials Transactions B*, Vol. 14, pp. 401-410, 1983.

[76] S. Song, B. Li, “Free surface profiles and thermal convection in electrostatically levitated droplets”, *International Journal of Heat and Mass Transfer*, Vol. 43, pp. 3589-3606, 2000.

[77] B. Adhikari, T. Howes, B. Bhandari, V. Truong, “Experimental studies and kinetics of single drop drying and their relevance in drying of sugar-rich foods: a review”, *International Journal of Food Properties*, Vol. 3, pp. 325-351, 2000.

[78] J. P. Hindmarsh, A. B. Russel, X. D. Chen, “Experimental and numerical analysis of the temperature transition of a suspended freezing water droplet”, *International Journal of Heat and Mass Transfer*, Vol. 46, pp. 1199-1213, 2003.

[79] A. Trommelen, E. Crosby, “Evaporation in drying of droplets and superheated vapours”, *AIChE Journal*, Vol. 16, pp. 857-866, 1970.

[80] L. Hallett, “Experimental studies of the crystallisation of supercooled water”, *Journal of the Atmospheric Sciences*, Vol. 21, pp. 671-682, 1964.

[81] S. Tabakova, F. Feuillebois, S. Radev, “Freezing of a supercooled spherical droplet with mixed boundary conditions”, *Proceedings of the Royal Society A*, Vol. 466, pp. 1117-1134, 2010.

[82] J. H. Hattel, N. H. Pryds, J. Thorborg, P. Ottosen, “A quasi-stationary numerical model of atomized metal droplets. I: Model formulation”, *Modelling and Simulation in Materials Science and Engineering*, Vol. 7, pp. 413-430, 1999.

[83] H. Liu, R. H. Rangel, and E. J. Lavernia, “Modeling of droplet-gas interactions in spray atomization of Ta-2.5W alloy”, *Materials Science and Engineering A*, Vol. 191, pp. 171–184, 1995.

[84] N. Zeoli, S. Gu, “Computational simulation of metal droplet break-up, cooling and solidification during gas atomization”, *Computational Materials Science*, Vol. 43, pp. 68–278, 2008.

[85] N. Zeoli, S. Gu, S. Kamnis, “Numerical modelling of metal droplet cooling and solidification”, *International Journal of Heat and Mass Transfer*, Vol. 51, pp. 4121-4131, 2008.

[86] S. Li, H. Fukuda, T. Ando, “Simulation of the solidification of gas-atomized Sn-5mass%Pb droplets.” *Materials Science and Engineering A*, Vol. 499, pp. 396–403, 2009.

[87] A. G. DiVenuti, “Modeling of the uniform droplet process.” MSc Thesis, Tufts University, Boston, MA, 1997.

[88] H. Inaba, K. Sato, “Latent cold heat energy storage characteristics by means of direct-contact-freezing between oil droplets and cold water solution”, *International Journal of Heat and Mass Transfer*, Vol. 40, No. 13, pp. 3189–3200, 1997.

[89] M. Song, A. Steiff, P. M. Weinspach, “The analytical solution for a model of direct contact evaporation in spray column”, *International Communications in Heat and Mass Transfer*, Vol. 23, No. 2, pp. 263–272, 1996.

[90] O. Jaber, G. F. Naterer, and I. Dincer, “Convective heat transfer from molten salt droplets in a direct contact heat exchanger”, *Heat and Mass Transfer*, Vol. 46, pp. 999-1012, 2010.

[91] B. Lally, L. Biegler, H. Henein, “Finite difference heat transfer modeling for continuous casting”, *Metallurgical Transactions B*, Vol. 21, pp. 761-770, 1990.

[92] A. K. Tieu, I. S. Kim, “Simulation of the continuous casting process by a mathematical model”, *International Journal of Mechanical Sciences*, Vol. 39, No. 2, pp. 185-192, 1997.

[93] S. K. Das, “Thermal modelling of DC continuous casting including sub mould boiling heat transfer”, *Applied Thermal Engineering*, Vol. 19, pp. 897–916, 1999.

[94] A. K. Tieu, I. S. Kim, “heat transfer analysis for the continuous casting process by the front tracking BEM”, *Engineering Analysis with Boundary Elements*, Vol. 24, pp. 215-223, 2000.

[95] J. Mahmoudi, “Mathematical modelling of fluid flow, heat transfer and Solidification in a strip continuous casting process”, *International Journal of Cast Metals Research*, Vol. 19, No. 4, pp. 223-236, 2006.

[96] S. S. Wei, S. I. Guceri, “solidification in developing pipe flows”, *International Journal of Heat and Fluid Flow*, Vol. 9, No. 2, pp. 225-232, 1987.

[97] G. J. Hwang, C. W. Tsai, “Effect of natural convection on laminar pipe flow solidification”, *International Journal of Heat and Mass Transfer*, Vol. 38, No. 15, pp. 2733–2742, 1995.

[98] J. Gammon and J. A. Howarth, “The inward solidification of cylinders with a slightly perturbed temperature distribution at the boundary”, *International Communications in Heat and Mass Transfer*, Vol. 23, No. 3, pp. 387–396, 1996.

[99] P. Sampson, R. D. Gibson, “Solidification of a liquid metal following through a circular pipe: A prediction of a nozzle blockage”, *Advances in Engineering Software*, Vol. 3, pp. 17–25, 1981.

[100] R. Conde, M. T. Parra, F. Castro, J. M. Villafruela, M. A. Rodriguez, C. Mendez, “Numerical model for two-phase solidification problem in a pipe”, *Applied Thermal Engineering*, Vol. 24, pp. 2501–2509, 2004.

[101] F. B. Cheung, L. Baker, “Transient freezing of liquids in tube flow”, *Nuclear Science and Engineering*, Vol. 60, pp. 1–9, 1976.

[102] R. V. Seeniraj and G. S. Hari, “Transient freezing of liquids in forced flow inside convectively cooled tubes”, *International Communications in Heat and Mass Transfer*, Vol. 35, pp. 786-792, 2008.

[103] M. Peters, K. Timmerhaus, R. West, Plant design and economics for chemical engineers, Fifth Edition, McGraw-Hill, 2002.

[104] I. C. Kemp, Pinch analysis and process integration: A user guide on process integration for the efficient use of energy, Elsevier, 2007.

[105] B. Linhoff, C. G. Akinradewo, "Linking process simulation and process integration", *Computers and Chemical Engineering*, Vol. 23, pp. S945-S953, 1999.

[106] A. I. A. Salama, "Determination of the optimal heat energy targets in heat pinch analysis using a geometry based approach", *Computers and Chemical Engineering*, Vol. 30, pp. 758-764, 2006.

[107] B. Linhoff, E. Hindmarsh, "The pinch design method for heat exchanger networks", *Chemical Engineering Science*, Vol. 38, pp. 745-763, 1983.

[108] F. Friedler, "Process integration, modelling and optimisation for energy saving and pollution reduction", *Applied Thermal Engineering*, Vol. 30, pp. 2270-2280, 2010.

[109] A. K. Kralj, "Estimating the maximum possible internal heat integrations of individual processes", *Energy*, Vol. 34, pp. 1372-1377, 2009.

[110] L. Matijaseviae, H. Otmaiae, "Energy recovery by pinch technology", *Applied Thermal Engineering*, Vol. 22, pp. 477-484, 2002.

[111] M. Morar, P. S. Agachi, "Review: Important contributions in development and improvement of the heat integration techniques", *Computers and Chemical Engineering*, Vol. 34, pp. 1171-1179, 2010.

[112] H. Axelsson, S. Harvey, A. Asblad, T. Berntsson, "Potential for green house gas reduction in industry through increased heat recovery and/or integration of combined heat and power", *Applied Thermal Engineering*, V. 23, pp. 65-87, 2003.

[113] B. Linnhoff, A. R. Eastwood, "Overall site optimisation by pinch technology", *Chemical Engineering Research and Design*, Vol. 75, pp. S138-S144, 1997.

[114] S. G. Yoon, J. Lee, S. Park, “Heat integration analysis for an industrial ethylbenzene plant using pinch analysis”, *Applied Thermal Engineering*, Vol. 27, pp. 886-893, 2007.

[115] S. Ghandehariun, G. F. Naterer, M. A. Rosen, Z. Wang, “Pinch analysis for recycling thermal energy in the Cu-Cl cycle”, Accepted, *International Journal of Hydrogen Energy*, 2012.

[116] http://webbook.nist.gov/chemistry/form-ser.html. Accessed on March 10th, 2011.

[117] G. D. Marin, Z. Wang, G. F. Naterer, K. Gabriel, “X-ray diffraction study of multiphase reverse reaction with molten CuCl and oxugen”, Thermochimica Acta, Vol. 524, pp. 109-116, 2011.

[118] C. Chow, H. F. Khartabil, “Conceptual fuel channel designs for CANDU-SCWR”, *Nuclear Engineering and Technology*, Vol. 40, pp. 139-143, 2008.

[119] S. Baindur, “Materials challenges for the supercritical water-cooled reactor (SCWR)”, *Bulletin of the Canadian Nuclear Society*, Vol. 29, pp. 32-38, 2008.

[120] S. Ghandehariun, G. F. Naterer, M. A. Rosen, Z. Wang, “Options for heat recovery from molten salt in thermochemical hydrogen production”, CSME Forum 2010, Victoria, BC, June 7 – 9, 2010.

[121] S. Ghandehariun, M. A. Rosen, G. F. Naterer, Z. Wang, “Comparison of molten salt heat recovery options in the Cu-Cl cycle of hydrogen production”, *International Journal of Hydrogen Energy*, Vol. 36, pp. 11328-11337, 2011.

[122] Personal communication with Dr. Zhaolin Wang, November 2009 to November 2010.

[123] J. Namiech, G. Berthoud, N. Coutris, “Fragmentation of a molten corium jet falling into water”, *Nuclear Engineering and Design*, Vol. 229, pp. 265-287, 2004.

[124] C. M. Van’t Land, Industrial crystallization of melts, Mill Valley, CRC Press, 2004.

[125] F. P. Incropera, D. P. DeWitt, Fundamentals of heat and mass Transfer, Fifth Edition, John Wiley & Sons, 2001.

[126] W. Rohsenow, J. Hartnett, Y. Cho, Handbook of heat transfer, Third Edition. McGraw-Hill Professional, NY, 1998.

[127] R. Clift, M. E. Weber, J. R. Grace, Bubbles, drops, and particles, Academic Press, N.Y., 1978.

[128] Y. A. Cengel, Heat transfer: A practical approach, Second Edition, McGraw-Hill, New York, 2003.

[129] E. N. Fuller, P. D. Schettler, J. C. Giddings, "A new method for prediction of binary gas-phase diffusion coefficients", *Industrial and Engineering Chemistry*, Vol. 58, pp. 19-27, 1966.

[130] The ultimate infrared handbook for R&D professionals: A resource guide for using infrared in the research and development industry, FLIR.

[131] B. D. Cullity, Elements of x-ray diffraction, Addison-wesley Publishing Company, Massachusetts, 1956.

[132] S. J. Kline, F. A. McClintock, "Describing uncertainties in single-sample experiments", *Mechanical Engineering*, Vol. 75, pp. 3-8, 1953.

[133] R. J. Moffat, "Contributions to the theory of single-sample uncertainty analysis", *Journal of Fluids Engineering*, Vol. 104, pp. 250-258, 1982.

[134] R. J. Moffat, "Describing the uncertainties in experimental results", *Experimental Thermal and Fluid Science*, Vol. 1, pp. 3-17, 1988.

[135] M. Strub, O. Jabbour, F. Strub, J. P. Bedecarrats, "Experimental study and modelling of the crystallization of a water droplet", *International Journal of Refrigeration*, Vol. 26, pp. 59-68, 2003.

[136] Workers health and safety centre, Molten materials and furnace hazards, Participant's Manual, Toronto, Canada, 1997.

[137] S. Ghandehariun, S., M. A. Rosen, G. F. Naterer, Z. Wang, “Reduction of hazards from copper(I) chloride in a Cu-Cl thermochemical hydrogen production plant” (in press), *Journal of Hazardous Materials*, 2012.

[138] L. Brewer, N. L. Lofgren, “The thermodynamics of gaseous cuprous chloride, monomer and trimer”, *Journal of the American Chemical Society*, Vol. 72, pp. 3038-3042, 1950.

[139] M. Guido, G. Gigli, M. Spoliti, “Mass spectrometric study of the vaporization of cuprous chloride and the dissociation energy of Cu_3Cl_3, Cu_4Cl_4, and Cu_5Cl_5”, *Journal of Chemical Physics*, Vol. 55, pp. 4566-4574, 1971.

Appendix

First Six Roots of the Transcendental Equation for Transient Conduction in a Sphere

Bi	ζ_1	ζ_2	ζ_3	ζ_4	ζ_5	ζ_6
0.001	0.0547	4.4936	7.7254	10.904	14.066	17.221
0.002	0.0774	4.4938	7.7255	10.904	14.066	17.221
0.004	0.1095	4.4943	7.7258	10.904	14.066	17.221
0.006	0.1341	4.4947	7.7260	10.905	14.067	17.221
0.008	0.1548	4.4952	7.7263	10.905	14.067	17.221
0.01	0.1730	4.4956	7.7265	10.905	14.067	17.221
0.02	0.2444	4.4979	7.7278	10.906	14.068	17.222
0.04	0.3450	4.5023	7.7304	10.908	14.069	17.223
0.06	0.4217	4.5068	7.7330	10.910	14.070	17.224
0.08	0.4860	4.5112	7.7356	10.911	14.072	17.225
0.1	0.5423	4.5157	7.7382	10.913	14.073	17.226
0.2	0.7593	4.5379	7.7511	10.922	14.080	17.232
0.4	1.0528	4.5822	7.7770	10.941	14.095	17.244
0.6	1.2644	4.6261	7.8028	10.959	14.109	17.255
0.8	1.4320	4.6696	7.8284	10.977	14.123	17.267
1	1.5708	4.7124	7.8540	10.996	14.137	17.279
2	2.0287	4.9132	7.9787	11.085	14.207	17.336
3	2.2889	5.0870	8.0962	11.173	14.276	17.393
4	2.4556	5.2329	8.2045	11.256	14.343	17.449
5	2.5704	5.3540	8.3029	11.335	14.408	17.503
6	2.6537	5.4543	8.3913	11.409	14.470	17.556
7	2.7164	5.5378	8.4703	11.477	14.529	17.607
8	2.7653	5.6078	8.5406	11.541	14.585	17.656
9	2.8044	5.6669	8.6031	11.599	14.637	17.703
10	2.8363	5.7172	8.6587	11.653	14.687	17.748